MODELING OF GAS RELEASE FROM AN UNDERGROUND PIPELINE

A Thesis

by

IBRAHIM LOKMANE DAOUDI

Submitted to the Office of Graduate and Professional Studies of
Texas A&M University
in partial fulfillment of the requirements for the degree of

MASTER OF SCIENCE

Chair of Committee,	Luc Véchot
Committee Members,	Marcelo Castier
	Konstantinos Kakosimos
	Mahmood Amani
Head of Department,	M. Nazmul Karim

December 2018

Major Subject: Chemical Engineering

ABSTRACT

Buried pipelines are one of the major transportation methods for natural gas and other light hydrocarbons around the world. With that comes the risk of pipeline failure and the release of the flammable materials, which have caused many incidents in the past including significant human and economic losses. Thus, understanding the behavior of underground gas flow and the way it escapes to the atmosphere is necessary for consequence modeling, in order to have the best possible prevention and mitigation barriers.

Depending on the conditions, the gas flow regime can be divided into three categories: diffusion, fluidization, and crater formation. The main objective of this project is to develop a CFD model that is able to simulate all underground gas flow regimes. The model was developed using the ANSYS Workbench Software. The dimensions of the simulated systems were based on the information given by industries in Qatar. The adopted approach included the Eulerian-Eulerian multicomponent model, the standard k-ε turbulence model, and the Gidaspow drag model. The model was configured and refined by testing the effect of various parameters such as the type of boundary conditions used, and the effect observed by changing some of the input data.

The configured model was validated against experimental data, with emphasis on testing its ability to predict the underground gas flow regime, and local methane concentrations. The model was then used to simulate various scenarios with differing the gas inlet velocity and soil density values. The results for each simulation were recorded with the gas underground gas flow regime identified, and then plotted using dimensionless numbers such as the Reynolds' and Archimedes' numbers. The obtained graph helps identifying the boundaries between each flow regime. The results of one of the simulations were used as an input for a consequence modeling software, and the threat zone based on the inputted data was reported.

ACKNOWLEDGEMENTS

I would like to show my appreciation and gratitude to my committee chair Dr. Luc Véchot, and my committee members Dr. Marcelo Castier, Dr. Konstantinos Kakosimos, and Dr. Mahmood Amani. I would like to thank Dr. Luc for his support from throughout the life time of the project, for his patience with the hurdles faced, and for his overall guidance and advice. I would like to thank Dr. Marcelo for his support throughout the life time of the project, and especially for his enthusiasm and positive energy when I was having a blue day, along with his suggestions and advices. I would like to thank Dr. Kakosimos for his massive help with the development of the CFD model with his great experience with the software, along with the guidance and help to finalize this project. I would like to thank Dr. Mahmood as well for his support for this project, and for his words of encouragement. The outcome would not have been possible to me without their support.

I would like to thank the Mary Kay O'Conner Process Safety Center at Qatar (MKOPSC-Q) and all its members for their continuous technical and mental support, and for the center for funding this project and making it possible.

Finally, I would like to thank my parents for their encouragement and support since I opened my eyes to this world.

CONTRIBUTORS AND FUNDING SOURCES

This work was supervised by a thesis committee consisting of Dr. Luc Véchot as the Committee chair and Professors Dr. Marcelo Castier and Dr. Konstantinos Kakosimos of the Department of Chemical Engineering and Dr. Mahmood Amani of the Department of Petroleum Engineering. All work for the thesis was completed independently by the student.

The project was funded by the Mary Kay O'Connor Process Safety Center at Qatar.

TABLE OF CONTENTS

Page

LIST OF FIGURES

Page

LIST OF TABLES

Page

1 INTRODUCTION

Natural gas is one of the most used energy sources in the world, contributing with 21.6% of the world's energy supply in 2015. Natural gas is especially important in Qatar, with the country being the world's second natural gas exporter in 2016 with 117 bcm.[1] One of the most common methods of transporting fuel or chemical gases, including natural gas, is using buried pipelines. While this method has many advantages, it remains important to control the risks associated to the underground releases of hydrocarbons.

Underground releases may be long duration low flow leaks (e.g. flange leaks or corrosion) which are harder to detect and may affect the soil and environment. Other types of releases may lead to high flow discharges (e.g. pipeline rupture due to excessive corrosion or due to mechanical impact with digging equipment) be more severe. Not only can they affect the soil and environment, they can form craters around the release point, and the released gas can pose toxic, fire and explosion hazards to the nearby workers or even public surrounding the pipeline.

The following historical examples illustrate the potential consequences of pipeline rupture.

- *Andhra Pradesh, India (Figure 1)*

On June 27th 2014, at around 5:30 am, a blast occurred in an underground natural gas pipeline in east Godavari district in the state of Andhra Pradesh in India. The pipeline was owned by a government company called GAIL (Gas Authority of India Limited). The cause of the incident was an over pressurized gas supply, which was, according to some sources, at twice the design pressure. The locals reported that a minor leak had already been present for days before the incident, and nothing was done to stop it. The state of the pipeline after the incident also showed that the pipeline was rusty. The explosion resulted in a crater with a radius of around 7 m. The explosion resulted in a full bore rupture of the pipeline and a massive spill of gas spread over around 500 m. The cloud ignited and caused another explosion in the form of unconfined vapor cloud explosion (UVCE), followed by

a pool fire that kept burning for hours until the supply ended. The incident led to the death of 22 people and the injury of 38 others and resulted in significant environmental and economic losses.[2][3]

Figure 1 Resulting crater, pipeline full-bore rupture and fire, Andhra Pradesh, India Reprinted from [2]

- *New Mexico, USA (Figure 2)*

On August 19th 2000, at around 5:26 am, a rupture occurred in a 30-inch natural gas transmission pipeline next to the Pecos River near Carlsbad, New Mexico. The pipeline was operated by El Paso Natural Gas Company (EPNG). The released gas ignited resulting in a fireball and the fire kept burning for 55 minutes. The explosion resulted in a crater that was about 15.54 m wide and with a length of 34.44 m along the pipeline. A piece of the pipeline that was 7.9 m long was found at around 87.5 m away from the crater. The incident led to the death of 12 people who were camping nearby and to property damage including two nearby suspension bridges for gas pipelines. The total economic loss estimated by EPNG was $998,296. An investigation into the incident was conducted by The National Transportation Safety Board in order to identify the cause. According to the

report, the cause of the rupture of the pipeline was due to significant reduction in pipe wall thickness due to severe internal corrosion. In addition, the corrosion occurred because the EPNG's corrosion control program failed to prevent, detect, or control the corrosion. Furthermore, the ineffective federal inspection on EPNG contributed to the incident.[4]

Figure 2 Crater formation and fire after pipeline rupture, New Mexico, USA Reprinted from [4]

Pipeline release incidents can cause a wide range of consequences. In order to control the risk associated to pipeline rupture (and effectively design for prevention, mitigation and emergency response measures), it is of upmost importance to predict the consequences associated to these events. This requires the understanding of the flow mechanism of the gas leaking through the ground for given pipeline conditions.

This thesis is contributes to improving the existing methods to predict the consequences of underground gas releases.

2 LITERATURE REVIEW

Determining how to model a natural gas leak through the ground depends heavily on the flow mechanism of the gas. A simple evaluation of the issue allows us to expect that the gas leak out of the underground pipeline can be released in three different regimes depending on the flowrate of the release, orientation of the release and the soil properties (Figure 3):

- First, a flow rate of gas can be so small that the gas will only diffuse, migrate through soil pores and will not displace or move soil.
- The second regime may be expected at larger flow rates, for which the gas can start displacing the soil, lift it and generate mixing. This is known as a fluidization.
- The third regime may be expected at much larger flow rates for which the gas jet will violently eject the soil up, creating a crater and resulting in an unobstructed jet flow.

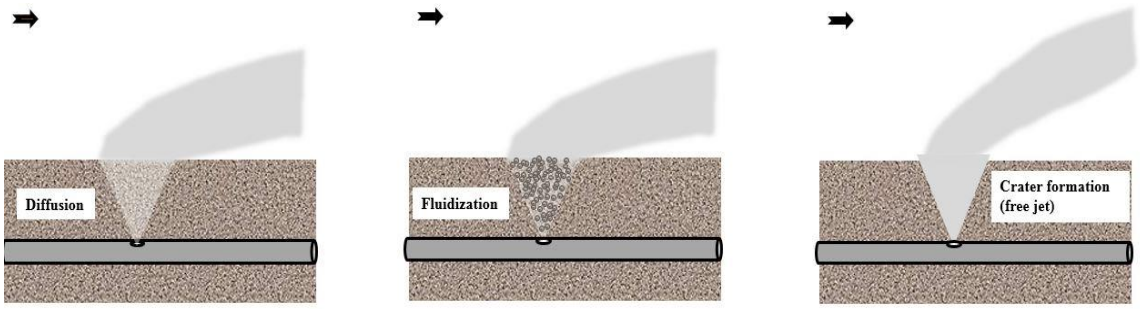

Figure 3 Different underground release behaviors for upward release

The following section summarizes the literature review of the currently available models (and validation when available) for the prediction of underground gas releases as well as the published experimental data on underground gas releases from buried pipelines.

2.1 Diffusion of Gas through Soil

2.1.1 Existing Models Describing Underground Gas Diffusion

To date, very few researches have been done on modelling of the underground releases of gases from buried pipelines. Most of developed models and research have focused on atmospheric gas dispersion, which is a far-field model, and not giving sufficient attention to near-field and the behavior of the gas flowing through the ground, although the result of the near-field model is input to the far-field one and thus greatly affects its quality. If the near-field model is not correct, neither will be the far-field model.[5]

2.1.1.1 Wakoh and Hirano 1991

According to Wakoh and Hirano [6], understanding the diffusion phenomena of underground gas is pretty complex, and requires considering the following:

- the diffusion process of leaked gas in soil;
- the outflow volume of gas;
- the gas concentration profile;
- the actual position of the break in the pipeline;
- the time that the leak started.

The author mentions that there are only few studies that considered underground gas diffusion prior to his paper, including Ohtsuga [7] who made a diffusion model using a binary gaseous mixture in a cylinder, and Palcoz et al. [8] who used equations representing mass conversation, Darcy's law, and Knudson diffusion. However, the authors claimed that these models were not applicable to dilute concentrations and at points that are at a long distance from the leak source.

The author derived an equation starting from the convection-diffusion equation, then performed an experiment to validate the model.

2.1.1.1.1 Assumptions

The assumptions used to develop the model were:

- the flow rate of the leaking gas (in this case, propane) remains constant;
- the leak pressure is near atmospheric;
- the gas leaks in a spherical pattern;
- the porosity of the soil and the diffusion coefficient of the gas are constant;
- the soil is homogenous;
- the gravity and the density variations of the gas in the soil are negligible;
- no gas present in the soil before the leak.

2.1.1.1.2 Equations

For a gas diffusing in a spherical matter, its concentration can be written as:[9], [10]

$$\rho = \frac{r}{x} erfc \frac{x - r}{2\sqrt{Dt}} \qquad (1)$$

$$r = \left(\frac{3Qt}{4\pi\varepsilon}\right)^{1/3} \qquad (2)$$

where:

- ρ is the gas concentration;
- r is the radius of convection face;
- x is the distance from the leak site;
- D is the gas diffusion coefficient;
- t is the lapse of time;
- Q is the leaked gas flow rate;
- ε is the soil porosity.

Combining Equations (1) and (2), one obtains:

$$\rho = \frac{\left(\frac{3Qt}{4\pi\varepsilon}\right)^{1/3}}{x} erfc \frac{x - \left(\frac{3Qt}{4\pi\varepsilon}\right)^{1/3}}{2\sqrt{Dt}} \quad (3)$$

By differentiating Equation (3) with respect to time, one obtains:

$$\left(\frac{\left(\frac{3Qt}{4\pi\varepsilon}\right)^{2/3} \tau^{7/6}}{L\rho_0}\right)\left(\frac{D}{\pi}\right)^{1/2} = exp\left(\frac{L - \left(\frac{3Qt}{4\pi\varepsilon}\right)^{1/3}}{2(D\tau)^{1/2}}\right)^2 \quad (4)$$

where*:*

- τ is the time required for the gas concentration to increase to a specific value ρ_0;
- ρ_0 is a specific value of gas concentration that is of interest;
- L is the distance from the leak site.

2.1.1.1.3 Verification

An experiment was performed in order to validate the developed model. The experiment was performed in a ground with a depth of 1.3 m of sandy soil and a thinner upper layer of 0.2 m consisting of conglomerate clay. Three pipelines were buried at a depth of 0.61 m underground with a distance of 1 m between them. Each pipe had a leak hole with a diameter of 6 mm. The leak gas used was liquefied petroleum gas (LPG) consisting of 95% propane and their pressure was kept at around 2.7 kPa. The gas flowrates out of the pipes were 100 ml/s, 200 ml/s, and 300 ml/s and the concentrations were observed 1 m, 2 m, and 3 m away from the leak point using He-Ne sensors. Figures 4-6 show the results of the experiment compared to calculated values.

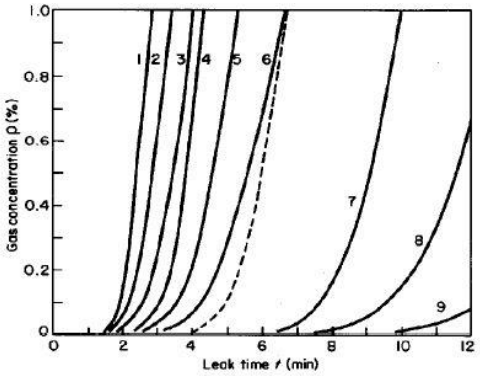

Figure 2 Variations of gas concentration at 1 m from the leak site: —, calculated values from Equation (3); - - -, continuous observed values. Values of D ($cm^2 s^{-1}$) and Q ($ml s^{-1}$):

	Curve number								
	1	2	3	4	5	6	7	8	9
D	1	1	1	0.5	0.5	0.5	0.1	0.1	0.1
Q	300	200	100	300	200	100	300	200	100

Figure 4 Gas concentration data at 1 m from the leak point Reprinted from [6]

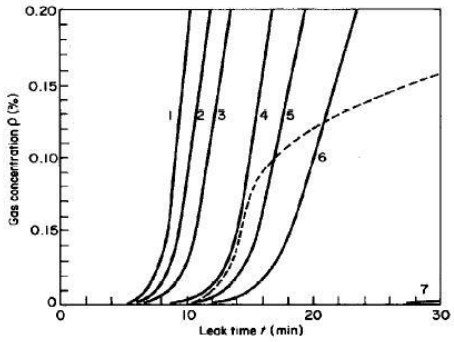

Figure 3 Variations of gas concentration at 2 m from the leak site: —, calculated values from Equation (3); - - -, continuous observed values. Values of D ($cm^2 s^{-1}$) and Q ($ml s^{-1}$):

	Curve number						
	1	2	3	4	5	6	7
D	1	1	1	0.5	0.5	0.5	0.1
Q	300	200	100	300	200	100	300

Figure 5 Gas concentration data at 2 m from the leak point Reprinted from [6]

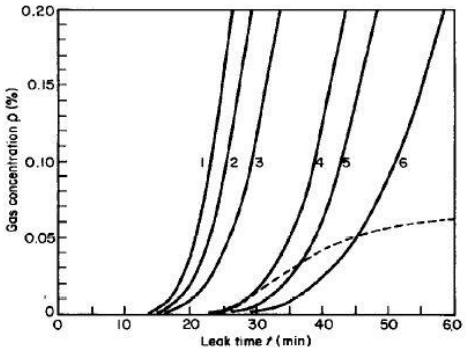

Figure 4 Variations of gas concentration at 3 m from the leak site: —, calculated values from Equation (3); - - -, continuous observed values. Values of D ($cm^2 s^{-1}$) and Q ($ml s^{-1}$):

	Curve number					
	1	2	3	4	5	6
D	1	1	1	0.5	0.5	0.5
Q	300	200	100	300	200	100

Figure 6 Gas concentration data at 3 m from the leak point Reprinted from [6]

2.1.1.1.4 Findings

A set of experimental data was obtained and it was observed that the value of the diffusion coefficient obtained experimentally was much greater than the one commonly used from molecular diffusion results.

2.1.1.2 Hibi et al. 2009

According to the authors [11], the mechanism of material transport in the gas zone in soil is more complicated than in the water zone. This is due to the fact that, unlike the water zone, in which diffusion, advection, and dispersion are considered, it also includes the Knudsen diffusion, the difference in molecular weight between components, and the multi-component gas system, in addition to the previously mentioned parameters, as stated by Mason et al. [12]. Diffusion has been modeled using different diffusion laws. Various authors modeled diffusion using Fick's Law, such as Sleep and Sykes [13]. The law was used to model binary gas systems in the gas zone of the soil. Fick's law, however, is not

applicable to a multi-component gas system. Another law that was used to model diffusion is Blanc's law [14], which was derived from the Stefan-Maxwell model [15]. Hoeg et al. [16] used a model based on Blanc's law to simulate the transport of low concentration substances in a multi-component gas system. However, Blanc's law is only applicable if the gases other than the moving gas are stagnant, and that the moving gas is at a low concentration. The Stefan-Maxwell equations and the dusty gas model can be used to model multi-component gas system in every concentration range including high concentration. The Stefan-Maxwell equation was compared with Fick's law in a one dimensional binary gas system with low concentration by Baehr and Bruell [17]. It was found out that both models gave similar results. One of the authors of this paper (Hibi [18]) compared the dusty gas model to Blanc's law, and found out that the concentrations differ, in which the results using Blanc's law show a higher concentration of the moving chemical substance. The effect of the Knudson diffusion was also studied by Thorstenson and Pollock [19], and Massmann and Farrier [20], and they found out that the Knudson diffusion has a significant influence in the case with a soil permeability lower than 10^{-14} m^2.

The authors of this paper derived the compound diffusion, which includes the molecular diffusion, and the Knudson diffusion, and the compound velocity, which includes the two previous parameters along with the gas pressure gradient and velocity, from the dusty gas model equations. The authors then verified the model using experimental data obtained using columns filled with dry sand.

2.1.1.2.1 Assumptions

The assumptions used to develop the model were:

- gas slippage does not occur;
- the gas is slowly moving through the soil;
- the porous media is incompressible;
- the gas behaves as an ideal gas;
- dispersion is not considered.

2.1.1.2.2 Equations

The gas velocity as described by Darcy's law is:

$$V_g = -\frac{K_{rg} k_s}{\mu_g} (\nabla P_g + \rho_g g \nabla z) \quad (5)$$

Where:

- V_g is the gas velocity in soil [L/T];
- k_s is the intrinsic permeability [L^2];
- K_{rg} is the permeability relative to intrinsic permeability;
- μ_g is the viscosity of the mixed gas [M/LT];
- P_g is the gas total pressure [M/LT^2];
- ρ_g is the gas density [M/L^3];
- g is the gravitational constant [L/T^2];
- z is the vertical coordinate positive in the upward direction.

By using Darcy's law and the continuity equation, the gas flow can be expressed as:

$$\frac{\partial \theta_g}{\partial t} = \nabla . \left[\frac{K_{rg} k_s}{\mu_g} \nabla (P_g + \rho_g g z) \right] \quad (6)$$

Where:

- θ_g is the gas filled porosity;
- t is time [T].

The density of the mixed gas can be calculated using:

$$\rho_g = \sum_i^v C_i M_i \quad (7)$$

Where:

- C_i is the molar concentration of gas i [mol/L^3];
- M_i is molecular mass of gas i [T].

The viscosity of the mixed gas is obtained using Equation (8) which was proposed by Reid et al. [21]

$$\mu_g = \sum_{i=1}^{v} \frac{X_i^g \mu_i^g}{\sum_{j=1}^{v} X_j^g \vartheta_{ji}} \qquad (8)$$

Where:

- X is the molar fraction;
- μ is the viscosity [M/LT].

And,

$$\vartheta_{ji} = \left(\frac{M_i}{M_j}\right)^{0.5} = \frac{1}{\vartheta_{ij}} \qquad (9)$$

The molecular diffusion in a multi-gas system given by the dusty gas law is:

$$\sum_{\substack{j=1 \\ j \neq i}}^{v} \frac{X_i N_j^D - X_j N_i^D}{\tau \theta_g D_{ij}} - \frac{N_i^D}{\tau \theta_g D_i} = \frac{1}{RT} \nabla (P_i + \rho_i g z) \qquad (10)$$

Where:

- N_j^D, N_i^D are the molar fluxes of components j and i respectively [mol/L^{2}T];
- τ is the tortuosity;
- D_{ij} is the Knudsen diffusion coefficient [L^2/T];
- R is the gas constant [M L^2/molKT^2];
- T is the temperature [K];
- P_i is the partial pressure of component i [M/LT^2];
- ρ_i is the gas density of component i [M/L^3].

The advection-dispersion equation can be written as:

$$\frac{\partial \theta_g C_i}{\partial t} + \nabla . V_g C_i + \nabla . (\boldsymbol{J}_i^{mech} + N_i^D) = 0 \qquad (11)$$

where:

- $V_g C_i$ is the advection flux;
- $\boldsymbol{J}_i^{mech}$ is the dispersion flux.

By substituting $C_i = \frac{P_i}{RT}$ and $\rho_i = M_i C_i$ into Equation (10) and rearranging, we obtain:

$$\sum_{\substack{j=1 \\ j \neq i}}^{v} \frac{X_i N_j^D - X_j N_i^D}{D_{ij}} - \frac{N_i^D}{D_i} = \tau \theta_g \left(\nabla C_i + \frac{M_i \boldsymbol{g}}{RT} C_i \right) \qquad (12)$$

where $\boldsymbol{g}$ is the gravity vector with L/T^2 dimensions.

By summing both sides of Equation (12) and rearranging we obtain:

$$-\sum_{i=1}^{v} \frac{N_i^D}{D_i} = \frac{\tau \theta_g}{RT} \nabla (P_g + \rho_g g z) \qquad (13)$$

The diffusion flux can be obtained by substituting Equation (13) into Equation (12):

$$\begin{aligned} N_i^D = & -\tau \theta_g D_{cij} \nabla C_i - \frac{\tau \theta_g M_i \boldsymbol{g} D_{cij}}{RT} C_i \\ & - D_{cij} \sum_{\substack{j=1 \\ j \neq i}}^{v} \frac{X_i}{D_{ij}} \left(\sum_{\substack{k=1 \\ k \neq i \\ k \neq j}}^{v} \frac{D_j}{D_k} N_k^D \right) \\ & - \frac{\tau \theta_g D_{cij}}{RT} \sum_{\substack{j=1 \\ j \neq i}}^{v} D_j \frac{X_i}{D_{ij}} \nabla (P_g + \rho_g g z) \end{aligned} \qquad (14)$$

where,

$$D_{cij} = \frac{1}{\left\{\sum_{\substack{j=1 \\ j\neq i}}^{v}\left[\left(\frac{D_j}{D_i}\right)\left(\frac{X_i}{D_{ij}}\right)+\left(\frac{X_j}{D_{ij}}\right)\right]+\frac{1}{D_i}\right\}}$$

The total molar flux N_i^T for a component i is the sum of the advective molar flux and the diffusive molar flux. The diffusive molar flux N_i^F can be obtained using Equation (5):

$$N_i^F = V_g C_i = -C_i \frac{K_r k_s}{\mu_g}(\nabla P_g + \rho_g g \nabla z) \qquad (15)$$

By using Equations (14) and (15), the total molar flux is obtained:

$$\begin{aligned} N_i^T = & -\tau\theta_g D_{cij}\nabla C_i \\ & -\left\{\frac{\tau\theta_g M_i \boldsymbol{g} D_{cij}}{RT}\right. \\ & +\frac{D_{cij}}{C}\sum_{\substack{j=1 \\ j\neq i}}^{v}\frac{1}{D_{ij}}\left(\sum_{\substack{k=1 \\ k\neq i \\ k\neq j}}^{v}\frac{D_j}{D_k}N_k^D\right) \\ & \left.+\left\{\frac{\tau\theta_g D_{cij}}{CRT}\sum_{\substack{j=1 \\ j\neq i}}^{v}\frac{D_j}{D_{ij}}+\frac{K_g k_s}{\mu_g}\right\}\nabla(P_g+\rho_g g z)\right\} \end{aligned} \qquad (16)$$

The first term on the right side of Equation (16) represents the compound diffusion coefficient D_i^*, which includes the molecular diffusion and Knudson diffusion, and the second term represents the compound velocity V_{gi}^* which is the advective term that influences the diffusion by gravity, gas pressure, molecule motion with Darcy's velocity, and diffusion fluxes of other components. Equation (16) can be rewritten as:

$$N_i^T = -D_i^* \nabla C_i + V_{gi}^* C_i \qquad (17)$$

By substituting Equation (17) into the continuity equation, the advection-diffusion equation is obtained:

$$\frac{\partial C_i}{\partial t} + V_g^* \nabla C_i = \nabla . (D_i^* \nabla C_i) \qquad (18)$$

By applying the finite element scheme on the left side, Equation (18) can be approximated to:

$$\frac{\partial C_i}{\partial t} + V_g^* \nabla C_i = \sum_{k=1}^{n} \Phi_k \{ C_{ik}(x_k, y_k, z_k, t + \Delta t) - C_{ik}(x_k - V_{gx}^* \Delta t, y_k - V_{gy}^* \Delta t, z_k - V_{gz}^* \Delta t, t) \} / \Delta t \qquad (19)$$

where:

- n is the number of nodal points;
- Φ_k is the Sharpe function for the finite element method;
- x_k, y_k, z_k is the coordinates of nodal point k;
- $V_{gx}^*, V_{gx}^*, V_{gx}^*$ are the velocities in the x, y, and z directions respectively;
- $C_{ik}(x_k, y_k, z_k, t + \Delta t)$ is the molar concentration of component i at node k and time = $t + \Delta t$ [mol/L^3];
- $C_{ik}(x_k - V_{gx}^* \Delta t, y_k - V_{gy}^* \Delta t, z_k - V_{gz}^* \Delta t, t)$ is the molar concentration of component i at node k, with $x = x_k - V_{gx}^* \Delta t$, $y = y_k - V_{gy}^* \Delta t$, $z = z_k - V_{gz}^* \Delta t$ and time = t [mol/L^3].

In order to solve the right hand side of Equation (18), finite elements are used to discretize it. The time is discretized using the Euler method, and the nonlinearities are solved using Picard iteration. With doing so, Equation (20) is obtained as:

$$\left(\frac{1}{\Delta t}\int_A \Phi_k dA + \sum_{k=1}^{n} \overline{D}_i^{*t+\Delta t,m} \int_A \nabla\Phi_k . \nabla\Phi_l dA\right) \times C_{ik}^{t+\Delta t,m+1}(x_k, y_k, z_k, t+\Delta t) = \frac{1}{\Delta t}\int_A \Phi_k dA\, C_{ik}\left(x_k - V_{gx}^{*}\Delta t, y_k - V_{gy}^{*}\Delta t, z_k - V_{gz}^{*}\Delta t, t\right) + \int_\Omega \Phi_k \bar{q}_{ci}^{t+\Delta t,m+1} . \boldsymbol{n} d\Omega \quad \begin{pmatrix} k = 1, n \\ i = 1, v-1 \end{pmatrix} \qquad (20)$$

where:

- A is the volume of the analytic domain [L^3];
- m is the iteration number for nonlinearity;
- Ω is the surface of the boundary [L^2];
- $\bar{q}_{ci}$ is the molar flux of component i at the boundary [mol/ L^2T];
- $\boldsymbol{n}$ is the normal vector of the boundary.

The molar concentration of component v at point k can be obtained using the molar concentration from equation (20) of components 1 to $v-1$ subtracted from the total concentration.

$$C_{vk}^{t+\Delta t,m+1} = \frac{P_{gk}^{t+\Delta t,m+1}}{RT} - \sum_{i=1}^{v-1} C_{ik}^{t+\Delta t,m+1} \qquad (21)$$

Obtaining the molar flux N_k^D is required in order to use Equation (20). The flux can be obtained by rearranging Equation (10).

$$\left(\sum_{\substack{j=1\\ j\neq i}}^{v}\frac{X_j}{\tau\theta_g D_{ij}}-\frac{1}{\tau\theta_g D_i}\right)N_i^D-\sum_{\substack{j=1\\ j\neq i}}^{v}\frac{X_i}{\tau\theta_g D_{ij}}N_j^D \qquad (22)$$

$$=-\nabla C_i-\frac{M_i\boldsymbol{g}}{RT}C_i.\ (i=1,v-1)$$

Equations (13) and (22) are discretized using the Galerkin finite element method.

$$\left(\sum_{\substack{j=1\\ j\neq i}}^{v}\frac{\bar{X}_j^{t+\Delta t,m}}{\tau\bar{\theta}_g D_{ij}}+\frac{1}{\tau\bar{\theta}_g D_i}\right)\int_A \Phi_k dA\, N_{ik}^{D^{t+\Delta t,m+1}}$$

$$-\sum_{\substack{j=1\\ j\neq i}}^{v}\frac{X_i^{t+\Delta t,m}}{\tau\bar{\theta}_g D_{ij}}\int_A \Phi_k dA\, N_{jk}^{D^{t+\Delta t,m+1}} \qquad (23)$$

$$=-\sum_{l=1}^{n}\Phi_k\nabla\Phi_l dA\nabla C_{il}^{t+\Delta t,m}$$

$$-\frac{M_i\boldsymbol{g}}{RT}\int_A \Phi_k dA\, C_{ik}^{t+\Delta t,m}.\ \begin{pmatrix}k=1,n\\ i=1,v-1\end{pmatrix}$$

$$-\sum_{i=1}^{v}\frac{1}{D_i}\int_A \Phi_k dA\, N_{ik}^{D^{t+\Delta t,m}}$$

$$=\frac{\tau\theta_g}{RT}\left(\sum_{l=1}^{n}\int_A \Phi_k\nabla\Phi_l dA P_{gl}^{t+\Delta t,m}\right. \qquad (24)$$

$$\left.+\bar{\rho}_g^{t+\Delta t,m}g\int_A \Phi_k dA\right)\ (k=1,n)$$

The molar flux of each component is obtained using equations (23) and (24). Then, the molar concentration is obtained using equation (6), (20), and (21).

2.1.1.2.3 Verification

In order to verify the model, a column experiment was designed. The column was 90 cm long and had a diameter of 50 cm. The column had 5 ports with syringes, in order to take out gas samples, and 5 pressure gauges, in order to measure the gas pressure. The column was filled with dry sand with particle size of 0.08-2 mm. Two different gases were injected into the column, which was already filled with air (containing nitrogen and nitrogen). The first gas was methane which is lighter than air in terms of molecular weight, and the second gas was carbon dioxide, which is heavier than air. The gas was inserted through the inlet with a pressure of around 97 kPa, and the gas flow rate was measured at the outlet using a flow meter. The pressure of the gas was recorded with the gas pressure gauges. Gas samples were taken from the port through syringes, and the gas samples were tested using gas chromatography. The experiment was stopped once the gas reached the last port (port number 5), and each experiment was repeated twice, using both either methane or carbon dioxide as the inlet gas. Figure 7 shows the experimental setup, and Figure 8 shows the structure of the column. An example of the experimental data compared with Blanc's law and the dusty gas model for a three component system is shown in Figure 9.

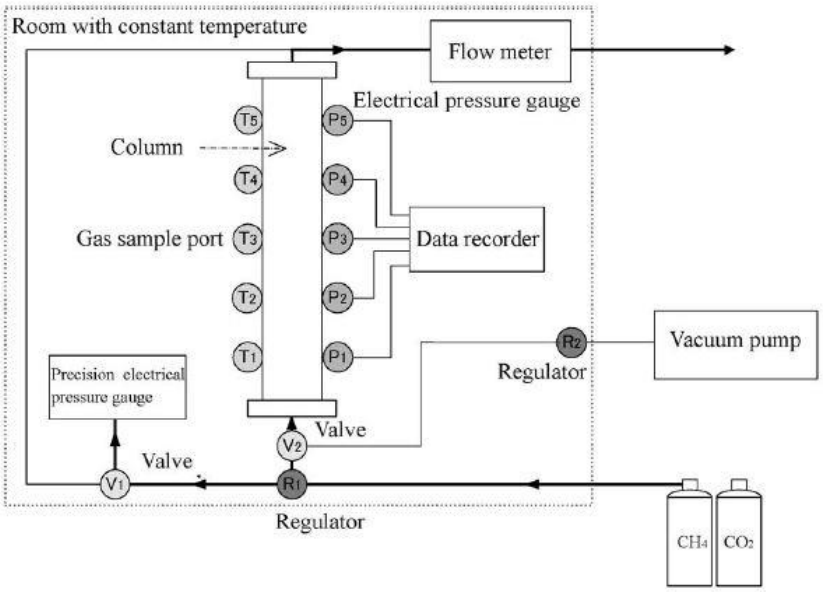

Figure 7 Hibi et al. experimental setup Reprinted from [11]

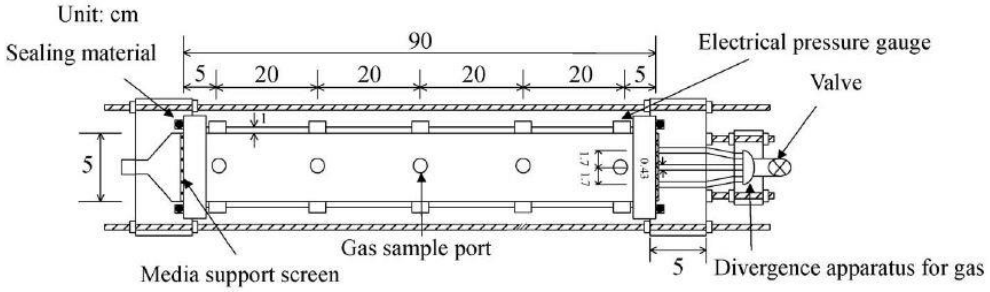

Figure 8 Detailed column illustration Reprinted from [11]

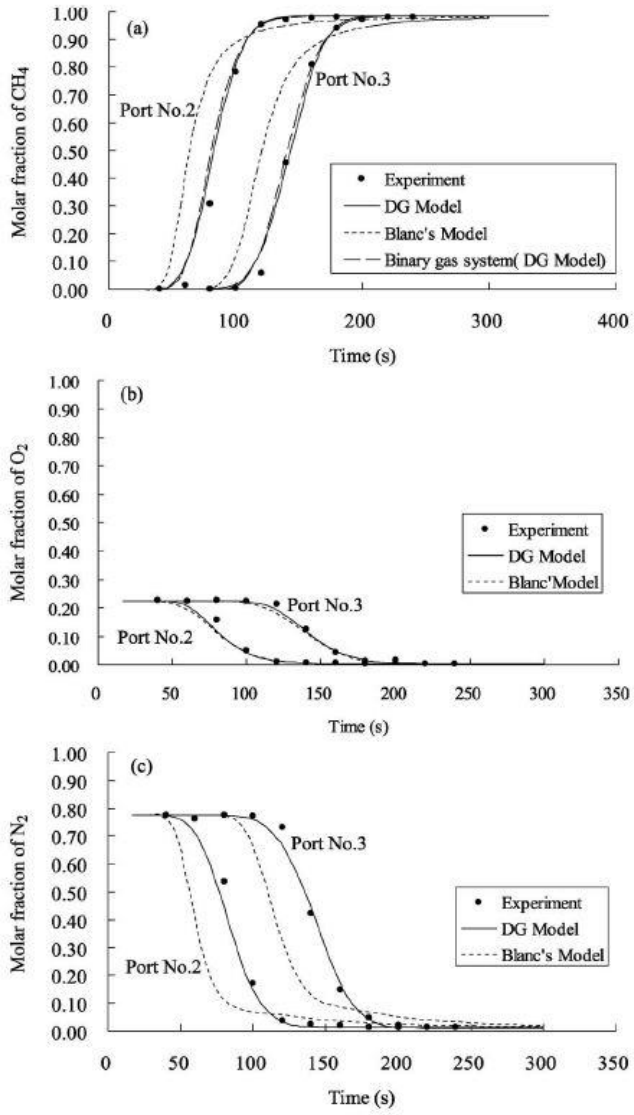

Figure 9 Hibi et al. experimental data compared to models Reprinted from [11]

2.1.1.2.4 Findings

The experimental results were compared with the dusty gas model, and the model was able to accurately simulate the multi-component and the binary gas systems. The model was also compared with Blanc's model, and Fick's model. The results show that Blanc's

model results did not match the experimental data except for oxygen, as shown in Figure 9. Thus, Blanc's model cannot be used to simulate a multi-component gas system with a wide range of molar concentrations. For a binary gas system, both Fick's model and the dusty gas model gave similar results.

2.1.1.3 Okamoto and Gomi 2011

Okamoto and Gomi [22] stated that in order to clarify the diffusion behavior, three things must be studied, which are as follows:

- the behavior caused by differences in pressure, specific gravity, and concentration.
- the gas and soil composition and the geometric boundary conditions of the ground
- the behavior in a wide area and the behavior in local zones like the zone around the leakage point.

They have also stated that many studies focused on the dispersion of gas through the atmosphere, and only a small number on underground gas diffusion. The authors performed a full-scale experiment, and then used the experimental data to verify the applicability of an analytical tool on a full-scale level. The analytical tool consisted of the equation of motion, equation of continuity, and an equation of state.

2.1.1.3.1 Assumptions

The assumptions used in the analytical tool were:

- a volume element is integrated and averaged over a volume larger than the pore size but smaller than the whole ground;
- low pressure (no soil movement);
- the soil volume is constant;
- the present gases are only air and the leaked gas;
- the gas flow is laminar;
- the process is at steady state;
- the gas behaves as an ideal gas.

2.1.1.3.2 Equations

In order to describe the gas motion through the soil, the equation of motion in Cartesian coordinates is used.

$$\rho \frac{\partial \vec{v}}{\partial t} + \rho(\vec{v}.\nabla)\vec{v} = -\nabla p - [\nabla.\vec{\tau}] + \rho\vec{g} + \vec{F} \qquad (25)$$

where*:*

- ρ is the density of the gas $[kg/m^3]$;
- $\vec{v}$ is the velocity of the gas $[m/s]$;
- p is the gas pressure $[Pa]$;
- $\vec{\tau}$ is the shear stress $[N/m^2]$;
- $\vec{g}$ is the gravitational acceleration $[m/s^2]$;
- $\vec{F}$ is the external force per unit volume on the gas.

By assuming that the pores in the soil are crooked tubes with a varying cross sections, and considering the gas flow to be laminar inside a tube, the average velocity at the direction of the flow can be expressed as

$$v = \frac{d^2/32}{\mu}\left(-\frac{dp}{dz} + \rho g\right) \qquad (26)$$

where μ is the coefficient of viscosity of the gas $[Pa.s]$.

When introducing an air permeability coefficient on an average cross section of the aforementioned crooked tubes, Equation (27) is obtained, which is equivalent to Darcy's Law.

$$\vec{v}_s = \varepsilon\vec{v} = \frac{K}{\mu}(-\nabla p + \rho\vec{g}) \qquad (27)$$

where*:*

- $\vec{v}_s$ is Darcy's velocity $[m/s]$;
- ε is the soil porosity;

- K is the air permeability coefficient $[m^2]$.

Equation (28) represents the mass conservation of the gases considering diffusion and gas leakage, with i=1 for air and i=2 for leaked gas.

$$\frac{\partial}{\partial t}(\varepsilon\rho C_i) + \nabla.(\rho C_i \vec{v}_s) = \nabla\left(D_{ij}\nabla\rho C_i\right) + \rho_i Q_i \qquad (28)$$

where*:*

- C_i is the concentration of the gas with component i in weight %
- D_{ij} is the Fick's diffusion coefficient of the gas with component i diffusing in the air component j $[m^2/s]$;
- Q_i is the gas with component i leakage rate $[L/s]$.

By expressing Equation (28) for the leaked gas (i=2) and with D_{12}=D_{21}=D, Equation (29) is obtained, which governs the change of gas concentration.

$$\frac{\partial}{\partial t}(\varepsilon\rho C_2) + \nabla.(\rho C_2 \vec{v}_s) = \nabla(D\nabla\rho C_2) + \rho_2 Q_2 \qquad (29)$$

The equation of mass conversation for mixed gas is obtaining by summing Equation (28) for the leaked gas and air.

$$\frac{\partial}{\partial t}(\varepsilon\rho) + \nabla.(\rho \vec{v}_s) = \nabla(D\nabla\rho) + \sum_i \rho_i Q_i \qquad (30)$$

The equation of state assuming ideal gas behavior can be expressed as:

$$p = \sum_i \frac{\rho_i RT}{M_i} = \frac{\rho RT}{M} \qquad (31)$$

Where*:*

- R is the universal gas constant $[J/mol.K]$;
- T is the absolute temperature $[K]$;
- M_i is the molecular mass of the gas with component i $[kg/m^3]$;

- M is the average molecular weight of the mixed gas $[kg/m^3]$.

By substituting Equations (27) and (31) into Equation (30), we obtain

$$\frac{\partial}{\partial t}\left(\frac{\varepsilon M}{RT}p\right) + \nabla.\left\{\frac{\rho K}{\mu}(\nabla p - \rho\vec{g})\right\} = \nabla(D\nabla\rho) + \sum_i \rho_i Q_i \qquad (32)$$

Equation (33) is used in order to convert Equation (32) into Equation (34) by using p'

$$p = p' + p_o + \rho_s(\vec{g}.\vec{r}) \qquad (33)$$

$$\frac{\varepsilon M}{RT}\frac{\partial}{\partial t}(p') + \frac{\varepsilon p}{RT}\frac{\partial}{\partial t}(M) - \nabla\left[\frac{\rho K}{\mu}\{\nabla p' - (\rho - \rho_s)\vec{g}\}\right] = \nabla(D\nabla\rho) + \sum_i \rho_i Q_i \qquad (34)$$

where*:*

- p' is the pressure difference from the atmospheric pressure;
- p_o is the atmospheric pressure;
- r is the position vector from the reference point;
- ρ_s is the atmospheric density.

The Wilke equation is used to estimate the viscosity coefficient of the mixed gas[23]

$$\mu = \sum_i \frac{\mu_i}{1 + \sum_{j\neq i}\frac{\phi_{i,j}x_i}{x_j}} \qquad (35)$$

where,

$$\phi_{i,j} = \frac{\left\{1 + \left(\frac{\mu_i}{\mu_j}\right)^{0.5}\left(\frac{M_j}{M_i}\right)^{0.25}\right\}^2}{2\sqrt{2\left(1 + \frac{M_i}{M_j}\right)^{0.5}}} \qquad (36)$$

2.1.1.3.3 Verification

A full-scale experiment was designed with a scale found commonly in chemical plants. An earthen tank was built with the dimension of around10x10x2 m and 10x10x3 m, and a gas leaking point was placed 1.2 m below the ground surface. Two different gases were used in order to test the effect of specific gravity on diffusion. The gases used were methane, which has a specific gravity lower than air, and propane-air 13-A (propane vol% 60%, air vol% 40%) which has a specific gravity higher than air. The experimental setup used for the methane experiment is shown in Figure 10 and the experimental setup used for the propane air mixture is shown in Fig XX. The leak rates used were 300-1000 cm^3/min with a pressure of 0.2 kPa. The data were collected using thermal conductivity sensors. The experimental results were then used to check the applicability of the analytical tool mentioned earlier. The results of the experimental data along with the simulation predicted results are shown in Figure 12 and Figure 13.

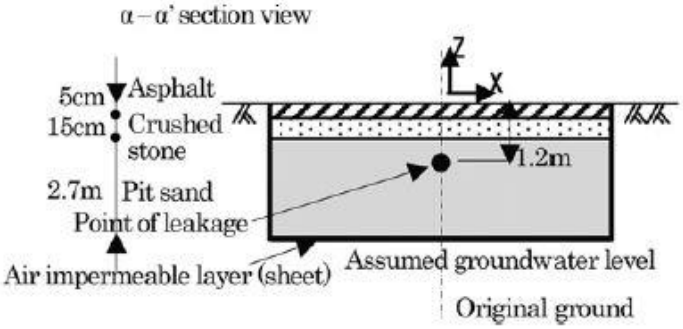

Figure 10 Experimental set-up for the methane experiment by Okamoto and Gomi Reprinted from [22]

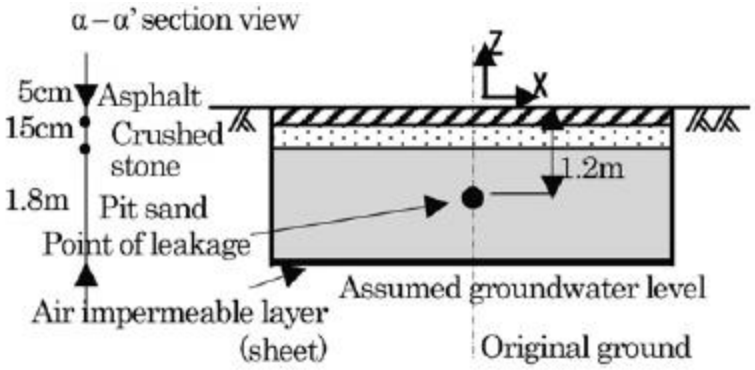

Figure 11 Experimental set-up for the propane-air experiment by Okamoto and Gomi Reprinted from [22]

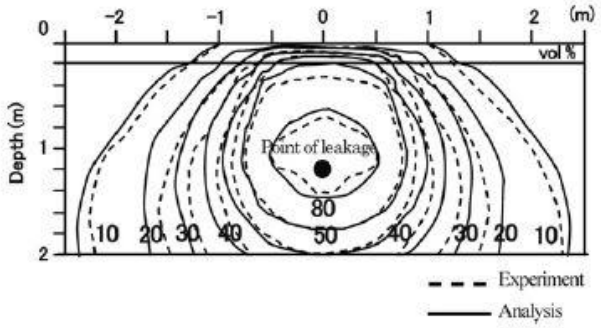

Figure 12 Methane vol% from experimental and model results after 240 hrs Reprinted from [22]

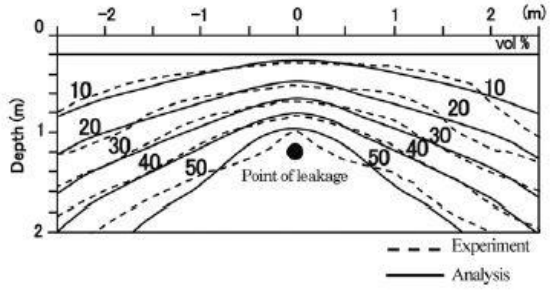

Figure 13 Propane-air 13-A vol% from experimental and model results after 240 hrs Reprinted from [22]

2.1.1.3.4 Findings

The following results were obtained:

- in high concentration zones, methane mainly diffuses upwards, while propane mainly diffuses downwards;
- in low concentration zones, the trend is not conspicuous and specific gravity has less impact;
- methane diffuses downwards and propane diffuses upwards despite specific gravity;
- in low concentration zones, methane rises over the ground surface, while it's relatively less notable with the propane-air mixture that is heavier than air;
- Darcy's law and Fick's law advection and diffusion models can be used on a full scale underground pipeline.

2.1.1.4 Parvini and Gharagouzlou 2015

According to Parvini and Gharagouzlou [5], most of the work that has been done on modelling focused on atmospheric gas dispersion. As a result of that, the goal of their

project was to derive consequence models for a gas that leaks from underground pipelines. The gas used in modelling and later on validating through experiments was hydrogen. The project involved two phases of modelling, a near-field and a far-field model. The near-field model was concerned with the diffusion of gas from the pipeline through the pores of the soil. The outcome of the near-field model was then used as an input to the far-field model, which was about the dispersion of gas through the atmosphere. The laws used in order to perform the modelling were Darcy's law, continuity equation, and concentration equations.

2.1.1.4.1 Assumptions

The assumptions used to develop the model were:

- the leakage rate is low;
- the ground is porous and stable.

2.1.1.4.2 Equations

According to Darcy's law, pure flow through a porous medium can be described as:

$$u = (-\frac{k}{\mu})\nabla P \qquad (37)$$

where*:*

- u is Darcy's velocity $[m/s]$;
- k is the porous environment permeability $[m^2]$;
- μ is the fluid dynamic viscosity $[Pa.s]$;
- P is the fluid pressure $[Pa]$.

Darcy's two-phase law is obtained by combining Darcy's law with the continuity equation.

$$\frac{\partial}{\partial t}(\rho\varepsilon_p) + \nabla.(\rho u) = 0 \qquad (38)$$

By combining Equations (37) and (38), one obtains:

$$\frac{\partial}{\partial t}(\rho\varepsilon_p) + \nabla.\rho[-(k/\mu)\nabla P] = 0 \qquad (39)$$

where*:*

- ρ is the fluid's density $[kg/m^3]$;
- ε_p is the void fraction, that is, the part of volume occupied by pores .

For a variable saturated porous environment, the component transfer can be expressed using Equation (40):

$$\frac{\partial}{\partial t}(\theta c_i) + \frac{\partial}{\partial t}(\rho_b c_{p,i}) + \frac{\partial}{\partial t}(a_v c_{G,i}) + \nabla.(c_i u) = \nabla[(D_{Di} + D_{e,i})\nabla c_i] \qquad (40)$$

with $\rho_b = (1-\varepsilon)\rho_p$ and $a_v = \varepsilon - \theta$,

where*:*

- θ is the fluid volume fraction;
- c_i is the gas concentration of gas component i in liquid $[mole/volume\ of\ fluid]$;
- c_p is the absorbed amount to solid particles $[mole/solid\ dried\ unit\ weight]$;
- c_G is the concentration in gas phase $[mass/gas\ volume]$.
- ρ_b is the solid phase density $[kg/m^3]$;
- ε is the porosity;
- a_v is the gas volume fraction;
- D_D and D_e denote component dispersion due to mechanical mixture and due to diffusion and evaporation $[m^2/s]$.

By expanding terms relative to time in Equation (40), one obtains.

$$\frac{\partial}{\partial t}(\theta c_i) + \frac{\partial}{\partial t}(\rho_b c_{p,i}) + \frac{\partial}{\partial t}(a_v c_{G,i}) = (\theta + \rho_b k_{p,i} + a_v k_{G,i})\frac{\partial c_i}{\partial t} + (1 - k_{G,i})c_i \frac{\partial \theta}{\partial t} - (\rho_p c_{p,i} - k_{G,i} c_i)\frac{\partial \varepsilon}{\partial t} \quad (41)$$

with $k_{p,i} = \frac{\partial c_{p,i}}{\partial c_i}$ and $k_{G,i} = \frac{\partial c_{G,i}}{\partial c_i}$,

where*:*

- $k_{p,i}$ is the absorption isotherm;
- $k_{G,i}$ is the linear evaporation.

Equation (40) can be written as:

$$(\theta + \rho_b k_{p,i} + a_v k_{g,i})\frac{\partial c_i}{\partial t} + (1 - k_{G,i})c_i \frac{\partial \theta}{\partial t} - (\rho_P c_{P,i} - k_{G,i} c_i)\frac{\partial \varepsilon}{\partial t} + \nabla.(c_i u) = \nabla.\left[(D_{D,i} + D_{e,i})\nabla c_i\right] \quad (42)$$

In the case of a saturated porous environment, Equation (43) can be used.

$$(\varepsilon + \rho_b k_{p,i})\frac{\partial c_i}{\partial t} + (c_i - \rho_P c_{P,i})\frac{\partial \varepsilon}{\partial t} + \nabla.(c_i u) = \nabla.\left[(D_{D,i} + \theta_{\tau_{F,i}} D_{F,i})\nabla c_i\right] \quad (43)$$

2.1.1.5 Verification

The model was verified using experimental data from work done by Okamoto et al. [24], who made multiple experiments on hydrogen diffusion through soil. A 10x2x2 m test ground was prepared, and a pipeline was buried at 1.2m below surface. The gas was leaked with a pressure of 0.2 kPa, with a flow rate of 1000 cm^3/min. Figure 14 shows their experimental set-up, while Figure 15 shows the comparison between the model and the experimental data.

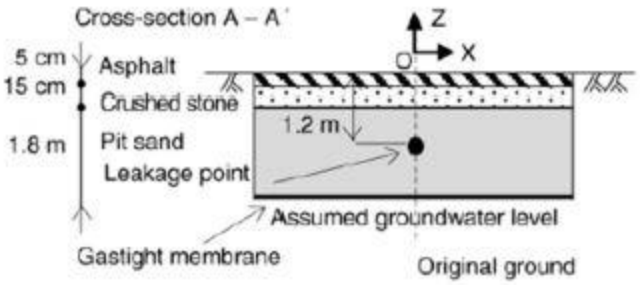

Figure 14 Experimental set-up used to validate Parvini and Gharagouzlou's model Reprinted from [5]

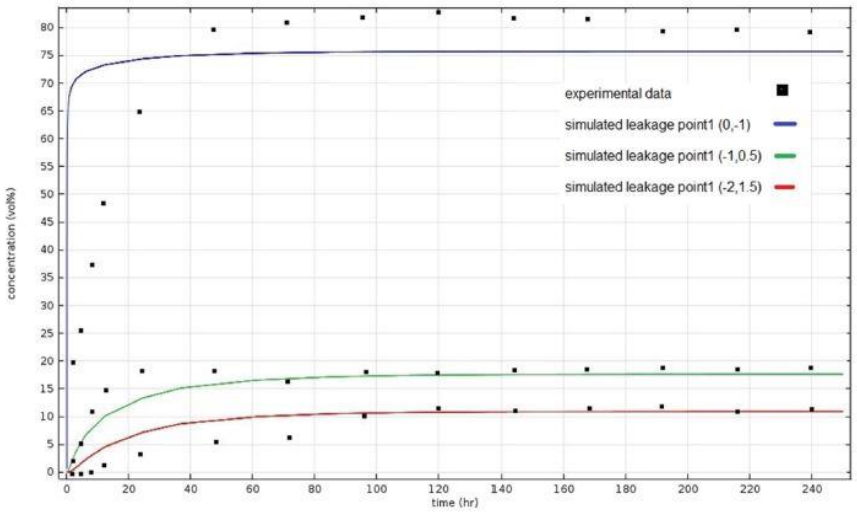

Figure 15 Hydrogen concentration from experimental data and model results Reprinted from [5]

2.1.1.5.1 Findings

The authors believe that the model showed "good" agreement with the previously referenced experimental data. The paper also states other findings considering dispersion through the atmosphere, which is not the point of interest in this research.

2.1.1.6 Diffusion Models Summary

Table 1 shows a summary of the previously mentioned diffusion models.

Table 1 Diffusion models summary

Paper	Equations	Assumptions
Wakoh and Hirano [6]	*Diffusion Convection equation. *Gas concentration for diffusion in a spherical pattern. *The radius of the convection phase.	*the flow rate of the leaking gas remains constant; *the leak pressure is near atmospheric; *the gas leaks in a spherical pattern; *the porosity of the soil and the diffusion coefficient of the gas are constant; *the soil is homogenous; *the gravity and the density variations of the gas in the soil are negligible; *no gas present in the soil before the leak.
Hibi et al. [11]	*Darcy's law. *Continuity equation. *Dusty gas model.	*gas slippage does not occur; *the gas is slowly moving through the soil; *ideal gas behavior; *dispersion is not considered;

Table 1 Continued

Paper	Equations	Assumptions
Okamoto and Gomi [22]	Equation of motion. *Darcy's law. *Continuity equation. *Equation of state (ideal gas).	*a volume element is integrated and averaged over a volume larger than the pore size but smaller than the whole ground; *low pressure so the soil is not moving; *the soil volume is constant; *the present gases are only air and the leaked gas; *the gas flow is laminar; *the process is at steady state; *the gas behaves as an ideal gas.
Parvini and Gharagouzlou [5]	*Equation of motion. *Darcy's law. *Continuity equation. *Component transfer equation in porous environment.	*the leakage rate is low; *the ground is porous and stable.

2.1.2 Experimental Work Involving Underground Gas Flow

Various experiments were conducted to study the diffusion of gas through soil. However, many of them were on a small scale, and only a few of them were large enough to emulate real life conditions.

2.1.2.1 Yan et al. 2015

Yan et al. [25] performed an experiment on a larger scale relative to other experiments. An Earthen tank has been built with the dimensions of 5x5x3 m. A pipeline with a diameter of 0.2 m and a length of 1 m was then laid on the centerline 0.9 m below the surface. The pipeline had four 5 mm leak points in different locations, and these points were controlled by a solenoid valve. Concentration measuring devices were installed at various locations throughout the soil in order to measure the change of the concentration with time. The sensor location coordinates are shown in Table 2. The experiment was conducted with various leak flow rates ranging from 3 L/min to 24 L/min and with various leak point orientations being upwards, downwards, left and right of the pipeline. The gas used in the experiment was methane. For higher flow rates, the experiment was conducted only for a specific period of time, while for the lower flow rates, the system was allowed to reach steady state. The outcome of the experiment was a set of concentration vs. time data at different locations from the leak point. The schematic of the experiment is shown in Figure 16. An example of the results from the experiment for a leak rate of 24 L/min is shown in Figure 17.

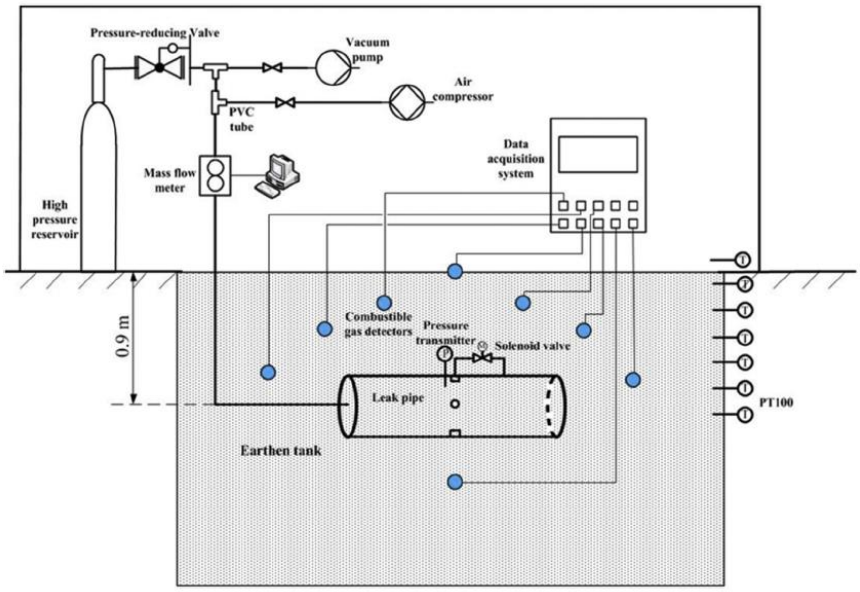

Figure 16 Schematic of Yan et al. experimental set-up Reprinted from [25]

Table 2 Sensors numbers and locations in the Yan et al. experiment Reprinted from [25]

Location	**1**	**2**	**3**	**4**	**5**	**6**	**7**	**8**	**9**	**10**	**11**	**12**	**13**	**14**	**15**
X(m)	-0.1	0.1	-1.5	1.5	0	-2.1	1.5	1	1	-1	-1	0	0.8	0	0
Y(m)	0	0	0	0	-1.5	2.1	-1.5	1	-1	1	-1	0.8	0	-0.8	0
Z(m)	2	2	0.8	0.8	0.8	0.8	0.8	0.5	0.5	0.5	0.5	0.3	0.3	0.3	0

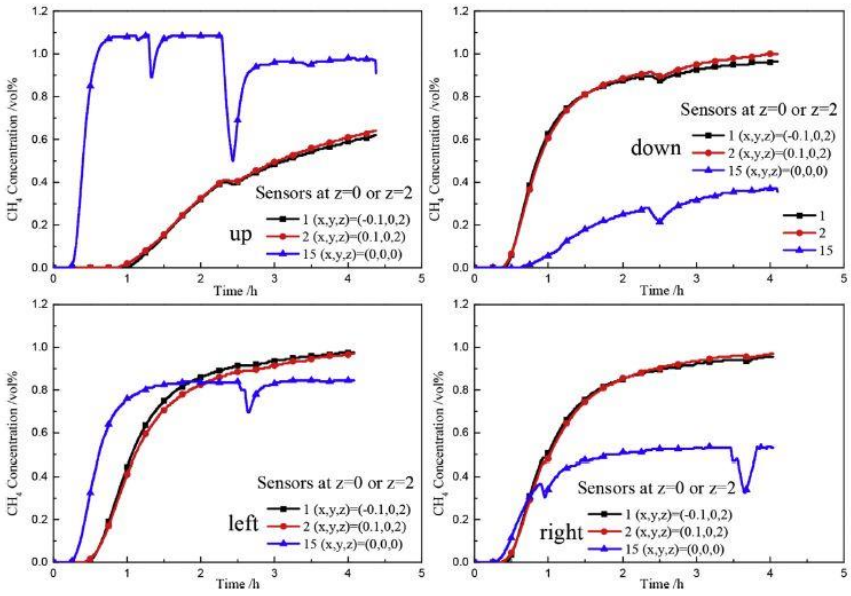

Figure 17 Experimental results for a flow rate of 24 L/min at different locations Reprinted from [25]

2.2 Fluidization

When the leak rate of the underground gas increases, eventually the soil particles would start moving, and the flow regime would be similar to fluidization. Fluidization can be defined as the process where solid particles are in a fluid like state, due to the force exerted on them by a gas or a liquid. Fluidization can be in different forms depending on the velocity of the exerted fluid on the solids, and on whether the fluid is gas or liquid. Figure 18 shows an example of different particle fluidization behavior for different scenarios.[26] In the fluidization stage, the soil is moving, but the gas flow rate is not high enough to displace the soil above the surface level. Most of the literature about fluidization focuses on process applications, especially chemical reaction engineering, and not much is found regarding internal underground fluidization. Also, most of the literature found in fluidization is about a uniform side inlet with multiple release points, and not a single point of release which is the case for an underground pipeline rupture.

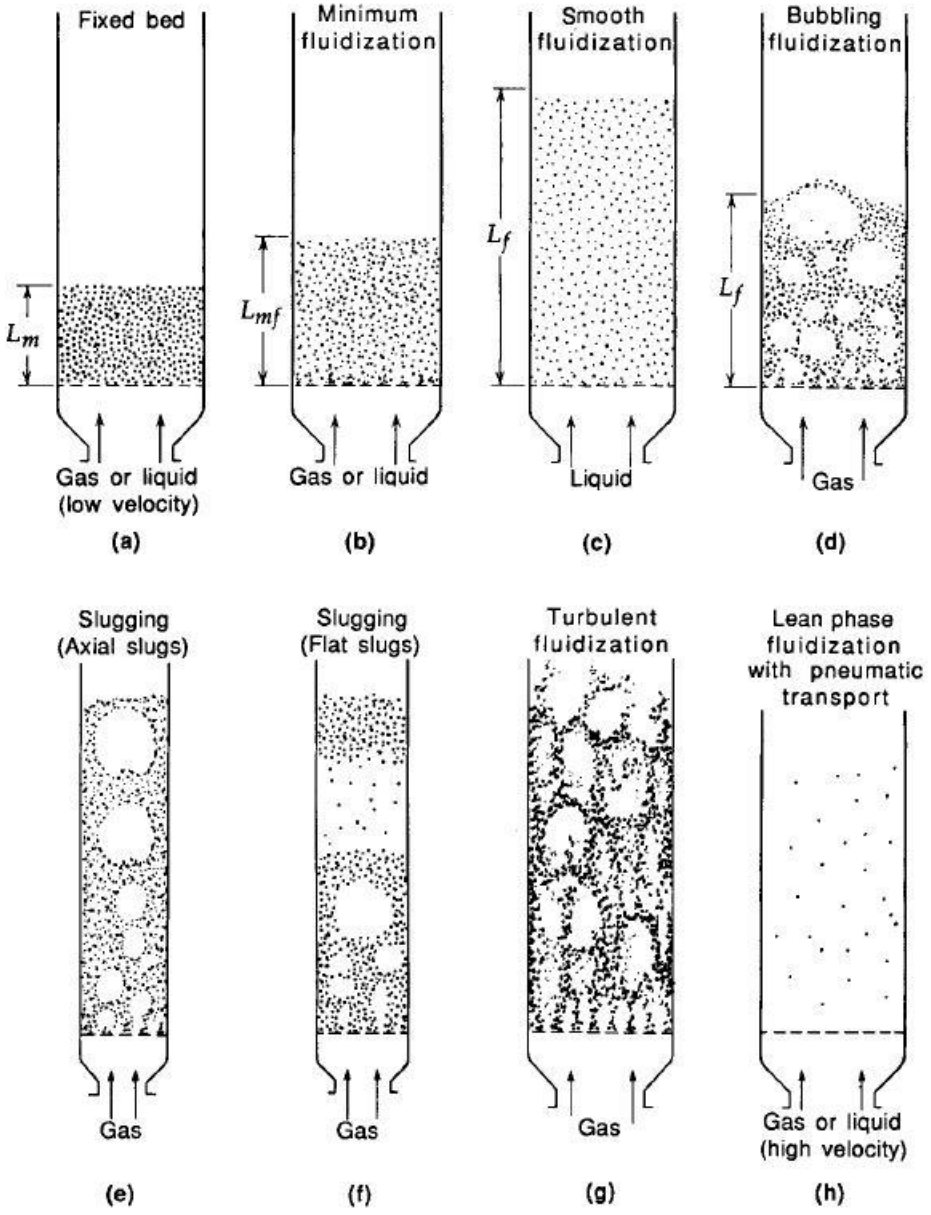

Figure 18 different particle fluidization behavior for different scenarios Reprinted from [26]

According to Alsaydalani et al. [27], there was no recognition of internal fluidization in the geotechnical literature and no systematic analysis for internal diffusion. In addition, there are only limited research done elsewhere that concerns granular internal fluidization

subject to a localized flow. The authors mention as well that internal fluidization is expected to happen for granular and uniform materials, and that other materials, such as clay, would be resistant to it and instead would undergo hydraulic fracture and erosion. From the literature review Asaydalani et al. [27] performed, they have deduced the following:

- with a low gas flow rate, no fluidization occurs when the gas flows through the granular material;
- at the previously mentioned condition, the gas flow might be partially blocked. According to Massimilla et al. [28], there will be no occlusion if the solid is less than 30% by total volume;
- Darcy's law can be applicable at very low gas flow rates, but at higher rates it is not applicable; [29]
- with an increased flow rate, after some point the soil in contact with the orifice will start fluidizing. The pressure required to initiate fluidization for an upward flow can be predicted. For example, Shi et al. [30] and Peng and Fan [31] have proposed models to predict the required pressure incorporating Ergun's equation; [32]
- when fluidization starts, a restricted fluidized zone is developed. The zone is enclosed by a moving layer within stagnant particles. The shape of the zone and the way it develops are not well known, but they probably depend on the orientation of the orifice; [33]
- at higher flow rates, at a certain point the fluidized phase will be injected out to the free surface, and the orifice will become visible. [34]

There are multiple mathematical correlations in the literature that describe fluidization. However, these correlations have a specific application, and there is a lack of a universal model that applies to all kinds of fluidization. [35] Philippsen et al. [36] mention some of the models used to model fluidization including the hydrodynamic model, transport phenomena, and numerical simulation.

2.2.1 Hydrodynamic Model

Hydrodynamic models describe the following:

- the motion and distribution of the solids;
- the gas-solid mixture;
- the particle size;
- the fluid velocity;
- the growth of bubbles;
- the relation between bubble and emulsion phases;
- the mass transfer phenomena;
- the heat transfer phenomena.

The model is controlled by the balance of forces between the particles and the gas velocity. At low gas velocities, the bed acts as a fixed bed, and when the velocity is higher than the minimum fluidization velocity, the particles start moving. It is possible to reach the wanted fluidization regime by changing the gas velocity. The relation between gas velocity and the pressure drop also characterizes the fluidized bed. The pressure drop increases linearly with the gas velocity in the case of a fixed bed. This relation continues until the forces balance between the gas flow and the particles weight. The velocity when that occurs is called the minimum fluidization velocity. Fluidization is also dependent on the size and shape of the solid particles. [36]

2.2.2 Transport Phenomena

The heat and mass transfer phenomena occur when there is contact between the different phases. The heat and mass transfer coefficients become larger with larger contact points between the phases. The transfer happens in two ways, one of which is the transfer between the gas and the solid particles, and the other is the transfer between the bed phases including bubbles, cloud, and emulsion. The second way only occurs in fluidized beds. Hence, modeling the bubbles hydrodynamics in bubbling fluidized beds is important, since that bubbles contribute to turbulence that affects the transfer phenomena. [36]

2.2.3 Numerical Simulation

Fluidized bed numerical simulation is based on mass conservation, energy conservation, and momentum equations, along with the equations that describe phase interactions. Some models were developed to describe gas-solid fluidized beds such as Lattice-Boltzmann, Discrete Particle Model, and Two Fluid Model. [36]

2.3 Crater Formation

At a certain flow rate, the gas flowrate is high enough to lift the soil on top of the leak point leading to a crater formation. While modeling gas dispersion in the case of a crater would be similar to modeling dispersion through the atmosphere, knowing the dimensions of the crater and the conditions of occurrence is required. Figure 19 shows a cross-sectional view of the crater dimensions. Various factors affect the size of the crater, such as the soil type, the pipeline pressure, and the diameter of the pipeline. The event of a rupture of a high pressure pipeline can be complex, since that the crater size also depends on factors related to the incident. These factors include the mode of failure, the location of failure, the relative flow from the pipeline ends, and the misalignment of the ends in case of a full bore rupture. Thus, some approximations might be needed in order to estimate the crater dimensions. There are a few models available to predict the crater dimensions, and most of them are empirical models. [37][38]

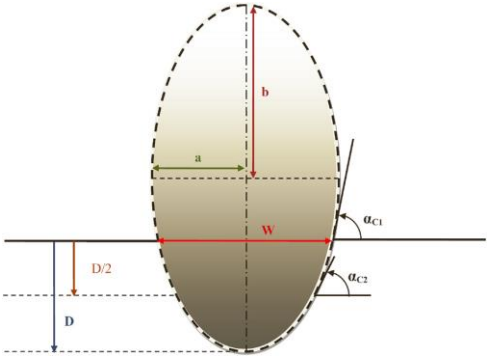

Figure 19 Cross sectional view of a crater Reprinted from [37]

2.3.1 Gasunie Model

The model is an empirical correlation developed by a Dutch company to find out the dimensions of the crater. The pipeline diameter, the pipeline underground depth, and a qualitative description of the soil are required input information to use the model. The assumptions used in developing the model and the equations developed are shown below.[37]

2.3.1.1 Assumptions:

- the soil is considered as a homogenous medium;
- the two ends of the pipeline are separated after the rupture;
- the crater formation occurs in two steps: initial soil displacement of the soil near the pipeline, then the erosion of soil due to gas flow.

2.3.1.2 Equations:

2.3.1.2.1 Crater depth:

For pipeline rupture on the top, the depth can be defined as:

$$D = D_p + D_c \qquad (44)$$

For a full-bore rupture, the depth can be defined as:

$$D = \begin{cases} 4.3D_p + D_c, & if\ w \leq 0.6 \\ \dfrac{R(w)D_p}{0.3} + D_c, & if\ 0.6 < w < 2 \\ 2.2D_p + D_c & if\ w \geq 2 \end{cases} \quad (45)$$

where*:*

- D is the crater depth;
- D_p is the pipeline diameter;
- D_c is the depth of cover;
- w is a soil parameter dependent on soil type.

The values of w are dependent on the type of soil in use and are shown in Table 3.

Table 3 w values based on soil types and the corresponding calculated crater angles Reprinted from [37]

Type of soil	$\boldsymbol{w}$	$\boldsymbol{\alpha_{c1}}$	$\boldsymbol{\alpha_{c2}}$
Very dry sand	0.75	60	29
Sand or dry mixed oil	1.10	65	35
Mixed soil or gravel	1.75	70	45
Humid mixed soil, clay or rock	2.70	75	57
Heavy clay	5.00	80	73

The function $R(w)$ can be computed with:

$$R(w) = 0.28 + 0.62(5 - w) - 0.07(25 - w^2) \quad (46)$$

The crater angles can be computed using:

$$\alpha_{c1} = tan^{-1}(w + 1) \quad (47)$$

$$\alpha_{c2} = tan^{-1}\left[\left(\frac{2.8 + 0.5w}{10}\right)(w + 1)\right] \quad (48)$$

2.3.1.2.2 Crater Width:

The crater width CW can be obtained using:

$$CW = 2a\sqrt{1 - \frac{(b - D)^2}{b^2}} \quad (49)$$

where a and b can be obtained with:

$$\tan \alpha_{c1} = \frac{b}{a}\sqrt{\left(\frac{b}{b - D}\right)^2 - 1} \quad (50)$$

$$\tan \alpha_{c2} = \frac{b}{a}\sqrt{\left(\frac{b}{b - 0.5D}\right)^2 - 1} \quad (51)$$

2.3.1.3 Limitations

The model has the following limitations:

- the model neglects the pipeline's operating pressure, which makes it overestimate the crater width for low operating pressure, and underestimate the crater width for high operating pressure;
- the model includes no correlation for the crater length;
- qualitative soil characterization leads to inaccuracy.

2.3.2 Battelle Model

The Battelle model was developed by the Battelle Institute in order to improve the Gasunie model mentioned above. The model shows an improvement from the Gasunie model by incorporating the pipeline's operating pressure into the equations, and by giving a

quantitative description of the soil. The assumptions and equations used to develop the model are shown below.[37]

2.3.2.1 Assumptions

- the correlations have been derived by considering that the physics governing crater formation due to a pipeline rupture are similar to the one where a crater is formed due to a chemical explosion;
- the Gasunie depth correlations are valid and used in this correlation.

2.3.2.2 Equations

For an infinitely long buried explosive with an incompressible fluid as the medium, the outburst speed can obtained with:

$$u_x = \sqrt{\frac{2\rho Q_w}{3\rho_{soil}}} \qquad (52)$$

where*:*

- u_x is the outburst speed;
- ρ is the gas density;
- Q_w is the explosion energy per unit mass;
- ρ_{soil} is the soil density.

The energy per unit mass of explosion can be obtained with:

$$Q_w = \frac{c^2}{2(\gamma^2 - 1)} \qquad (53)$$

where*:*

- c is the speed of sound;
- γ is the specific heat ratio of the gas.

The width of the crater can be obtained with:

$$CW = 2\sqrt{\frac{D_p\left(D_c + \frac{D_p}{2}\right)u_x}{u_{kr}} - \left(D_c + \frac{D_p}{2}\right)^2} \quad (54)$$

The critical velocity to displace the soil u_{kr} can be obtained with:

$$u_{kr} = \sqrt{\frac{2A_{dyn}}{\rho_{soil}}} \quad (55)$$

Where A_{dyn} is the work required to displace a unit of volume of mass of soil.

2.3.2.3 Limitations

The model has the following limitations:

- the depth calculations use qualitative soil characteristics, while the crater width calculations use quantitative values;
- the model lacks a correlation for crater length.

2.3.3 Advantica Model

The model was developed by GL Noble Denton, formerly known as Advantica. The developers conducted a set of 12 experiments using a test rig designed to simulate a puncture in a buried natural gas transmission pipeline. Three different types of soil were defined as clay soil, sandy soil, and mixed soil. The operating pressure ranged from 20 – 120 bar and the hole size varied from 25 mm to 80 mm. The dimensions of the craters formed after each experiment were measured. The developers did not report the crater width, and reported the recommended separation distance in the case of having parallel pipelines. However, according to Silva et al. [37] the maximum width of the crater can be assumed to be twice as much as the separation distance, since that the Advantica developers stated that the distance has been recorded from the centerline of the first pipeline to the nearest point on the parallel pipeline. Silva et al. then used the same data

to produce new figures in terms of crater width instead of separation distance as shown in Figure 20. [39]

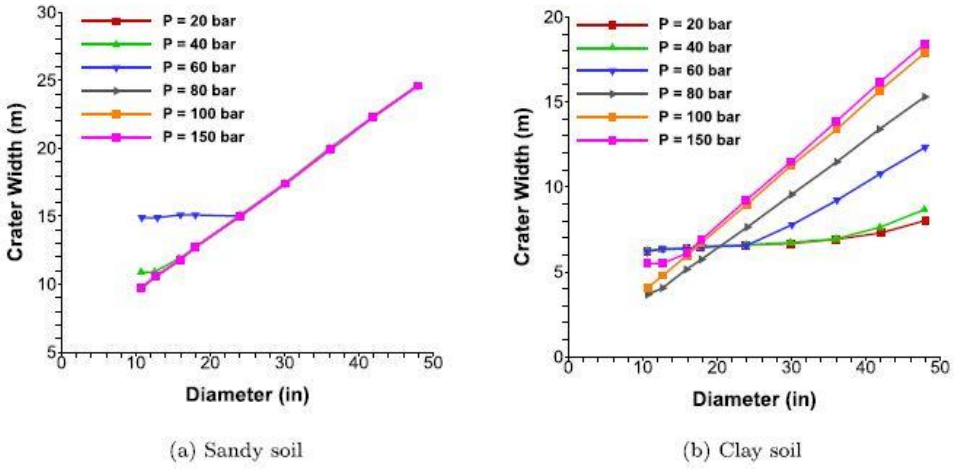

Figure 20 Example of experimental data on crater size Reprinted from [37]

2.3.3.1 Equations

The Advantica model provided only experimental data resulting from the 12 experiments. Silva et al. [37] then adding the crater width information by assuming it is double the separation distance obtained a general equation governing the data by using linear regression.

$$CW_i = n_i D_p + m_i \qquad (56)$$

The empirical correlation constants (n_i and m_i) depend on the type of soil, and the pipeline operating conditions. Table 4 below shows the list of correlations throughout different scenarios.[37]

Table 4 Empirical correlation constants value for different conditions Reprinted from [37]

Soil Type	Pressure (bar)	Diameter (in)	Correlation
Sandy soil	20	Any	$CW = 0.3999D_p + 5.4695$
	40	≤12.8	$CW = -10^{-14}D_p + 10.875$
		>12.8	$CW = 0.3934D_p + 5.7275$
	60	≤24.0	$CW = 0.0278D_p + 14.6060$
		>24.0	$CW = 0.3927D_p + 5.8000$
	80-150	any	$CW = 0.3999D_p + 5.469$
Clay soil	20	≤36.1	$CW = 0.0237D_p + 6.0135$
		>36.1	$CW = 0.093D_p + 3.4989$
	40	≤36.0	$CW = 0.0258D_p + 5.9839$
		>36.0	$CW = 0.1445D_p + 1.6881$
	60	≤24.0	$CW = 0.0237D_p + 5.9989$
		>24.0	$CW = 0.2437D_p + 0.5545$
	80	any	$CW = 0.3148D_p + 0.1522$
	100	any	$CW = 0.3710D_p + 0.0842$
	150	≤12.6	$CW = -0.0075D_p + 5.811$
		>12.6	$CW = 0.3562D_p + 1.000$
Mixed soil	≤80.0	≤36.1	$CW = 0.0244D_p + 10.276$
		>36.1	$CW = 0.1946D_p + 4.0742$

2.3.4 Accident-Based Model

The model was developed by Silva et al. [37] using reported incident data on which a crater formation has occurred. The data were collected from 48 different incidents from various databases. The data was inputted in a linear regression software called STATISTICA and a correlation between crater width and the pipeline diameter, the operating pressure, the depth of cover, the specific heat ratio of the gas, and the density of the soil was obtained. The obtained correlation is shown in Equation (57).[37]

$$CW = 33.646 + 0.315D_p + 0.056P + 3.995D_c - 8.304\gamma - 0.017\rho_{soil} \quad (57)$$

2.4 CFD Models

One of the ways to predict the pattern of gas flow through soil is using Computational Fluid Dynamics (CFD) models. CFD is used to analyze systems involved with fluid flow and heat transfer and other phenomena such as chemical reactions. CFD has many applications in the industry such as aerodynamics of vehicles, mixing and segregation processes, and chemical reactors. The codes of CFD are implemented in three different elements, the preprocessor, the solver, and the post-processor. In the pre-processor stage, the system is set-up by defining the geometry and generating the grid for it. Then, the appropriate physical and chemical models are selected depending on the system that needs to be simulated. The fluids properties and the boundary conditions are also defined in order to run the codes. The solution of the equations is defined at nodes in each cell. In general, the more cells used in the grid, the more accurate the solution is. However, this also can increase the computational cost, which is the time required by the computer to give a solution. The second stage is the solver. In the solver stage, the governing equations are integrated into the solution domain, then the resulting integral equations are converted into a system of algebraic equations. Finally, the equations are solved by an iterative method. There are various CFD solvers available such as Fluent, CFX, and PHOENICS. The last stage is the post-processor stage. In this stage the results of the simulations are analyzed and, based on them, some outcomes are recorded.[40] Solving via CFD involves using the Navier-Stokes equation to determine the fluid properties at a single node at a single point of time. Then, the data are used as input for other equations such as turbulence models and drag force models. There are two main approaches for numerical simulations for solid-gas systems, which is the case of this thesis. The first is called the Two-Phase method which is an Eulerian-Eulerian approach, in which both the solid, and the gas are considered a continuum, and the particle amount is specified by inputting the volume fraction of the solid. In addition, other constitutive equations are used from the granular theory in order to account for the solid behavior. The other main approach is the CFD-DEM (Discrete Element Method) method, which is an Eulerian-Lagrangian approach, in which the gas is considered a continuum, but the solid is considered a discrete phase. In this method, the

Newtonian equations of motion are solved for each particle using force balance, while the gas is simulated using Navier-Stokes equation.[41], [42] The CFD-DEM approach is considered more accurate since it takes into account the particle-particle and particle-wall collisions, and other particle properties such as elasticity modulus and stiffness coefficient, unlike the Two-Phase approach which doesn't include them.[41] However, the high computation cost associated with CFD-DEM makes it only feasible for dilute solid-phase flow.[43] Most of the CFD work that has been found in literature involved fluidization, and none was found directly related to an underground pipeline release. A general form of the Navier-Stokes equation is shown below.[44]

$$\rho \frac{D}{Dt}\mathbf{v} = -\nabla p + \mu \nabla^2 \mathbf{v} + \rho \mathbf{g} \qquad (58)$$

2.4.1 Turbulence Models

Two-equation turbulence models are used along with the Navier-Stokes equation in order to simulate fluids. The first equation represents the turbulence kinetic energy k. The second one can include any of the following: the dissipation rate of turbulence kinetic energy ε, the specific dissipation rate ω, the length scale l, and others. Some of the turbulence models are shown below. [45]

2.4.1.1 The k-ε Model

The k-ε model is the most used two-equation model in simulations. It is recommended to be used for multi-phase flows, and flows with chemical reactions. The model of Lander and Sharma is as follows:[46]

The kinematic eddy viscosity ν_t equation:

$$\nu_t = C_\mu \frac{k^2}{\varepsilon} \qquad (59)$$

The turbulence kinetic energy k equation:

$$\frac{\partial k}{\partial t} + \bar{u}_j \frac{\partial k}{\partial x_j} = \frac{\partial}{\partial x_j}\left[\frac{(\nu + V_t)}{\sigma_k}\frac{\partial k}{\partial x_j}\right] - \varepsilon + \tau_{ij}\frac{\partial \bar{u}_i}{\partial x_j} \quad (60)$$

The turbulence dissipation ε equation:

$$\frac{\partial \varepsilon}{\partial t} + \bar{u}_j \frac{\partial \varepsilon}{\partial x_j} = \frac{\partial}{\partial x_j}\left[\frac{(\nu + V_t)}{\sigma_\varepsilon}\frac{\partial \varepsilon}{\partial x_j}\right] + C_{\varepsilon 1}\frac{\varepsilon}{k}\tau_{ij}\frac{\partial \bar{u}_i}{\partial x_j} - C_{\varepsilon 2}\frac{\varepsilon^2}{k} \quad (61)$$

with:

$$V_t = l_{mix}^2 \left|\frac{\partial \bar{u}}{\partial y}\right| \quad (62)$$

where:

- $\sigma_k = 1.0,\ \sigma_\varepsilon = 1.3$ are the Prandtl numbers for k and ε;
- $C_\mu = 0.09, C_{\varepsilon 1} = 1.44, C_{\varepsilon 2} = 1.92$ are model constants;
- l_{mix} is the mixing length;
- τ_{ij} is Reynolds turbulence stress.

2.4.1.2 Modified k-ε Model

Various modifications and improvements have been implemented on the k-ε model. The most important two are the realizable k-ε model [47] and the Renormalization Group (RNG) k-ε model. [48]

The realizable k-ε model includes Schwartz inequality for shear stresses and satisfying the realizability constraints on normal Reynolds stresses. In this model C_μ is no longer constant and instead is calculated using an improved eddy-viscosity equation. The other constants also differ in value, being $\sigma_k = 1.0,\ \sigma_\varepsilon = 1.2, C_{\varepsilon 1} = 1.44, and\ C_{\varepsilon 2} = 1.9$. The model showed improvements for jets, mixing layers, and separating streams, compared to the standard k-ε model.

The RNG k-ε model is improved compared to the standard k-ε model by having better ability to predict separating flows and recirculating flows. However, the model fails to

predict flows with acceleration. In this model, $C_{\varepsilon 2}$ is no longer constant and instead is replaced by $C_{\varepsilon 2}$ in equation.

$$C_{\varepsilon 2} \equiv C_{\varepsilon 2} + \frac{C_\mu \eta^3 (1 - \eta/\eta_0)}{1 + \beta_1 \eta^3} \quad (63)$$

with

$$\eta = \frac{Sk}{\varepsilon}, S = \sqrt{2S_{ij}S_{ji}}, S = \frac{1}{2}\left(\frac{\partial \bar{u}_i}{\partial x_j} + \frac{\partial \bar{u}_j}{\partial x_i}\right) \quad (64)$$

where:

- S is the mean strain-rate of the flow;
- S_{ij} the deformation tensor;
- $C_\mu = 0.085, C_{\varepsilon 1} = 1.42, C_{\varepsilon 2} = 1.68, \sigma_k = \sigma_\varepsilon = 0.72, \beta_1 = 0.012, and\ \eta_0 = 4.38.$

2.4.1.3 The k-ω Model

The k-ω model is also a widely used model, and is considered superior to the standard k-ε model. The model is able to predict more accurately for boundary layers with adverse pressure gradients, and is much more accurate for shear flows and separated flows. However, it still has inaccuracies for predicting boundary free flows such as jets. The most recent version of the k-ω model was developed by Wilcox and the equations are as follows:[49]

The kinematic eddy viscosity ν_t equation:

$$\nu_t = \frac{k}{\tilde{\omega}}, \tilde{\omega} = max\left\{\omega, C_{lim}\sqrt{\frac{2S_{ij}S_{ji}}{\beta^*}}\right\}, C_{lim} = \frac{7}{8} \quad (65)$$

The turbulence kinetic energy k equation:

$$\frac{\partial k}{\partial t} + \bar{u}_j \frac{\partial k}{\partial x_j} = \frac{\partial}{\partial x_j}\left[\left(\mathrm{v} + \sigma^* \frac{k}{\omega}\right)\frac{\partial k}{\partial x_j}\right] - \beta^* k\omega + \tau_{ij}\frac{\partial \bar{u}_i}{\partial x_j} \qquad (66)$$

The turbulence dissipation ε equation:

$$\frac{\partial \omega}{\partial t} + \bar{u}_j \frac{\partial \omega}{\partial x_j} = \frac{\partial}{\partial x_j}\left[\left(\mathrm{v} + \sigma \frac{k}{\omega}\right)\frac{\partial \omega}{\partial x_j}\right] - \beta\omega^2 + \frac{\sigma_d}{\omega}\frac{\partial k}{\partial x_j}\frac{\partial \omega}{\partial x_j} + a\frac{\omega}{k}\tau_{ij}\frac{\partial \bar{u}_i}{\partial x_j} \qquad (67)$$

with:

$$a = 0.52, \quad \beta = \beta_0 f_\beta, \quad \beta_0 = 0.0708, \quad \beta^* = 0.09, \quad \sigma = 0.5, \quad \sigma^* = 0.6, \quad \sigma_{d0} = 0.125 \qquad (68)$$

and

$$\sigma_d = \begin{cases} 0, & \frac{\partial k}{\partial x_j}\frac{\partial \omega}{\partial x_j} \le 0 \\ \sigma_{d0}, & \frac{\partial k}{\partial x_j}\frac{\partial \omega}{\partial x_j} > 0 \end{cases}, \quad f_\beta = \frac{1 + 85\chi_\omega}{1 + 100\chi_\omega}, \qquad (69)$$

$$\chi_\omega = \left|\frac{\Omega_{ij}\Omega_{jk}S_{ki}}{(\beta^*\omega)^3}\right|, \quad \Omega_{ij} = \frac{1}{2}\left(\frac{\partial \bar{u}_i}{\partial x_j} - \frac{\partial \bar{u}_j}{\partial x_i}\right)$$

where:

- C_{lim} is the stress-limiter strength;
- f_β is the vortex-stretching function;
- χ_ω is the dimensionless vortex-stretching parameter;
- Ω_{ij} is the mean-rotation tensor.

2.4.2 Two-Phase Model

As stated earlier, the Two-Phase model is an Eulerian-Eulerian approach to simulate multi-phase flow. In this model, both the solid and the fluid are treated as a continuum. The model assumes that the solid behaves as a pseudo-fluid, and the granular features are

obtained using granular theory equations and user input for particle properties. The main equations for an isothermal system are shown below.[50]

Continuity equations:

$$\alpha_g + \alpha_s = 1 \quad (70)$$

$$\frac{\partial}{\partial t}\left(\alpha_g \rho_g\right) + \nabla.\left(\alpha_g \rho_g \vec{u}_g\right) = S_{gs} \quad (71)$$

$$\frac{\partial}{\partial t}\left(\alpha_s \rho_s\right) + \nabla.\left(\alpha_s \rho_s \vec{u}_s\right) = S_{sg} \quad (72)$$

Momentum equations:

$$\frac{\partial}{\partial t}\left(\alpha_g \rho_g \vec{u}_g\right) + \nabla.\left(\alpha_g \rho_g \vec{u}_g \vec{u}_g\right) = -\alpha_g \nabla P_g + \nabla \alpha_g . \tau_g + \alpha_g \rho_g g + \beta\left(\vec{u}_s - \vec{u}_g\right) + S_{gs}\vec{u}_s \quad (73)$$

$$\frac{\partial}{\partial t}\left(\alpha_s \rho_s \vec{u}_s\right) + \nabla.\left(\alpha_s \rho_s \vec{u}_s \vec{u}_s\right) = -\alpha_s \nabla P_s + \nabla \alpha_s . \tau_s + \alpha_s \rho_s g + \beta\left(\vec{u}_s - \vec{u}_g\right) + S_{sg}\vec{u}_s \quad (74)$$

Gas phase stress sensor:

$$\tau_g = \mu_g \left[\nabla \vec{u}_g + \left(\nabla \vec{u}_g\right)^T\right] - \frac{2}{3}\alpha_g \mu_g (\nabla \vec{u}_g) \quad (75)$$

Solid phase stress sensor:

$$\tau_s = \mu_s [\nabla \vec{u}_s + (\nabla \vec{u}_s)^T] - \frac{2}{3}\mu_s (\nabla . \vec{u}_s) + \lambda_s . \nabla . \vec{u}_s \quad (76)$$

Solid shear viscosity and bulk viscosity:

$$\mu_s = \frac{4}{5}\alpha_s\rho_s d_p g_{0,ss}(1+e_{ss})\left(\frac{\theta_s}{\pi}\right)^{0.5} + \frac{\alpha_s\rho_s d_p\sqrt{\theta_s\pi}}{6(3-e_{ss})}\left[1 + \frac{2}{5}(1+e_{ss})(3e_{ss}-1)\alpha_s g_{0,ss}\right] + \frac{P_s sin\varphi}{2\sqrt{I_{2D}}}\lambda_s = \frac{4}{3}\alpha_s\rho_s d_p g_{0,ss}(1+e_{ss})\left(\frac{\theta_s}{\pi}\right)^{0.5} \quad (77)$$

Radial distribution function:

$$g_{0,ss} = \left[1 - \left(\frac{\alpha_s}{\alpha_{s,max}}\right)^{\frac{1}{3}}\right]^{-1} \quad (78)$$

where*:*

- α is the volume fraction;
- S is the source term;
- β is the drag coefficient;
- λ_s is the bulk viscosity;
- d_p is the surface to volume mean diameter $[m]$.

2.4.3 CFD-DEM Model

The CFD-DEM model, as stated earlier, is an Eulerian-Lagrangian approach, where the fluid is treated as a continuum while the solid is considered a discrete phase, and the model equations are applied to each particle individually. In the early stages, the number of particles was several thousands, however, now it is possible to simulate 50,000 to 100,000 particles with a single CPU. This approach is still probably not feasible for very large domains where particles exceed millions. The CFD-DEM is computationally expensive, but it predicts results more accurately compared to the Two-Phase model. The equations used in CFD-DEM for the gas are similar to the ones used in the Two-Phase model

(Equations (71), (73),(75)). For the solid particles, these two following equations are used.[51]

Translational and rotational motion equations of each single particle:

$$m_a \frac{dv_a}{dt} = -V_a \nabla p_g + F_d + m_a g + \sum_{b=1}^{N} (F_{ab,n} + F_{ab,t}) \quad (79)$$

$$I_a \frac{dw_a}{dt} = \sum_{b=1}^{N} (R_b n_{ab} \times F_{ab,t}) \quad (80)$$

with the drag force calculated by:

$$F_d = \frac{(u_g - v_p) V_p \beta}{(1 - \varepsilon_g)} \quad (81)$$

where*:*

- $F_{ab,n}, F_{ab,t}$ are the normal and tangential force components respectively;
- S is the source term;
- β is the phase momentum exchange coefficient.

3 RESEARCH OBJECTIVE

The proper prediction of the consequences of underground pipeline releases requires the understanding of the flow mechanism of the gas leaking through the ground from the buried pipelines. There is currently a clear lack of a universal model that is capable of modeling underground gas release from diffusion (low flow pipeline releases) to crater formation (high flow releases). In addition, all the available crater formation prediction tools are mostly empirical correlations with various assumptions and limitations. Hence, there is a need to understand the underground gas release phenomena in a more fundamental level.

The principal objective of the project is to model the underground releases of hydrocarbon from a buried pipeline.

The proposed work includes the following steps:

- Review of the current state-of-the-art approaches on the modeling of underground gas releases;
- Development of a Computational Fluid Dynamic (CFD) based model that aims to model the gas flow through the ground for different gas flow rates (from low to high flow);
- Study of the effect of the gas release rates and soil properties on the release regime, namely the movement or displacement of the soil;
- Model validation using existing experimental data;
- Identification of the pipeline release rates corresponding to the underground flow regimes boundaries (diffusion, fluidization and crater formation);
- Utilization of model output for consequence modeling.

4 METHODOLOGY

This research involved modelling work shown in the 5 stages listed below.

4.1 Stage 1: Literature Review and Identification of the Knowledge Gaps

This part aims to review historical major accident cases that involve underground releases to identify a necessary scope and limits of the model, which should be able to predict all potential industrial-scale incidents. The review also includes a study of existing underground gas release models and existing experimental data. The investigation of previous work includes the study of diffusion, fluidization effect and crater formation and the identification of the models' limitations. This is followed by identifying the knowledge gaps, and the possible areas of improvement. The typical dimensions and conditions of buried natural gas pipelines were noted from previous incidents, from experimental papers such as Acton et al. [39], and from the local industry in Qatar. This data can be used in order to have a realistic model when simulating an underground gas release.

4.2 Stage 2: Design of a CFD Model for the Simulation of Underground Gas Releases

The underground gas flow was simulated using a CFD software named ANSYS Workbench. The three main steps prior to a simulation are geometry, meshing, and model setup

- *Geometry:*

In this stage, the model is setup first using data given by the industry on the used buried transportation pipeline, which includes the pipe diameter, orifice size, operating pressure, soil type, and pipe depth. The dimensions of the data are then represented by a geometry created using ANSYS DesignModeler. The geometry was set to be a 2-dimensional geometry with two bodies, where the top body represented the atmosphere, and the bottom body where the pipeline lied in represented the soil. A detailed step by step geometry setup is shown in section 5.1.

- *Meshing:*

The system is divided into a number of nodes varying in size based on location, being finer around the inlet, the pipeline, and the interface, and coarser in other locations. This is done by using the ANSYS Meshing software. The modeling equations are solved in each node. An example of the previously mentioned geometry after being meshed is shown in Figure 21. A detailed step by step description for the meshing procedure is shown in section 5.2.

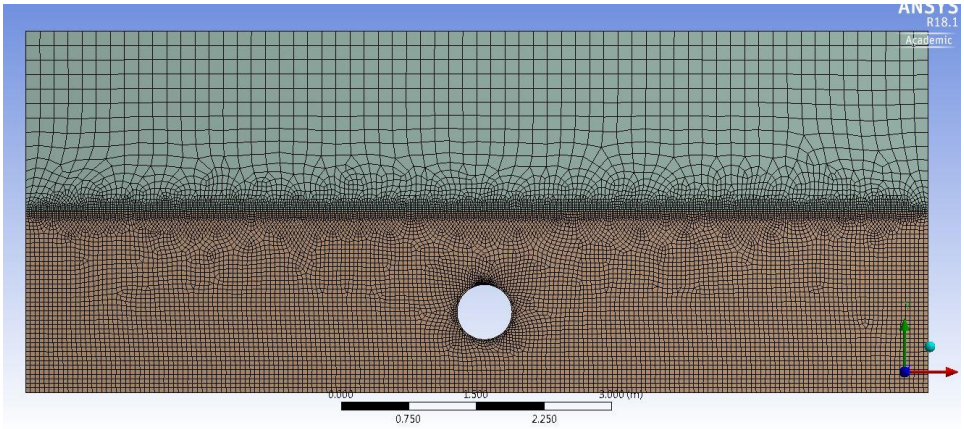

Figure 21 Example of meshed geometry

- *Model set-up:*

The methodology for the CFD Model Set-Up is shown in Figure 22. In the model set-up, various parameters are used as input and various applicable models to the given scenario are chosen, such as the multiphase model, the turbulence model, and the granular viscosity model. In the multiphase model, different phases are set-up for air, soil, and methane. For the turbulence model, the k-ε turbulence model is selected. For the granular viscosity, the Gidaspow model is selected. After inputting boundary conditions and initiating the flow,

the simulation can start running and showing results. Details about the choice of models and running the calculation procedure are presented in section 5.3.

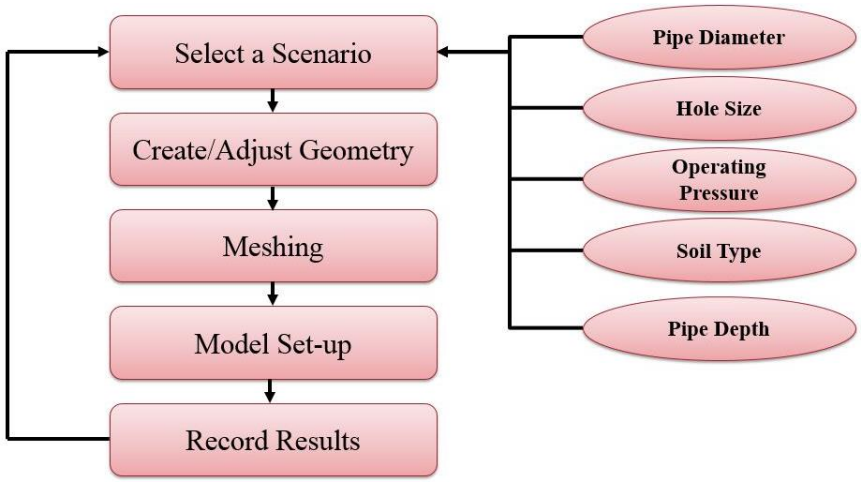

Figure 22 Stage 2 steps

After results are obtained for the first scenario, various parameter are changed to evaluate their effect on the results compared to the original case. The parameters studied are:

- Mesh size: in which various meshing approaches for the designed geometry are examined including different mesh sizes and attempting to use the "Sphere of influence" option;
- Soil viscosity: in which the soil viscosity in the material tab is checked to determine if it has an effect on the results;
- Soil particle diameter: in which the soil particle diameter are examined and compared for the case of having a constant diameter versus a varying particle size distribution, using the population balance model;

- Type of inlet boundary condition: the choices of inlet pressure or inlet velocity as boundary conditions are compared;
- Primary phase selection: in which the choice of the primary phase selected (either air or methane) is examined, and based on the results, the primary phase is selected;
- Inlet velocity: in which the effect of having a different range of velocity values ranging from $2x10^{-2}$ m/s to 15 m/s is evaluated;
- Type of geometry boundary condition: in which the option for using symmetry versus the outlet boundary condition for the side of the geometry in the atmospheric body will be assessed;
- Specific gravity: in which the effect of using fluids other than methane, including hydrogen, ethane, and propane is assessed;
- Presence of soil: in which the difference between having the soil present in the simulation versus having no soil in it, along with its effect on the methane flow is studied;
- Material density: in which the air and methane density values are varied between constant, and using a model such as ideal gas. The results are then compared.

4.3 Stage 3: Model Validation Using Existing Experimental Data

The model is validated using experimental data found in literature review. For the diffusion flow regime, the model is validated using the work by Yan et al. [25] for the case of a gas leak flow rate of 24 L/min. The geometry, mesh, and setup inputs were changed to match conditions provided in their paper. The simulation is run for a time period similar to the experiment. The results from the simulation are compared with the existing experimental data, in order to infer the accuracy of the model.

4.4 Stage 4: Identifying Regimes Boundaries Using the Model

In this stage, the setup uses conditions provided by the industry in Qatar. First, the gas volumetric flow rate for Qatar is estimated and compared to the recorded gas volumetric flow rate provided in the experimental data in the literature. Then, the effect of the fluid velocity and the soil density is studied, and reported in dimensionless form, using

Reynolds' number to represent the fluid velocity and Archimedes' number to represent the soil density. The developed model is executed for various velocity values, starting from very small, with the expectation that no soil movement will be observed (diffusion). The velocity is then slowly increased until noticing a clear soil motion (fluidization). The velocity is again increased until a clear opening from the hole in the pipeline to the atmosphere is seen (crater formation). The velocity ranges in which a change of regime is observed are recorded. The velocity values ranged from 0.1 m/s to 50 m/s. The same procedure is done using different soil density values ranging from 1000 kg/m^3 to 1600 kg/m^3. All the results are compiled in a graph represented by the previously mentioned dimensionless numbers.

4.5 Stage 5: Using the Model's Output as an Input for Consequence Modeling

The output mass flow rate is taken from one of the simulated cases as an example, and then used as an input to the Areal Locations of Hazardous Atmospheres (ALOHA) software, which is a software used for consequence modeling.[52] The source is assumed as a single continuous release point. The threat zone of the possibility of a flash fire will is plotted from the outcome of ALOHA.

5 DESIGN OF A CFD MODEL FOR THE SIMULATION OF UNDERGROUND GAS RELEASE

The simulation of underground gas release from a buried pipeline is done using the software ANSYS Workbench 18.1 which includes ANSYS DesignModeler, ANSYS Meshing, and ANSYS Fluent. Each one of them was used for setting up the model in three consecutive steps: geometry, meshing, and setup.

5.1 Geometry

The first step of simulating a real case scenario is to have our system and domain represent the conditions and dimensions observed in real cases. Since there are plenty of different possibilities of a buried pipeline dimensions, the one most relevant to the local industry in Qatar was chosen. An industrial company in Qatar provided us with the information shown in Table 5. These dimensions will be used in the geometry used setting up the model. Since that the pipeline diameter was not given, the diameter used was obtained by choosing the median diameter from the experimental work of Acton et al.[39] which was 0.61 m. The geometry in this project went through various phases with different levels of capability to use the software. There are three main geometry setups that were used throughout the project represented by phase 1, phase 2, and phase 3. Phase 1 and phase 2 are very similar and the only difference is that in phase 2 more constrictions on the geometry were used and more accurate dimensions were used, due to a better understanding of using the software. Phase 1, and phase 2 geometry were used in the investigation, and testing stages. Phase 3 is a replica of the experimental work done by Yan et al. by utilizing the information given in their description. Phase 3 was used in the model validation stage. The software used to create all the geometry is ANSYS DesignModeler. In all the geometry cases, the system is assumed to be a two dimensional system, since that whatever happens in the third dimension will be the same due to symmetry. This also will simplify the problem and potentially lower the computational cost for running the simulations. The 2D system is divided into two equally sized sections, the top being the atmosphere domain, and the bottom being the soil domain. In the soil domain, the pipeline is located at exactly

the center of the horizontal axis (x axis), while the depth varies along the vertical axis (y axis) depending on the phase. A section on the top of the pipeline is also selected as the inlet source of the gas. A schematic diagram of the system can be seen in Figure 23.

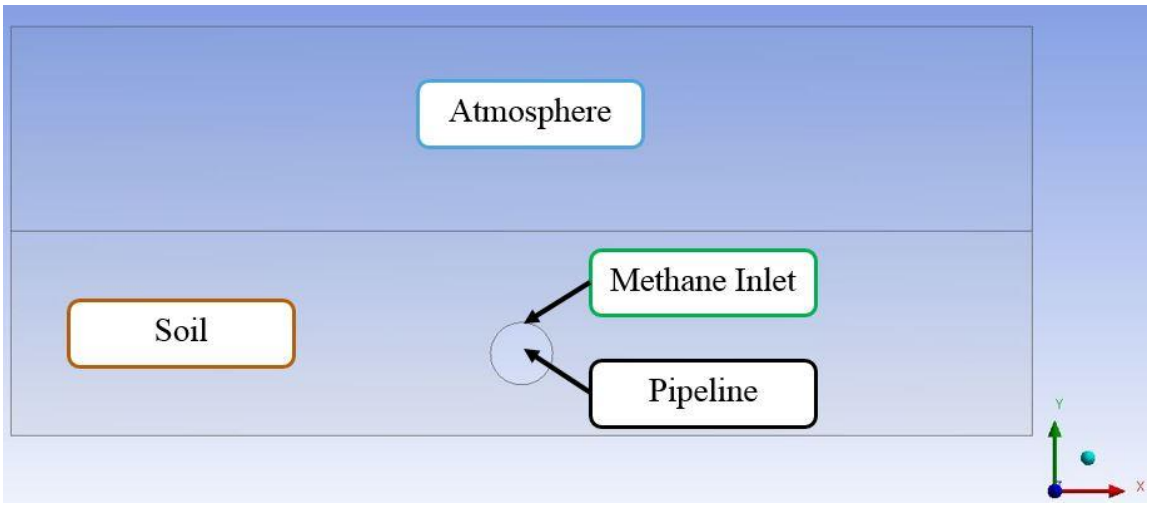

Figure 23 Geometry schematic

Table 5 Pipeline conditions provided by Qatar industry

Parameter	Value
Pipeline Depth	1 to 1.5 m
Operating pressure	80 bar
Operating temperature	15 to 35 ^{o}C
Gas composition	methane 83%, ethane 5%, nitrogen 5%, CO_2 3%, H_2S 2%, propane 1.5%, butane 0.5%

Pipeline thickness	32.6 mm
Hole sizes of interest	0.75’’, 2’’, 4’’, full bore rupture

5.1.1 Phase 1

The whole dimensions of the system are 10 m in the x – axis and 4 m in the y – axis. First, a rectangle is drawn on the positive x and y directions starting from the point (0,0) which is the bottom left corner of the rectangle. Using the same drawing tool, another rectangle is drawn starting from the top left corner point of the previously drawn rectangle, leading to two rectangles drawn on top of each other sharing one side (Top of the first one, and bottom of the second one). Afterwards, the circle option is chosen, the center of the circle is approximately put on the middle of the x – axis, and at approximately 0.8 m in the y – axis (1.2 m below surface). The point was approximated by using the coordinates on the bottom right corner of the software. The circle is then drawn. From the “Modify” tab, using the split option, two points on top of the pipeline were used to approximately split the pipeline into two sections, the inlet hole, and the pipeline wall. The value was approximated to 0.1 m for the inlet section by using the coordinates on the bottom right corner of the software. In order to put an exact value for a part of the already drawn geometry, the dimensions option is selected. The general dimension option is chosen and used on three sides of the drawn rectangles. The value of horizontal side is fixed to 10 m represented by H1. The value of the vertical side of each triangle is 2 m represented by V2, and V3, adding the total vertical length to 4 m. For the pipeline, the dimensions option is used to fix the diameter of the pipeline to 0.61 m represented by D4. A schematic diagram of the geometry is shown in Figure 24. The second part of the geometry creation is to create a surface from the sketch drawn. Using the “Modeling” tab, the sketch drawn is first selected and by using the surface from sketch option, the surface is generated, and

two bodies are identified (soil, and atmosphere) with the pipe being hollow circle not part of the soil body. With this, the geometry is done, and ready for meshing.

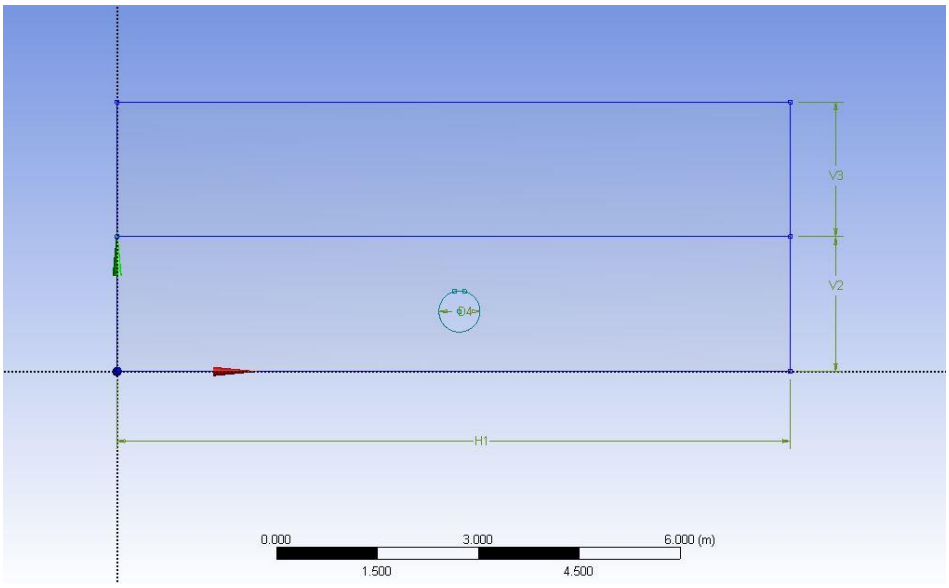

Figure 24 Phase 1 geometry

5.1.2 Phase 2

The only difference between phase 1 and phase 2 is that phase 2 has more dimensions to assure a better accuracy of the geometry after understanding the software better. The sketching steps are exactly as stated in the previous section up until the dimensions part. In this geometry, four more dimensions are added in order to ensure that the location of the pipeline, and the hole size are exact and not approximated. A vertical dimension between the bottom of the geometry and the center of the circle is added to ensure the center is 0.8 m above the bottom line, which is represented by V6. A horizontal dimension between the left side of the geometry and the center of the circle is added to ensure the

center is 5 m away from it, being exactly at the middle, which is represented by H5. To control the hole size, two horizontal dimensions were added from each point of the split inlet to the side of the circle. By ensuring that both of them are equally distanced from the side, the hole size would be in the center, and would be the length left from the circle diameter after subtracting the dimensions. In the case, the dimensions were both 0.255 m in order to have the hole size at exactly 0.1 m. The dimensions are represented by H7 and H8. Other dimensions (H1, V2, V3, D4), are exactly as mentioned in phase 1. A schematic diagram of the geometry of phase 2 is shown in Figure 25. The modeling steps to create the surface body are exactly as mentioned in phase 1.

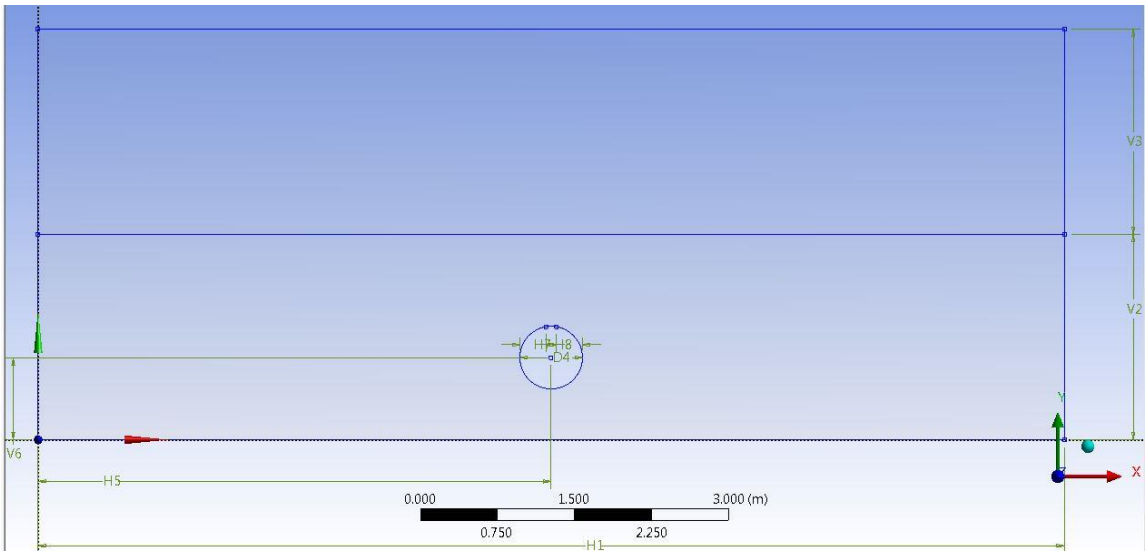

Figure 25 Phase 2 geometry

5.1.3 Phase 3

The geometry in this phase is used to validate the model using the experimental work done by Yan et al. [25]. In this case, all the steps were identical to the previous phase with the only difference being the values of the dimensions, in order to represent the information given in the paper. The pipe diameter D4 is 0.2 m, the distance from the bottom to the center of the pipeline V6 is 1.1 m (pipe depth 0.9 m), and the hole size is 5 mm (H7, and H8 are 0.0975 m). Other dimensions (H1, V2, V3, H5), are exactly as mentioned in phase 2. A schematic diagram of the geometry of phase 3 is shown in Figure 26. The modeling steps to create the surface body are exactly as mentioned in the previous phases.

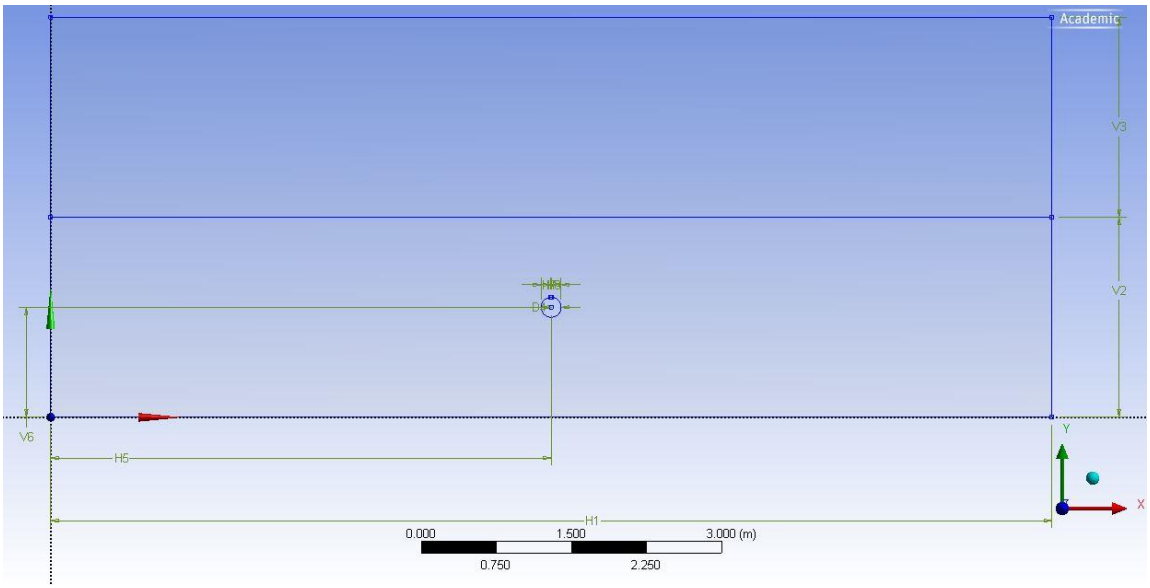

Figure 26 Phase 3 geometry

5.2 Meshing

The next step after creating the geometry is to divide our domain to cells generating a grid. The meshing process is done by using ANSYS Meshing. The system is divided into nodes, and the CFD codes will run at each of these nodes. The size of the nodes and the number of the nodes affects the accuracy of the solution, and the computational time it takes to get results. Thus, choosing the optimal mesh size would generate good accuracy with the lowest possible computational time. The size of the mesh is not usually uniform throughout the geometry. It is usually finer around the point of release and interfaces, and coarser around other locations when the flow is already established.

In order to do meshing, the first step is to import the geometry into ANSYS meshing, which is done automatically when using ANSYS Workbench. First, in order to make the process organized, different sections of the geometry are named. The named sections were:

- Inlet, which is the opening on top of the pipeline;
- Pipe wall, which is the rest of the pipeline other than the opening;
- Imaginary wall, which is the bottom of the geometry;
- Outlet, which is the top of the geometry;
- Soil, which is the lower half of the geometry;
- Atmosphere, which is the upper half of the geometry;
- Interface, which is the line separating the soil body and the atmosphere body;
- Symmetry, which are the lines on the sides of the geometry.

Many different mesh sizes were investigated in the project, which is discussed in the next chapter. Figure 27 shows the different approaches that were adopted. In order to make Mesh (A), the sizing option is selected, then it was applied four times on different locations as follows:

- For the inlet, element size selected was $6x10^{-3}$ m;
- For the pipe wall, element size selected was $2x10^{-2}$ m;

- For the interface, element size selected was $2x10^{-2}$ m;
- For the soil and atmosphere bodies, element size selected was $5x10^{-2}$ m.

The element size is different in different regions in hopes of having higher accuracy in areas where the flow is establishing, where the possibility of error would be higher if the element size is big, since the whole node would be considered one point for the calculations. The next step is generating the mesh, and the mesh would be created. For Mesh (A), the size obtained is 21,452 nodes. Another option was used for the example of Mesh (C). In order to get the sphere-like mesh, a new point is created which is intended to be the center of the sphere. The coordinates of the points where (5,2.5). Then, going back to mesh sizing option, the soil and atmosphere bodies are selected. Then, the "Sphere of Influence" mesh sizing type is selected. The previously defined point was set as the center. The options also requires inputting the radius, and the element size, which were 2.5 m and $2x10^{-2}$ m respectively.

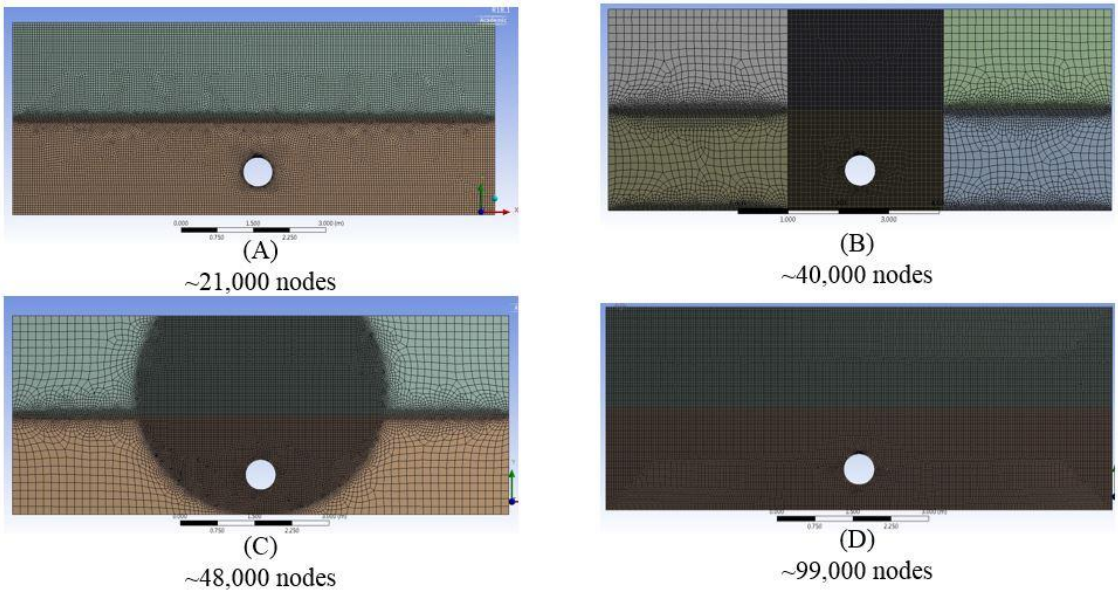

Figure 27 Different mesh sizes for the same geometry

5.3 Model Setup

After the meshing process, the meshed geometry is inserted into ANSYS Fluent. The final step before running the calculations, is to decide which models are required for the solution, and to provide the necessary input data to solve the equations.

5.3.1 General Setup

Some of the general settings for running the simulation involved having the solver type as pressure-based, and the velocity formulation being absolute. The 2D space is set as planar, and the time is set as transient, which reflects the case we have in our hands. Finally, the gravity value is selected to be -9.81 m/s^2 in the y direction.

5.3.2 Models

In the models section, various models that are enabled in order to be used for the simulation calculations. The ones that are of concern to this project are the multi-phase model, energy model, viscous model, species model, and population balance model.

In the multi-phase option, the number of phases and the model type is selected. In this project, the number of phases differed based on the time of the simulation ranging from one phase to three phases depending on the wanted simulation. After the number of phases is selected, the Eulerian type is selected based on the literature review. The CFD-DEM option is not chosen due to the massive domain of the case, which would not make it feasible to be done in a reasonable manner, due to the huge number of particles and the massive time it would require to solve equations for each of them. Afterwards, the phases are selected in order to input additional information to each phase. The three phases are air, soil, and methane. For air and methane, no changes are added since they are gas phases. For soil, the granular option is enabled, since it is a solid phase. For the soil properties, the diameter was set as a constant diameter of 1 mm. For the granular viscosity, the Gidaspow[53] model was selected, since it showed better agreement with experimental data compared to Symlal-Obrien[54]. [55] In addition, for the granular bulk viscosity, the Lun et al.[56] model was chosen, being the only available model in Fluent. Finally, the

packing limit was left as default as 0.63, which the value for the assumption that the soil particles are spherical, but was changed in many simulations depending on the case.

The energy model enables the user to enable the energy equation. This option was enabled or disabled depending on the simulation. It is a requirement to be used in the case of a density that is not constant.

The viscous model is used to choose type of the flow (Laminar or turbulent), and to choose the turbulence model needed for the simulation. The model chosen is the k-ε model, since it is the most widely used model, and the case of this project does not fall into its weaknesses.[45]

The species model is used when there is a material that is used in the simulation, but the amount is too small for it to be considered a phase. The details of this model are shown in Chapter 7.

The population balance model is used in order to have a particle size distribution of the soil particles and not a fixed diameter. The method used is the discrete method, since particle range is known, and the span of the particle sizes is 2-3 orders of magnitude from each other. The use of this model is shown in Chapter 6.

5.3.3 Materials Setup

All the materials included in the simulation cases need to be added including all fluids and solid. Both air and methane are available in the Fluent database with their respective data. For the soil, a user defined material is added as a fluid since this is an Eulerian-Eulerian approach, and the soil density is required as input. The soil is assumed to be sand and density chosen for this project is 1600 kg/m^3. [57] In the case of the energy balance equation being enabled, the user must specify the model for calculating density since it is no longer constant for the fluids. Various models are available including ideal gas and Peng-Robinson.

5.3.4 Boundary Conditions Setup

The types of boundary conditions in the domain, and any other required information for specific boundaries must be added in order for the equations to be solved. The type of boundary conditions is stated below for the named selections from the meshing section.

- For the inlet, velocity, pressure, and mass flow inlet types were chosen for different stages of the project and with various values;
- For the pipe wall and the imaginary walls, the type of boundary is “wall”;
- For the outlet, the boundary type selected is a pressure outlet, and is set to 0 barg in all stages of the project, since the outlet is in the atmosphere;
- For the interface, the boundary type “interface” was chosen;
- For symmetry, “symmetry” boundary type was selected.

5.3.5 Initial Conditions Setup

Since that the simulations that are run are transient, initial conditions must also be added to solve the equations. After initializing the simulation, various parameters are patched based on the case simulated, such as the sand volume fraction in the soil body (which differed based on the phase of the project) and in the atmosphere body (which is zero). The same procedure is done for air and methane volume fraction values in the soil and atmosphere body, with methane being always zero at the start of the simulation, and air being the rest of the volume fraction. This can be done through code that is used for Fluent. An example of code used for simulations is shown in the Appendix.

5.3.6 Running Calculations

The final step before running the calculations is to choose the time step size, the number of time steps, the time step method, and the max iterations per time step. There are two time step methods, either a fixed time step or an adaptive time step. The adaptive time step allows setting a range of time step sizes and the software chooses the time step size based on the residuals. The lower the residuals are the higher the time step size the software uses bounded by the user’s input. In addition, the ending time is chosen to decide when the

simulation ends. The fixed time step method has only one time step size and it runs based on the number of time steps inputted. Throughout the project, the time step size ranged from as low as $1x10^{-5}$s to as high as 1 s. In general, having a smaller time step size increases the accuracy, but increases the computational time significantly. Thus, it is important to try to find the optimum time step size with good accuracy. The maximum iterations per time were chosen to be 100 throughout the project. After all the previous information is set, running calculations can start and the software starts generating and recording data. In order to speed up the calculation time, the Fluent case file is sent to the Supercomputer "Raad", available at Texas A&M University at Qatar, and multiple simulations are run simultaneously. The job file used for the supercomputer is shown in the Appendix.

5.3.7 Results Example

Figure 28 shows the results of a simulation that has been done using the model set-up using ANSYS Fluent. The results are shown from the beginning of the simulation to 5 seconds flow time from the start of release. In this case, the following conditions were used:

- Pipeline depth: 1.2 m
- Pipeline diameter: 0.61 m
- Methane velocity: 10 m/s
- Soil type: sand
- Orifice size: 0.1 m
- Soil volume fraction: 0.63

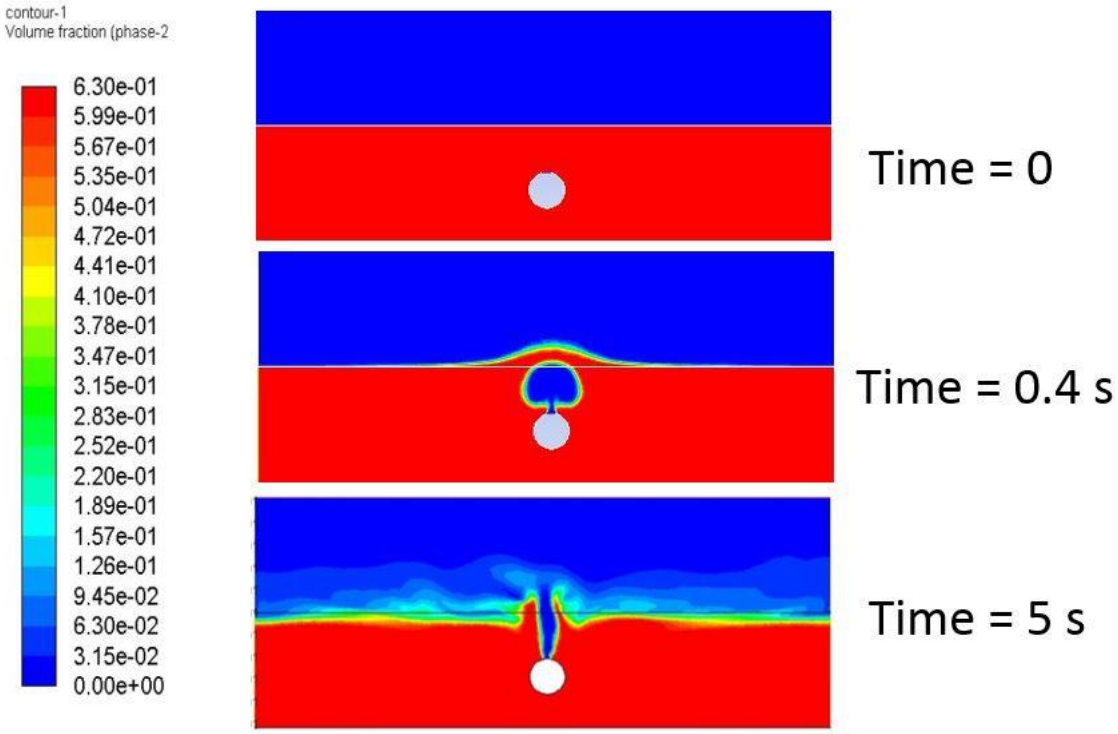

Figure 28 Sand volume fraction at the start and after some time

Various changes were done to the set-up throughout the project, which are shown in Chapter 6.

6 MODEL CONFIGURATION

In order to ensure the performance of the model, to use it for validation and boundary identification later on, various parameters were changed and investigated throughout the project, and due to the results of the investigated parameters, various configuration changes were done. The parameters that were investigated are as follows:

- Mesh size;
- Soil viscosity in the material tab;
- Soil particle diameter;
- Type of inlet boundary condition;
- Primary phase selection;
- Inlet velocity;
- Type of geometry boundary condition;
- Specific gravity;
- Presence of soil;
- Material density.

6.1 Mesh Size

As seen in Figure 27, various mesh sizes were used during the lifetime project, in order to obtain the best possible outcome. Mesh (B), and Mesh (C), are both approaches where a finer mesh is present in the middle area, which is the area where the gas flow would be. In Mesh (B), a change in the geometry was added and instead of having two boxes representing the atmosphere, and soil bodies, six boxes were used, three for the atmosphere boy and three for the soil body. The middle boxes were then set at a smaller mesh sizing compared to the others boxes since it's the area where the flow would be. The issue with this approach was a technical issue, since that Fluent did not allow for the vertical lines to be assumed as interfaces, and hence the simulations could not be run. In order to overcome the technical issue, another approach was using the sphere of influence option, which is represented by Mesh (C). The details on how to make Mesh (C) are shown in section 5.2. The technical issue from Fluent was no longer present, however, all the

simulations that were run using Mesh (C) diverged, and the mesh size was not used for simulations. In order to make sure that the results obtained were independent of the mesh size, and that the simulations gave acceptable results, a mesh independence study was conducted. The study was done using element sizes of 8, 5, and 2 cm in the areas that were not at the inlet or the interface. The meshed geometry of each element size is shown in Figure 29. For the mesh independence study, the residual error value of 10^{-4} was considered acceptable, [58] and it was checked for the continuity equation and for a parameter of interest, which is the methane volume fraction. The residual error is the difference of error magnitude of an equation between iterations. In general, decreasing the element size increased the simulation time required to reach the solution. Table 6 shows the results obtained for the mesh independence study and from the table, Mesh (A) gave an acceptable error with a reasonable running time for a single simulation. Thus, Mesh (A) was selected to be used for the rest of the project.

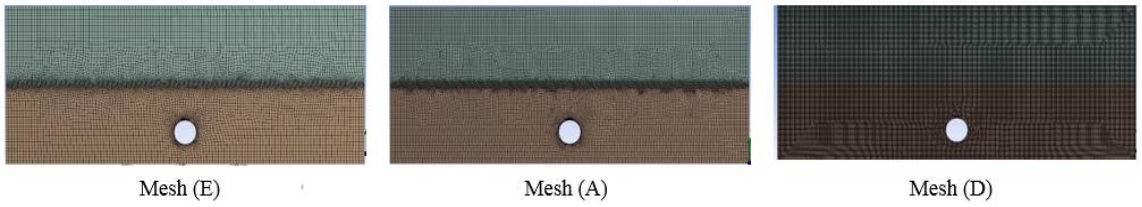

Figure 29 Different mesh used for mesh independence study

Table 6 Mesh independence study results

Mesh	Element size (cm)	Number of nodes	Continuity residuals	Methane volume fraction residuals	Simulation time to reach 5 s
Mesh (E)	8	~12,000	$\sim 10^{-3}$	$\sim 10^{-8}$	~6 hrs
Mesh (A)	5	~21,000	$\sim 10^{-4}$	$\sim 10^{-9}$	~8 hrs
Mesh (D)	2	~99,000	$\sim 10^{-4}$	$\sim 10^{-9}$	~36 hrs

6.2 Soil Viscosity in the Material Tab

In the Material tab in Fluent, once a material is selected, there is a slot for viscosity, in case the material selected is a fluid. In the Two-Fluid approach, our soil is considered a fluid, and hence a value of viscosity needs to be inputted. In this case, the soil material is sand, and there is not value for viscosity for it since it is a solid. However, there is the granular bulk viscosity that is setup in the phases tab, which is obtained by the drag model mentioned earlier in 5.3.2. Two different viscosities were used to test if the value affects the solution or not which were $1x10^{-2}$ Pa.s and $1x10^{-3}$ Pa.s respectively. Figure 30 shows the results at the same time step for both viscosities, and the results show that the solutions are identical. Hence, the viscosity in the material tab is not taken into account, and the granular bulk viscosity is the one used for calculations by the software.

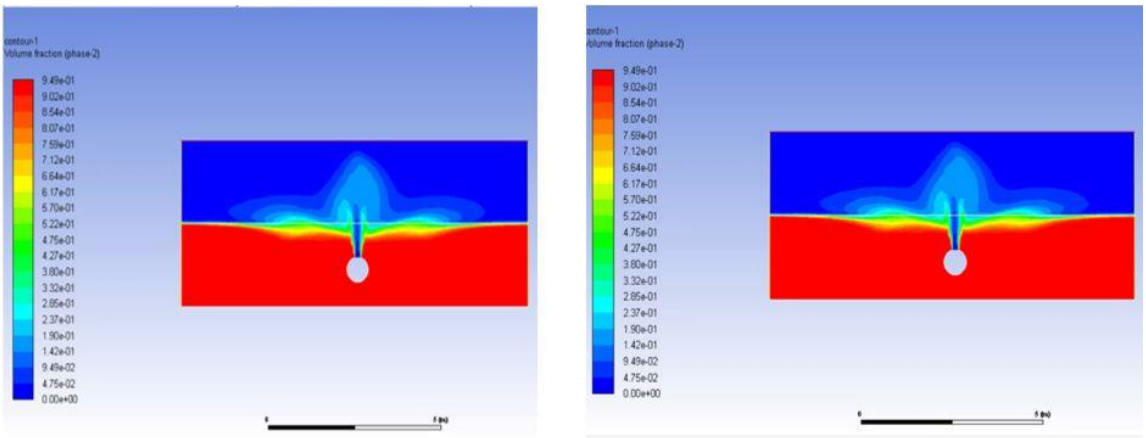

Figure 30 Sand material tab viscosity comparison

6.3 Soil Particle Diameter

As specified in Chapter 5, the sand particle diameter has to be specified in the phases tab. However, the only available options are a constant diameter or a user defined function, where the user can write their own code. In order to have a varying sand particle diameter, and to observe its effect on the simulation results, the population balance model is used. The population balance model is not available in Fluent by defaults and it has to be activated. After the model is activated, various options are available. The one chosen for this simulation is the discrete model, since it allows having multiple bins, and it is used when the particle size range is known, with the span of the particle size range being 2-3 orders or magnitude. According to the United States Department of Agriculture, the sand size ranges from 0.05-2 mm[59]. The number of bins (divisions between the minimum and maximum values) is chosen to be four. The phase chosen is phase-2 which is the sand phase. The minimum particle size value is inputted, then the ratio exponent is set to be 5.33 in order to obtain the maximum particle size value. Using the population balance model also requires adding additional initial conditions, which are setting the values for

each bin in the soil particle size distribution. The size of bins is assumed to be identical with 25% for each quarter. Figure 31 shows the results obtained for sand volume fraction for an inlet flow of 10 m/s at 5 seconds. It seems that the effect of the flow is clearer on the soil surface in the case of a varying diameter, due to the presence of many smaller particles. The sand cloud in the atmosphere also appear to be denser, but not significantly. The use of the population balance model also increases the residuals, which is expected due the introduction of an additional equation to solve. The population balance model was not used in the rest of the project due to the associated error, and due to the interest of other parameters for the simulations. The change of the code used for Fluent is shown in the Appendix.

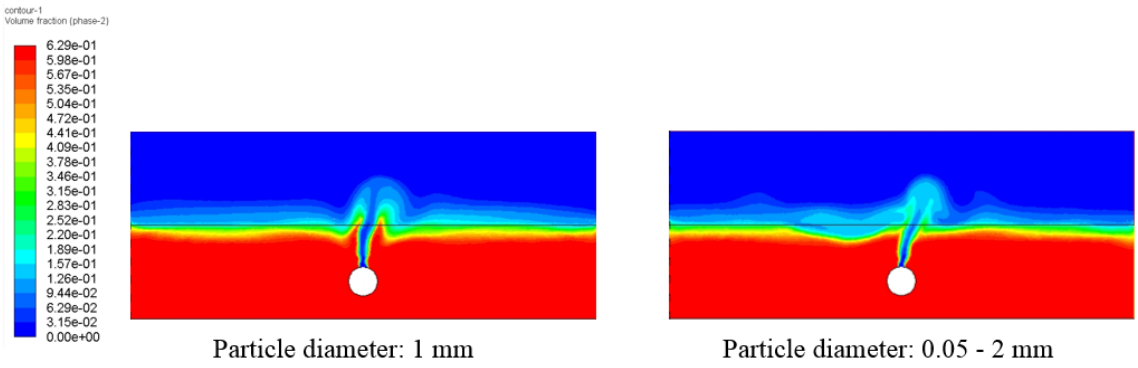

Figure 31 Sand volume fraction at 5 s for different particle diameter

6.4 Type of Inlet Boundary Condition

The two main inlet boundary conditions that were studies are pressure inlet and velocity inlet. Using a pressure inlet is probably more useful for the industry since that the pipeline pressure is known, compared to the velocity inlet which is not necessarily known. However, using the pressure inlet boundary condition has shown multiple issues during

simulations, and most of them diverged, either immediately or after some short time less than 5 seconds. Table 7 shows some of the pressure values that were investigated and whether they diverged or not. Figure 32 shows the results obtained from a diverged simulation for sand volume fraction. On the other hand, using a velocity inlet showed a much better stability for the solutions, through a wide range of velocity values, from 0.1 m/s to 50 m/s, and all the simulations converged and gave results. As a result of that, the velocity inlet was chosen to be used throughout this project.

Table 7 Pressure inlet simulation cases and their results

Case #	Inlet pressure (kPa)	Result
1	8	Diverged immediately
2	10	Diverged after 0.5 s
3	15	Diverged after 1.6 s
4	25	Diverged after 2.3 s
5	50	Converged to 5 s
6	100	Converged to 5 s
7	2000	Diverged after 1.2 s

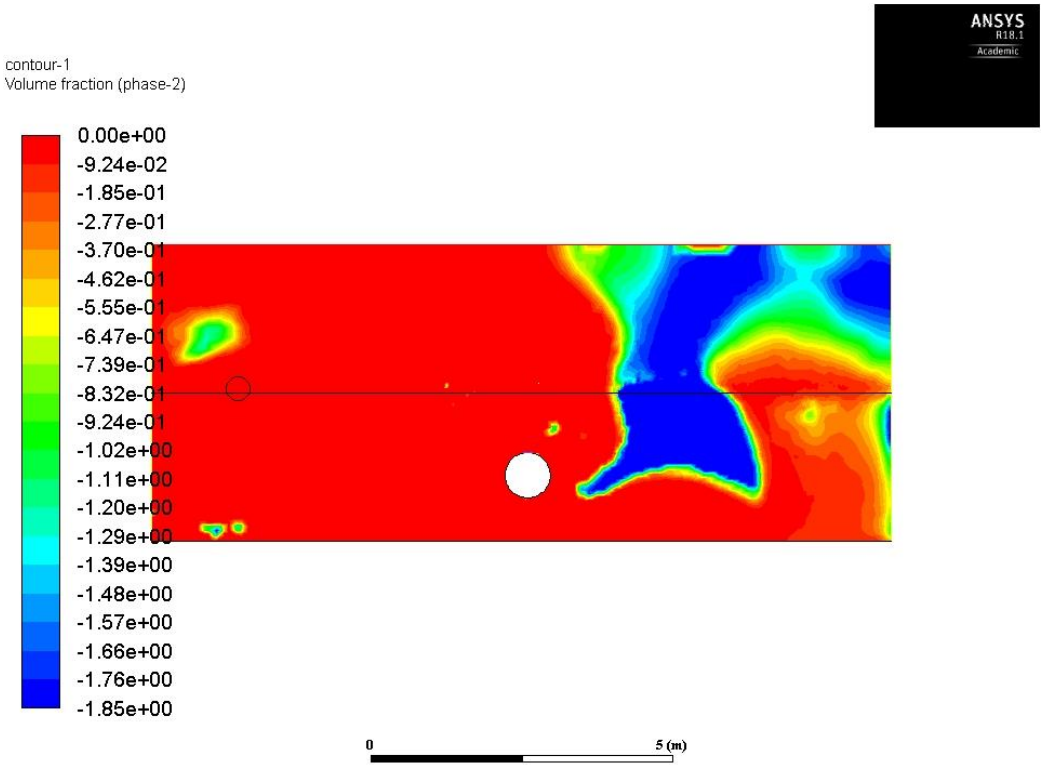

Figure 32 Example of a diverged simulation for sand volume fraction

6.5 Primary Phase Selection

The presence of three phases, including air, sand, and methane, grants a decision to choose which phase is the primary phase and which other phase is secondary. Since the sand is a solid and is not part of the flow, it is selected as a secondary phase. The choice between air and methane seems to be dependent on the phase that is dominant in the inlet stream. For example, Figure 33 and Figure 34 show the results obtained from a 10 m/s methane inlet with air as the primary phase. The results clearly seem incorrect despite the fact that the simulation converged. On the other hand, Figure 35 and Figure 36 show the results obtained for the same velocity inlet, and the results seem to be reasonable, and the pressure data seem to be correct, based on the soil density, and volume fraction. Similarly, in other

simulations where air was the inlet with traces of methane, the simulation diverged when methane was chosen as the primary phase, and gave reasonable results with air being chosen as the primary phase. So, it is apparently necessary to choose the dominant material in the inlet as the primary phase for this kind of simulations.

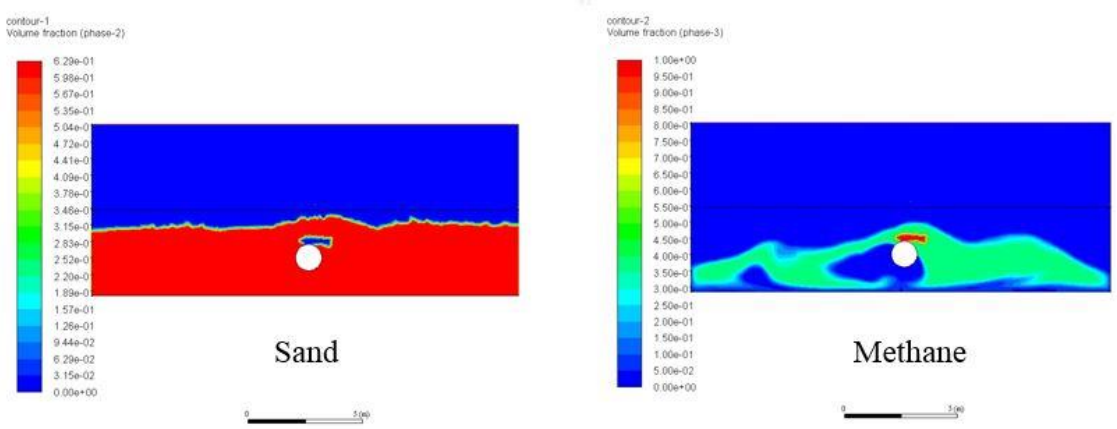

Figure 33 Sand and methane volume fraction with air as primary phase

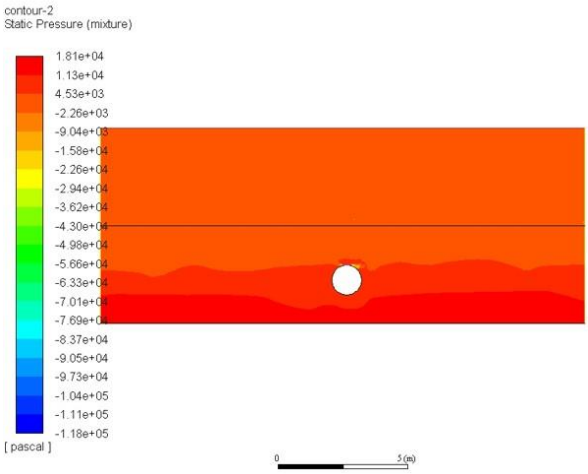

Figure 34 Pressure data with air as primary phase

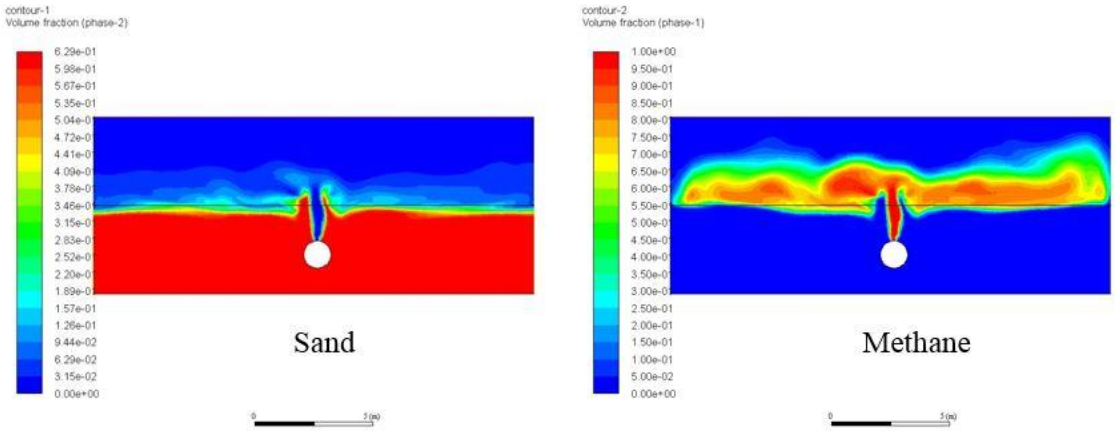

Figure 35 Sand and methane volume fraction with methane as primary phase

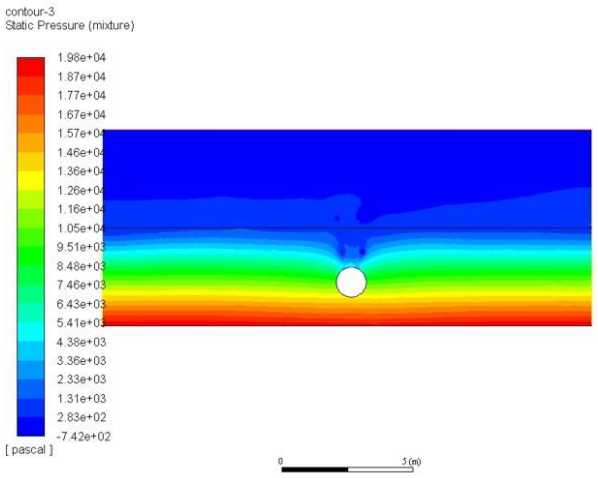

Figure 36 Pressure data with methane as primary phase

6.6 Inlet Velocity

Since the velocity-inlet was chosen to be used as the boundary condition, different velocities were used to check for the ability of the model to show different results. Four different velocity values were checked being, $2x10^{-2}$m/s, 5 m/s, 10 m/s, and 15 m/s. Figure 37 shows the results obtained for methane volume fraction at around the 5 seconds mark. The results that appear are expected since that with a higher inlet velocity, more methane can be seen in the atmosphere, and hence the model was able to predict such behavior. However, it was concerning that the methane does not reach to the top of the boundary, which is only 2 m high. One longer simulation was run in order to check if the methane reaches the outlet eventually. Figure 38 shows the methane volume fraction at different times with an inlet velocity of 10 m/s. From the figure, it is clear that the methane does reach the top eventually, but it would be expected for it to reach sooner. Also, it can be seen from the figure that the side of the geometry, that the methane is trapped on the side of the atmosphere and not able to escape because of the symmetry boundary condition.

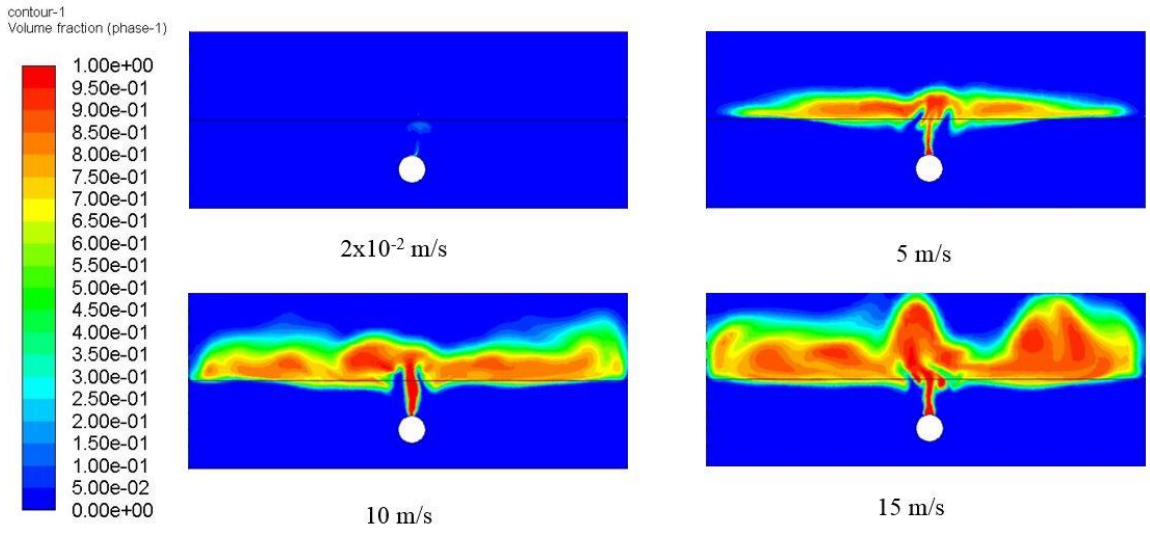

Figure 37 Methane volume fraction for different inlet velocity at 5 s

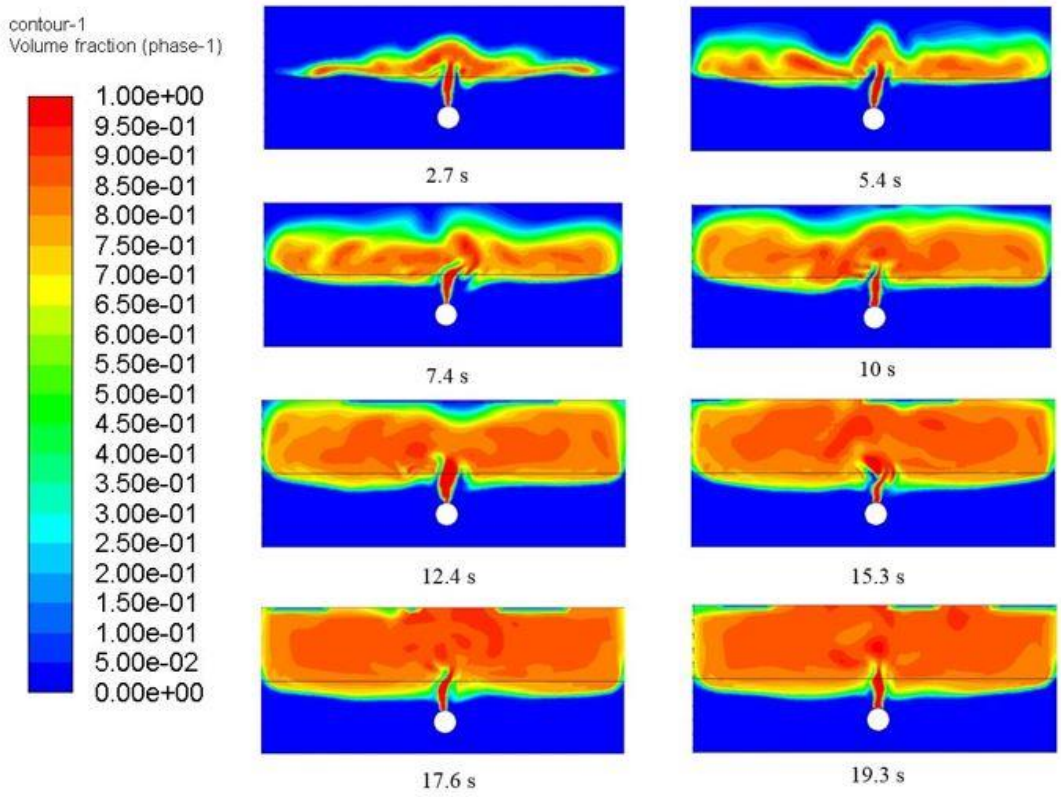

Figure 38 Methane volume fraction at different time steps with a 10 m/s inlet

6.7 Type of Geometry Boundary Condition

Due to the gas being trapped by the side due to the symmetry boundary condition, which means that both sides are mirror images of each other. Instead, the sides on the atmosphere body were changed to the pressure-outlet boundary condition, while the sides in the soil body were kept as symmetry. Figure 39 shows the results obtained from each case, and shows that the gas is able to escape from the sides by using the pressure-outlet boundary condition. Thus, the pressure-outlet boundary condition is used for the rest of the project.

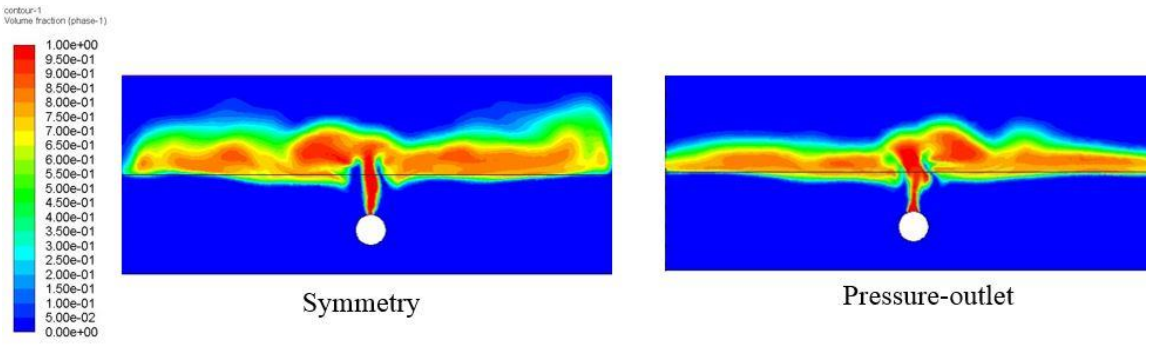

Figure 39 Methane volume fraction for different boundary conditions at 5 s

6.8 Specific Gravity

In order to find out the reason of the lag of methane from reaching the top, different materials lighter and heavier than methane were used. The materials used were ethane and propane, which are both heavier than methane, and hydrogen, which has a lower specific gravity than methane. Figure 40 shows the gas volume fraction for each gas at 5 seconds with a 10 m/s inlet velocity. The results visually did not answer the question of the lag cause, and all the gases did not reach the top.

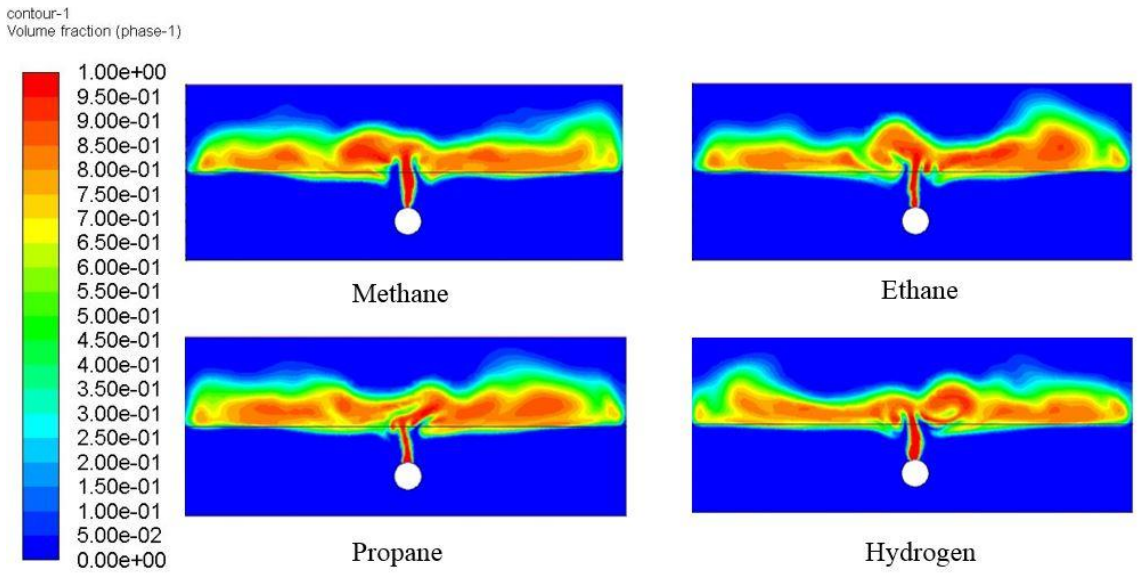

Figure 40 Volume fraction for different gases at 5 s

6.9 Presence of Soil

Another approach to discover the reason behind the methane lag to the top was having the same simulation, but without the presence of soil, to see if the gas will reach to the top faster. This was done by removing the soil phase and having only the methane and air phases left. Figure 41 shows the flow of methane at 10 m/s, and in the case of no soil, the gas does reach to the top quickly. This leads to the conclusion that the sand cloud that is formed affects the gas dispersion in the atmosphere, and diverts the gas to go more horizontally than vertically, however, the gas does reach the top eventually. The fact the soil cloud might affect the gas dispersion in the atmosphere might be significant to safety, because, when the gas is flowing with no soil, the methane concentration is above its Higher Explosive Limit (HEL). Thus, it would be considered a safe area near the release since methane will not ignite. However, the results of the simulation show that some of the methane is between its Lower Explosive Limit (LEL) (5%) and its HEL (15%),[60]

which means that the possibility of methane igniting is present, and such safety concerns must not be overlooked.

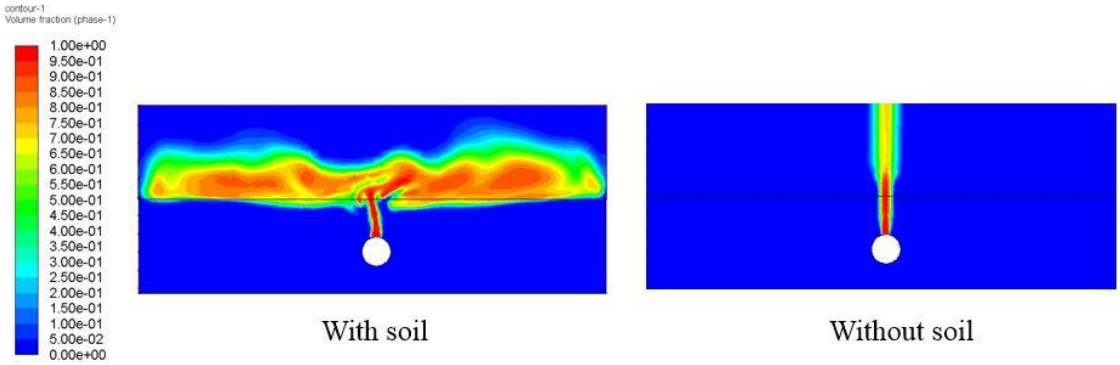

Figure 41 Methane volume fraction dependent on the presence of soil

6.10 Material Density

Finally, the methane and air density values were considered constant, and the possibility of using an equation of state to obtain them was checked. To do so, first the energy equation is enabled. Then, for each material the equation of state in the materials tab is chosen. Both ideal gas, and Peng-Robinson equations were tested. The initial temperature has to also be specified in the boundary conditions. Figure 42 shows the results obtained for assuming ideal gas behavior compared to a constant methane density. The results are not massively different, but it shows the model's ability of simulating using non-constant density. However, using non-constant density increases the residuals, which is expected since more equations come into place.

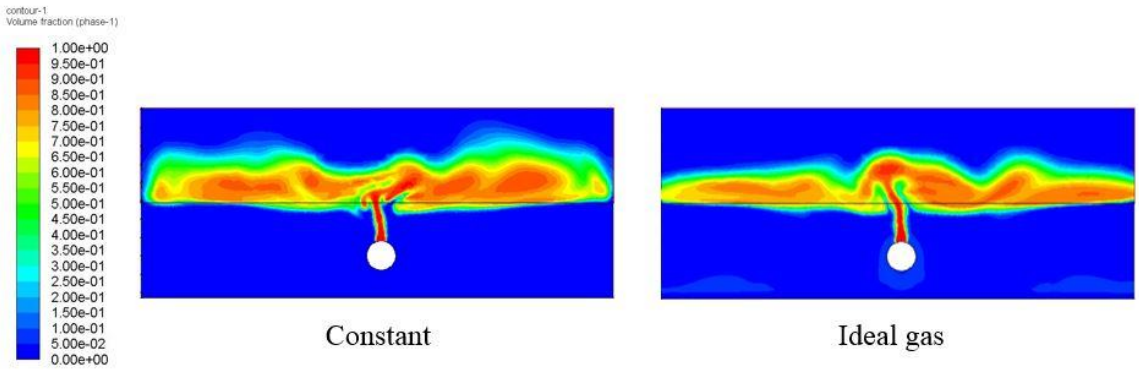

Figure 42 Methane volume fraction for different density approaches at 5 s

7 MODEL VALIDATION

In order to check the performance of the model, it has to be validated against experimental data. The experimental data that is chosen for validation for this project is the one shown in Figure 43 provided by Yan et al. [25] for a flow of 24 L/min. It is the only available experimental data on the same scale of geometry with the data points available, and also the most recent work that has been found. Figure 44 shows a schematic representation of the locations of the sensors.

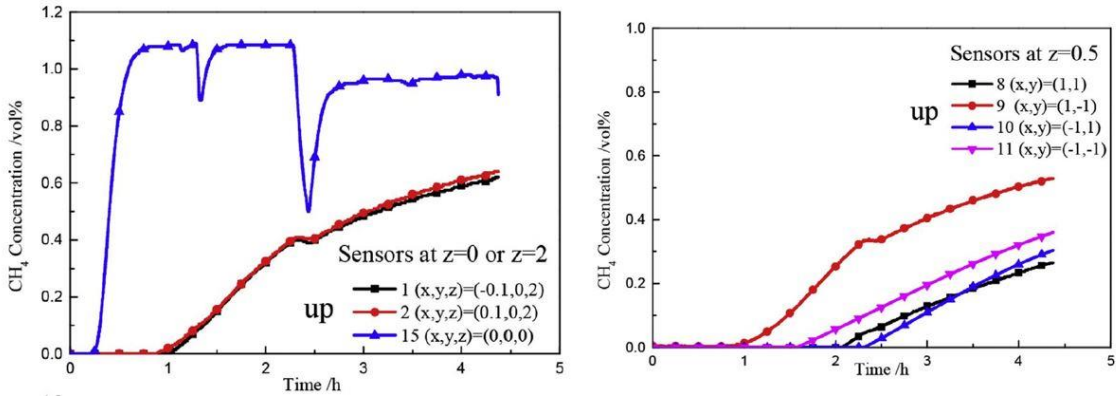

Figure 43 Yan et al. experimental data for 24 L/min flow Reprinted from [25]

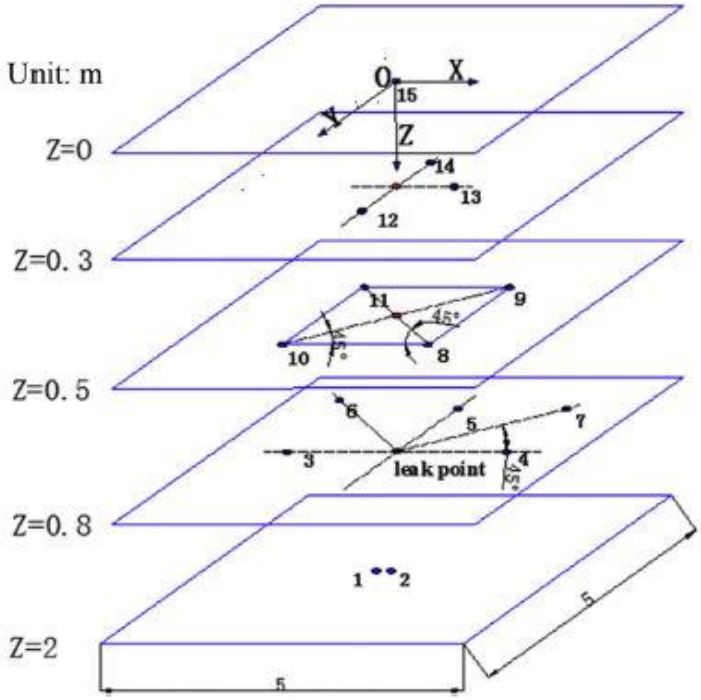

Fig. 2. Coordinate system and sensor locations.

Figure 44 Sensors locations schematic diagram Reprinted from [25]

7.1 Setup Adjustment

Some adjustments are required to the setup, to match the conditions of the experimental work. First, the geometry is adjusted to match the geometry described by Yan et al.[25], shown in Figure 16. The adjusted geometry has already been mentioned in Section 5.1.3 and shown in Figure 26. Afterwards, the meshing process has to be done. The original mesh does not work because the mesh size at the inlet was bigger than the orifice size provided by Yan et al., which is 5 mm. The inlet edge sizing is selected to be $1x10^{-4}$ m, and the resulting mesh had 21780 nodes. The inlet in the experimental work was 97.5% vol% air, and 2.5% vol% methane. The issue with this flow with the current model, is the fact that the methane amount is too small to represent its own phase. In addition, using

methane as the primary phase causes divergence, and air was switched to be the primary phase since it is the dominant phase in the inlet. Some adjustments that are made in the setup include setting the porosity to 0.13 in the soil body. The value of porosity is the average porosity taken from the experimental data. Similarly, the soil density was taken from the average of the experimental data and changed in the materials tab to 1380 kg/m^3. The soil permeability was kept as default, and the soil particle size was left as 1 mm, since that the data is not provided and the type of soil is not mentioned in the experimental work. Simulations were attempted with having three phases, but most of them diverged, and the rest gave unreasonable results. This is probably due to the small amount of methane, and hence, the "Species" model was activated. First, a mixture has to be defined in the materials section, from the available materials that have already been defined. The mixture defined is a mixture of methane and air. The mixture is then selected in the species model. The third phase is removed and the mixture is considered as the primary phase, while the soil remain as the secondary phase. After setting up the model, the simulations then can be started. However, another issue with the validation is the duration of the experiment which is in hours. With the current model, reaching 5 seconds using a time step of 1 ms takes around 8 hours of computing in the super computer. So, it would take months to reach the same time frame as the experimental data by using the same time step size. By raising the time step to 1 s the simulation time is much shorter, to around three days, but the residual error becomes much larger. In an attempt to simulate the case using a 1 s time step the simulations diverge almost immediately. In order to overcome this error, the simulation was first run with a small time step (1 ms) for the first 10 seconds, then the final data file at the 10 s mark was used as the initial condition, for the case where the time step is 1 s. The simulation was run to a solution time of 10,710 s, with the data recorded every 100 seconds. The journal file used for Fluent is shown in the Appendix.

7.2 Results and Discussion

The locations with the coordinates from Table 2 and shown in Figure 43 were located in the geometry using the point option in the CFD-Post 18.1 software, which is used for post processing. Locations 1, 2, and 15 are on the same plane as the geometry (since y=0) and

the coordinates for the points were as follows: Location 1 (4.9,0), Location 2 (5.1,0), and Location 15 (5,2). For Locations 8,9,10, and 11, since these locations do not fall on the 2D geometry plane (y≠0), the values were obtained by setting $x = r = \sqrt{x_{exp}^2 + y_{exp}^2}$, and by this Locations 9 and 11 are omitted since they give identical locations to 8 and 10. The coordinates for Location 8 are (7,1.5) and for Location 10 (3,1.5). The results of the simulations are shown in Figure 45 for Location 1 and 2, Figure 46 for Location 8 and 10, and Figure 47 for Location 15. The experimental points were obtained from Figure 43 Yan et al. experimental data for 24 L/min flow with the help of "Web Plot Digitizer" software.

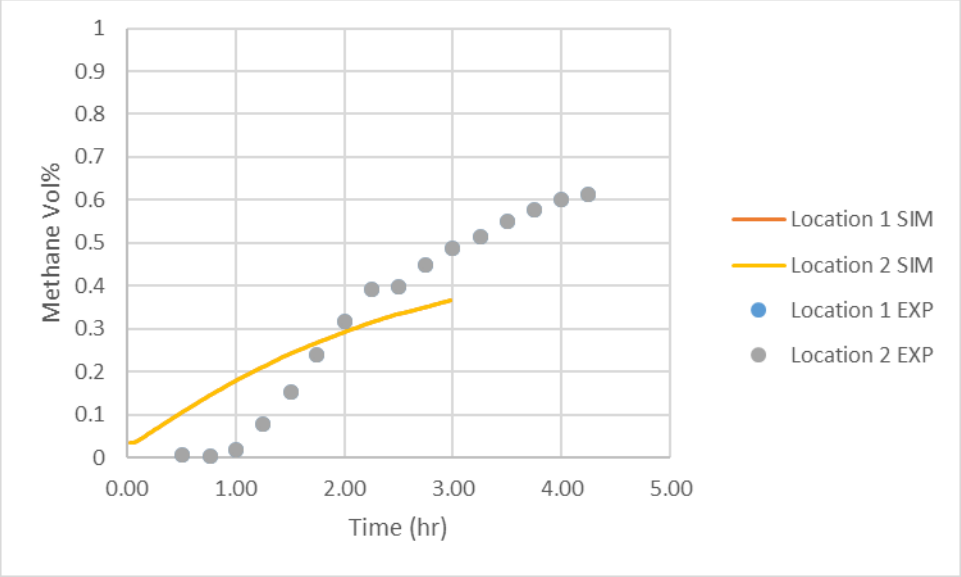

Figure 45 Validation results for Location 1 and Location 2

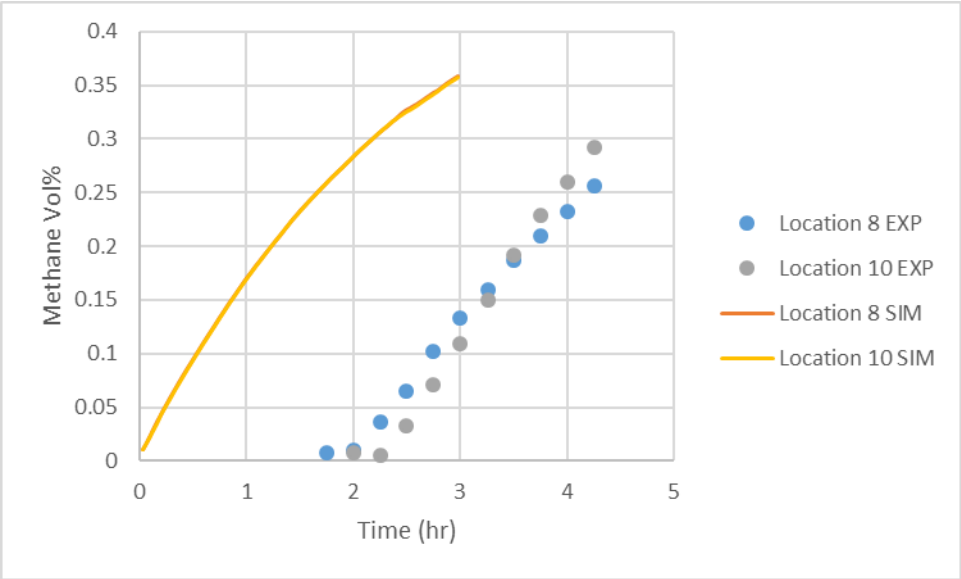

Figure 46 Validation results for Location 8 and Location 10

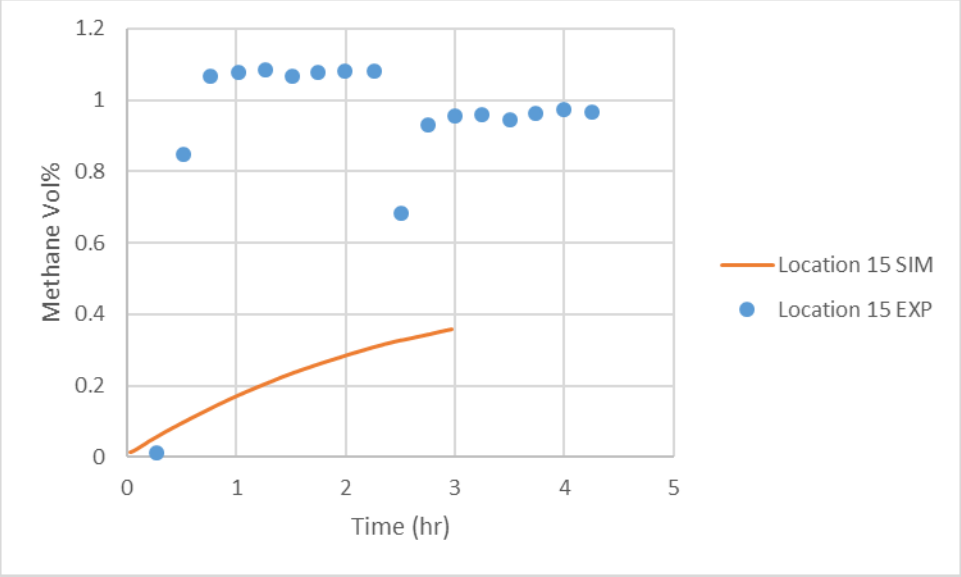

Figure 47 Validation results for Location 15

The normalized mean square error (NMSE) can be obtained using:

$$NMSE = \frac{1}{N}\sum_{i}\frac{(Predicted - Experimental)^2}{\overline{Predicted} * \overline{Experimental}} \quad (82)$$

The relative error can be obtained using:

$$Relative\ Error\ \% = \frac{|Experimental - Predicted|}{Experimental} x100 \quad (83)$$

Figure 45 shows the results obtained for Location 1, and Location 2, compared with experimental data. The simulation results for both locations lie on top of each other, since that the locations are mirror images of each other. Hence, the results should be identical since the system is symmetrical. In the experimental data there is a clear lag of when the concentration starts increasing, while the model is unable to predict such lag. The NMSE value obtained is $1.8x10^{-1}$. The lower the NMSE value the more the model is considered well performing both in space and time[61]. The average relative error value is really high due to the first three points which represent the lagging. If the first three points are omitted the average relative error is 4.6%. There are many factors that contribute towards the error including the high residuals due to the use of a large time step (1 s), and the assumptions that were used in the model and soil properties that have been mentioned. The reason of the inability to predict the lagging might be due to the fact that the experimental work has no known bottom, since the gas can go as low as the soil permeates. On the other hand, the wall at the bottom of the geometry limits the gas diffusion, and allows it is concentration to rise much sooner.

Figure 46 shows the results obtained for Location 8, and Location 10, compared with experimental data. The simulation results for both locations also lie on top of each other, since that the locations are mirror images of each other. Again, there is a clear lag between the simulation results and the experimental data, similar to the previous case. The NMSE value for Location 8 is 3.5 and the NMSE value for Location 10 is 5.3, which are both higher than the values for Location 1 and Location 2. In addition to the previously

mentioned probable causes of error, the error here might be due to assumption of the x value that is not represented in the model's geometry due to the fact that it is a 2-dimentional geometry. In addition, the model assumes the soil to be uniform in all directions which might not be realistic in the actual soil that the experiment is based on.

Figure 47 shows the results obtained for Location 15 compared with experimental data. The difference here is the most noticeable compared to the other cases. The experimental data give a larger value compared to the predicted simulation results. The NMSE value obtained for Location 15 is 2.53. In addition to the previously mentioned possible error causes, the difference between the experimental data and the simulation results might be due to a sensor error in the experimental work. That is mentioned by Yan et al. [25] stating that the sensor in Location 15 was covered by a small amount of soil, to prevent the effect of air during the experiment (at 2.7 hours mark), which caused some instability in the obtained results. Which also indicates, that before putting the soil into the sensor, the results might have been affected by the air flowing into the sensor.

Overall, the model was able to simulate the diffusion behavior, without being able to predict the lagging observed in the experimental work. In addition, despite the differences in the predicted concentration values, the values were in the same order of magnitude, and if the results were shifted to include the lagging the results would have been much closer. The values of NMSE also show that the model after being normalized, has the same trend with the experimental data. Despite the model shortcomings, it is believed that it can be reasonably used to predict the gas flow regime behavior, and the concentration increase trend. The species model also increases the error observed in the residuals, and it is believed that the model would have a better prediction of data with having methane as the primary phase, with having a methane inlet instead of it being a species. However, more investigation should be done in the future into the model validation, possibly with using generated experimental data, or by allowing the simulation to go on for months with a small time step while checking the results periodically.

In an attempt to validate the model and check if a lag is observed, the soil phase was removed and the soil body was kept as zone with a porosity of 0.13. By doing so, the system is then limited to a single phase and the multiphase model is turned off. Figure 48 shows the results obtained at Location 1. It is clear that there is a slight lag seen here compared to the previous results. However, the concentration values are much smaller than expected by the experimental data. There is a possibility that by using this approach and varying other parameters such as the soil permeability which is not known, that model might show a closer agreement with the experimental data. However, due to the time frame of the project, this can be done in a future phase.

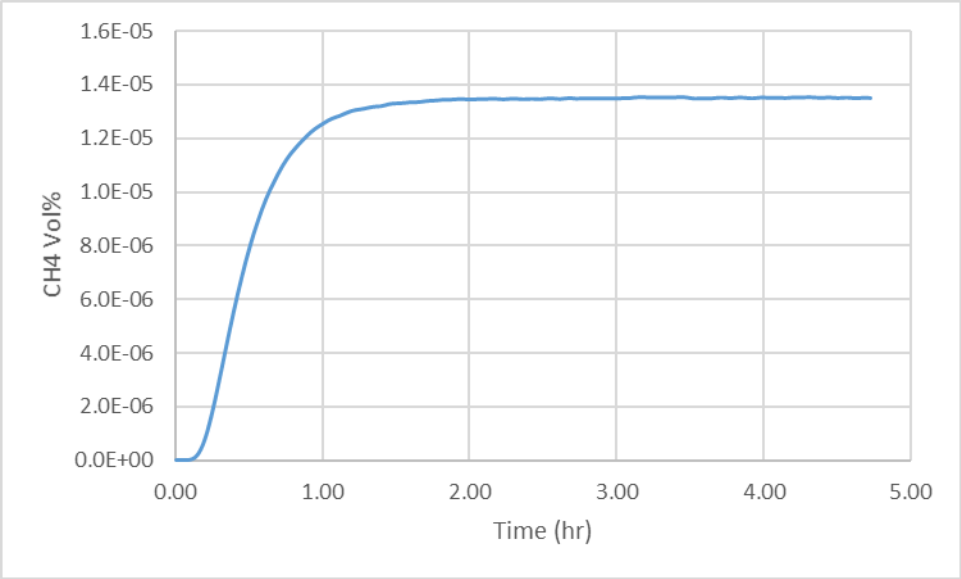

Figure 48 Methane volume percentage for a 1 phase simulation at Location 1

7.3 Crater Width Validation Attempt

It was not possible to validate the crater formation width using the experimental data by Acton et al. directly, due to the previously mentioned issue of using the pressure value as

an inlet, since it diverges. However, by comparing a simulation of an inlet of 10 m/s with their lowest pressure value of pressure (20 bar) for sandy soil and for a pipeline diameter of 0.61 m, using the correlation in Table 4, the crater size obtained was not that different. The crater width obtained using the correlation is 0.38 m. The crater width obtained from Fluent results using the CFD-Post software at a line 0.2 m below the surface (as seen in Figure 49) to avoid its instability was 0.41 m at 4.97 s as shown in Figure 50. Since the crater width is changing with the time steps, the crater width was taken at different time steps. The average crater width obtained for these time steps is around 0.4 m. The reason of the similarity between using the Advantica model and Fluent might be due to the fact that the pressure contribution to crater width is minor for the case of sandy soils as shown in Figure 20, and the crater width were to be extrapolated for lower pressure values it would give similar results.

Table 8 Crater width at different time steps

Time step (s)	Crater width (m)
3.56	0.41
3.76	0.41
4.06	0.40
4.26	0.35
4.56	0.39
4.77	0.46
4.97	0.41

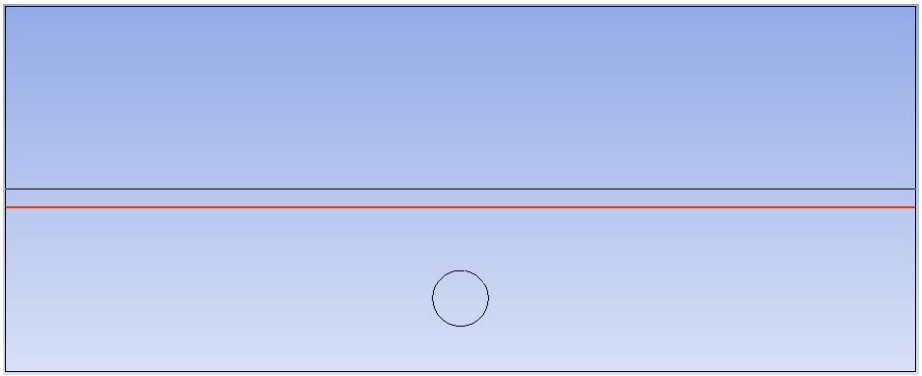

Figure 49 Line location in geometry for methane concentration

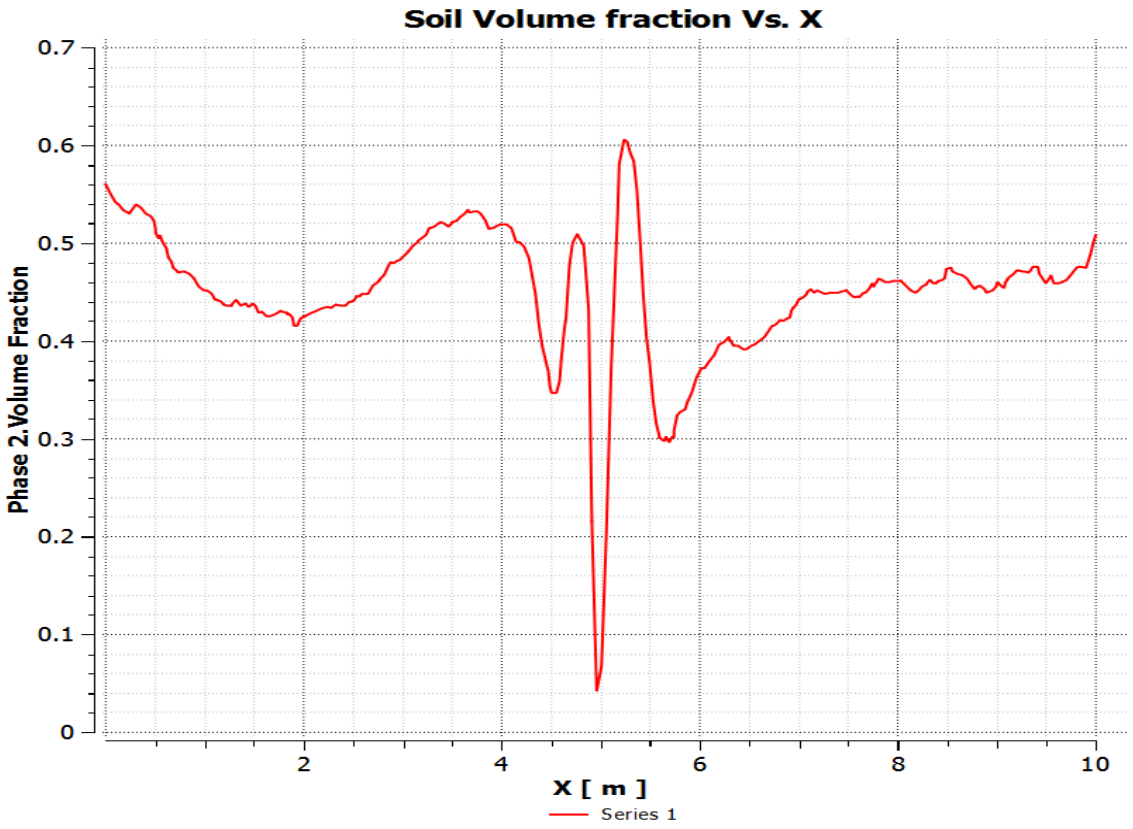

Figure 50 Soil volume fraction for a velocity inlet of 10 m/s at 5 s

8 FLOW REGIME BOUNDARIES

After validating the model, the model is used to attempt to identify the boundaries between the gas low regimes, diffusion, fluidization, and crater formation. In order to do so, various simulations are run using different parameters. In order to have a useful representation of the data, it is converted using dimensionless numbers, which would allow other cases different than the model setup to be comparable. The two main factors that should be taken into account are the fluid information and the soil information. The fluid information, which is varies in this chapter by changing the fluid velocity is represented using the Reynolds number. The soil information varies using different soil densities and is represented using the Archimedes number. This representation is used to identify fluidization regimes as indicated by Yan[35]. Thus, the same approach is used to identify the underground gas flow regime by plotting $\frac{Re}{Ar^{1/3}}$ vs. $Ar^{1/3}$. In addition, the conditions given in Qatar can be compared to the already existing experimental work, to predict the possible flow regime.

8.1 Qatar Flow Compared to Experimental Work

The volumetric flow rate of the gas flow in Qatar is estimated based on the data given in Table 5, then the results are compared to the volumetric flow rates obtained in the literature from experimental data. The following equations are used in order to estimate the volumetric flow rate:[62]

First, checking if the flow is choked or not by using:

$$\frac{P_{choked}}{P_0} = \left(\frac{2}{\gamma + 1}\right)^{\frac{\gamma}{\gamma - 1}} \qquad (84)$$

where γ is the specific heat ratio of the gas.

Since that the pressure value is large (80 bar), the flow is choked, and hence, the following equation is used to obtain the mass flow rate:

$$Q_m = C_0 A P_0 \sqrt{\frac{\gamma M}{R T_0} \left(\frac{2}{\gamma + 1}\right)^{\frac{\gamma}{\gamma - 1}}} \quad (85)$$

Where C_0 is the discharge coefficient assumed to be 0.61.

The volumetric flow rate can be obtained by obtained by dividing the mass flow rate with density:

$$Q_v = \frac{Q_m}{\rho} \quad (86)$$

The following table shows the final results using Qatar conditions, combined with the experimental data:

Table 9 Volumetric flow rate data and their accompanied flow regime

Source	Volumetric flow rate m^3/s	Gas flow regime
Wakoh and Hirano[6]	$1x10^{-4} – 3x10^{-4}$	Diffusion
Okamoto and Gomi[22]	$5x10^{-6} – 1.67x10^{-5}$	Diffusion
Yan et al.[25]	$5x10^{-5} – 4x10^{-4}$	Diffusion
Acton et al.[39]	0.14 – 1.49	Crater Formation
Qatar industry	0.086 – 2.45	-

From Table 9 it can be seen that the volumetric flow rate obtained for the given Qatar conditions is around 4 orders of magnitude higher than diffusion. The range is closer to

volumetric flow rate that causes crater formation. Hence, it is expected the conditions that were given in Table 5 would results in a crater formation.

8.2 Simulation Results for Boundary Identification

One of the main objectives of the project is to find the boundaries of the underground gas flow regimes, with associated flow and soil conditions. Twenty six simulations were run with varying value of velocity from 0.1 m/s to 50 m/s, and with varying the soil density values from 1000 kg/m^3 to 1600 kg/m^3. The flow regime was identified for each case, and then the case point is plotted using the dimensionless numbers mention earlier, Reynolds number and Archimedes number. On the same graph, the experimental data of Yan et al.[25] and Acton et al.[39] were also plotted. Note that the experimental data for Acton et al.[39] is shown as a single point since all of them have the same velocity from calculation, which is the sonic velocity due to the flow being choked. The value for particle diameter was assumed to be 1 mm for all cases, and the soil initial volume fraction was assumed to be 0.63 (the value used when assuming spherical particles). Table 10 shows the details of all the simulated cases, and Figure 55 shows the obtained graph. The Reynolds number and the Archimedes number can be expressed as follows:

$$Re = \frac{d_p v \rho_{fluid}}{\mu} \quad (87)$$

$$Ar = \frac{d_p^3 \rho_{fluid} (\rho_{soild} - \rho_{fluid}) g}{\mu^2} \quad (88)$$

In order to identify the kind of underground gas flow regime, the CFD-Post software was used. A user location is inserted at 0.2 m below the surface, in order to avoid any instability on the surface. Then, the soil volume fraction data is collected over the x-axis, and based on the observed result the flow regime is decided, which is observed at around 5 seconds after initial release. If the drop and fluctuation of the soil volume fraction is small on top of the release point (x=5 m), then the case is considered diffusion, as shown in Figure 51. Here, the drop in the small volume fraction is simply due to the methane passing through, and since it is small were believe it has a minimal effect on the soil. On the other hand,

when the soil volume fraction is clearly different than the initial 0.63, but not close to zero, the case is considered fluidization. Figure 52 shows an example of a case deemed as fluidization. Finally, if the soil volume fraction above the release point reaches close to zero, the case is considered crater formation, which is represented by Figure 53. A vertical line was also drawn on top of the release point to ensure the presence of a crater, and is shown in Figure 54, where clearly the soil volume fraction around the release point (y=1.1 m) are close to zero, while the soil volume in the atmosphere (y>2 m) is higher, due to the presence of the soil cloud.

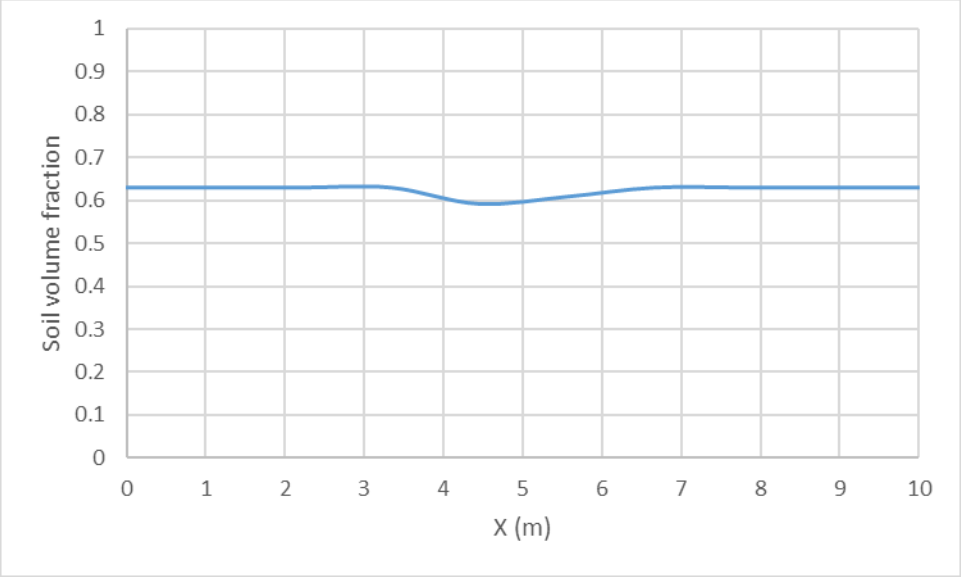

Figure 51 Soil volume fraction data for Case 1

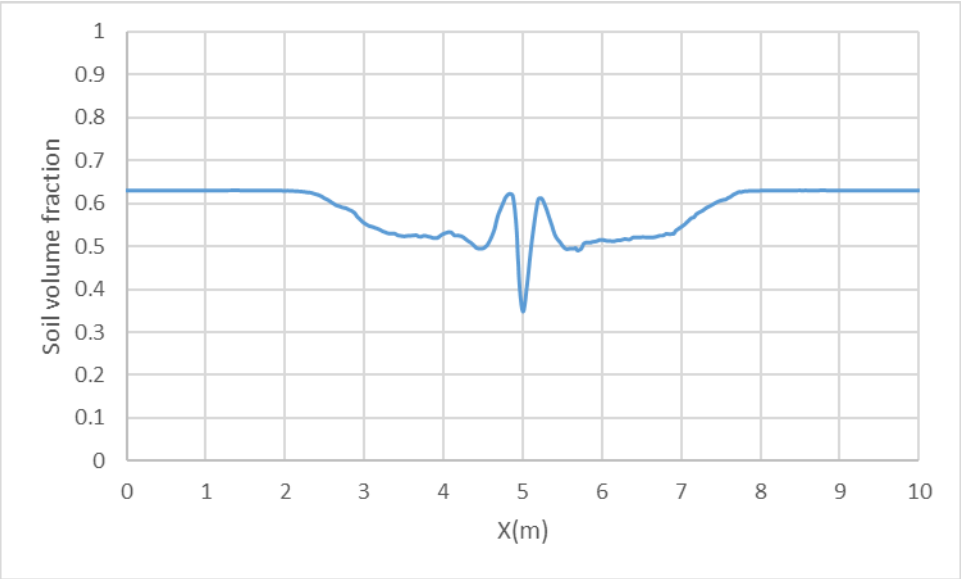

Figure 52 Soil volume fraction data for Case 2

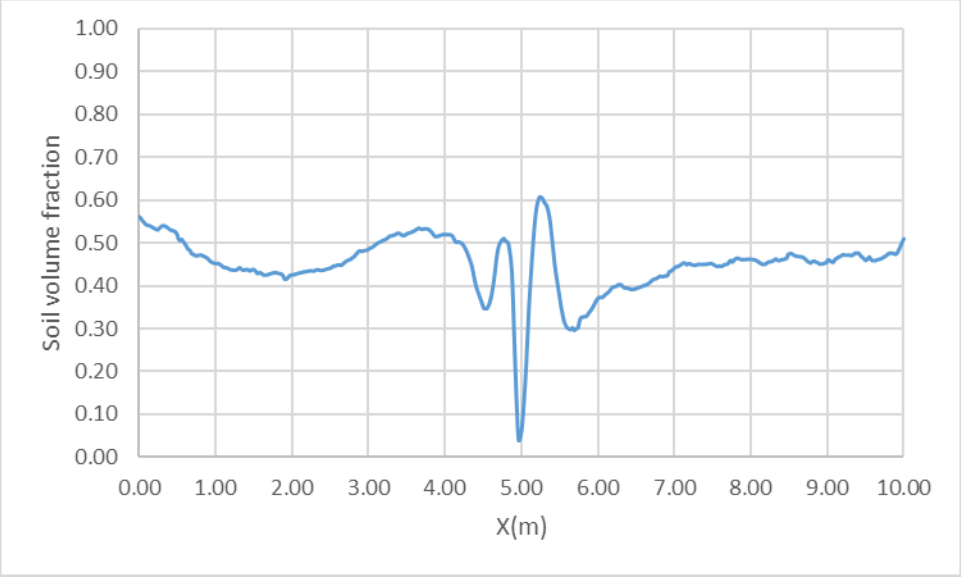

Figure 53 Soil volume fraction data for Case 4 in the horizontal axis

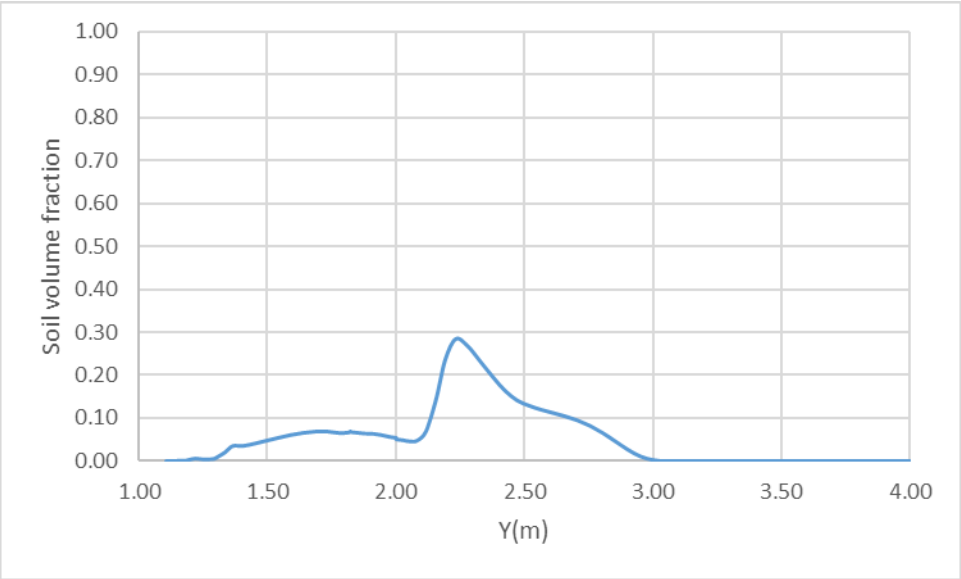

Figure 54 Soil volume fraction data for Case 4 in the vertical axis

Table 10 Simulation cases with their respective flow regime

Case #	**Soil density (kg/m^3)**	**Inlet velocity (m/s)**	**Flow regime**
Case 1	1600	0.1	Diffusion
Case 2	1600	1	Fluidization
Case 3	1600	5	Fluidization
Case 4	1600	10	Crater
Case 5	1600	25	Crater
Case 6	1600	50	Crater

Table 10 Continued

Case #	Soil density (kg/m^3)	Inlet velocity (m/s)	Flow regime
Case 7	1000	0.1	Diffusion
Case 8	1000	1	Fluidization
Case 9	1000	5	Fluidization
Case 10	1000	10	Crater
Case 11	1200	0.1	Diffusion
Case 12	1200	1	Fluidization
Case 13	1200	5	Fluidization
Case 14	1200	10	Crater
Case 15	1400	0.1	Diffusion
Case 16	1400	1	Fluidization
Case 17	1400	5	Fluidization
Case 18	1400	10	Crater
Case 19	1000	0.5	Diffusion
Case 20	1200	0.5	Diffusion
Case 21	1400	0.5	Diffusion
Case 22	1600	0.5	Diffusion
Case 23	1000	3	Fluidization
Case 24	1200	3	Fluidization

Table 10 Continued

Case #	Soil density (kg/m^3)	Inlet velocity (m/s)	Flow regime
Case 25	1400	3	Fluidization
Case 26	1600	3	Fluidization

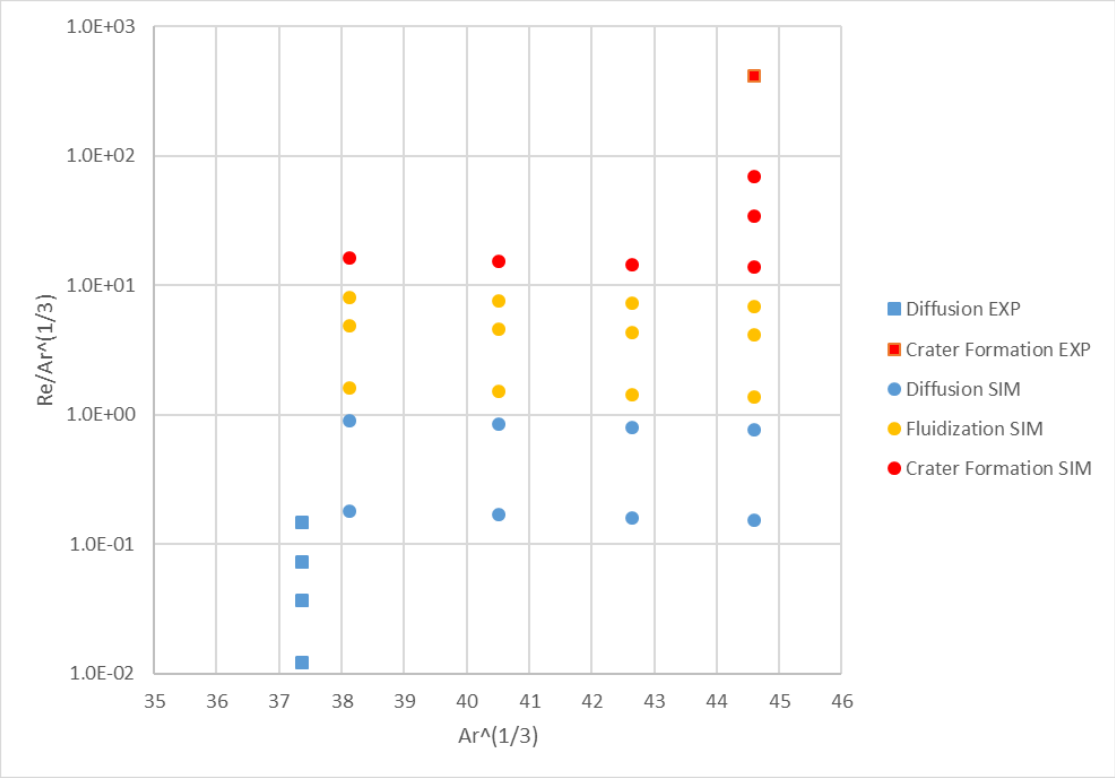

Figure 55 Results from simulations with their respective flow regime

From Figure 55 it is clear that the flow regime is affected by the methane inlet velocity. Starting from diffusion at lower velocity values, followed by fluidization at higher velocity

values, then eventually into crater formation at even higher velocity values, represented by a higher Reynolds number. On the other hand, changing the soil density values, did give different results in general, but it did not change the flow regime for the cases that were simulated, for the same velocity. According to the model results with the current setup, the change from the diffusion to the fluidization behavior occurs at an inlet gas velocity value between 0.5 m/s and 1 m/s. The change from the fluidization behavior to the crater formation behavior seems to take place between an inlet gas velocity value of 5 m/s and 10 m/s. One of the drawbacks of this boundary identification approach is the fact that the decision of the flow regime is done in a qualitative manner, which does not allow having a clear line boundary between the regimes. However, the transition between each regime is most probably not a fine line with having an unstable regime, such as a flow where the soil might fluidize next to the hole, but it would diffuse through the upper parts towards the atmosphere. Adding many more simulations, which results in adding more points to Figure 55, would make the boundaries between the different underground gas flow regimes clearer, by having more velocity values, more soil density values, and possibly varying soil particle diameter.

9 CONSQUENCE MODELLING USING FLUENT RESULTS

A leak of methane can have severe consequences as observed by the previously mentioned incidents, since that the gas is flammable. Finding out the potential consequences of an underground gas leak is necessary in order to design prevention or mitigation barriers that are effective. The results out of a simulation can be used as an input for consequence modelling. For example, for a gas release of 10 m/s, the mass flow rate through the surface can be obtained, and then used as an input for dispersion models. In order to do so, CFD-Post software is used. The mass flow option is not directly available, and has to be setup by the user. The "massFlowAve" function is selected, which takes the mass flow average at a specific location. The variable selected is the methane volume fraction so that only the methane flow rate is obtained, and the location selected is the soil surface (the interface). The code the is written is "massFlowAve(Phase 1.Volume Fraction)@interface contact_region trg". The value obtained is 0.53 kg/s at 5 s, which is a little less than the inlet flow rate. The lower value is expected since the system did not yet reach steady state.

The value is then used in the Areal Locations of Hazardous Atmospheres (ALOHA) software, which is used for consequence modelling.[52] First, the chemical needs to be identified in ALOHA by going to setup, then selecting methane from the pure chemicals list. The next step is setting up the atmospheric data. The wind is assumed to be blowing with a speed of 5 m/s from the east, measured at 2 m elevation. The ground roughness is selected to be open country, and the sky is assumed to be clear with no clouds. The air temperature is assumed to be 40 ^{o}C and the humidity is assumed to be at 50%. Next the source data need to be inputted. The option chosen is direct, since that the mass flow has been integrated. The mass flow rate is inputted, and the maximum leak duration is applied which is 60 minutes. Figure 56 shows the results obtained for a flash fire using the Gaussian dispersion model.

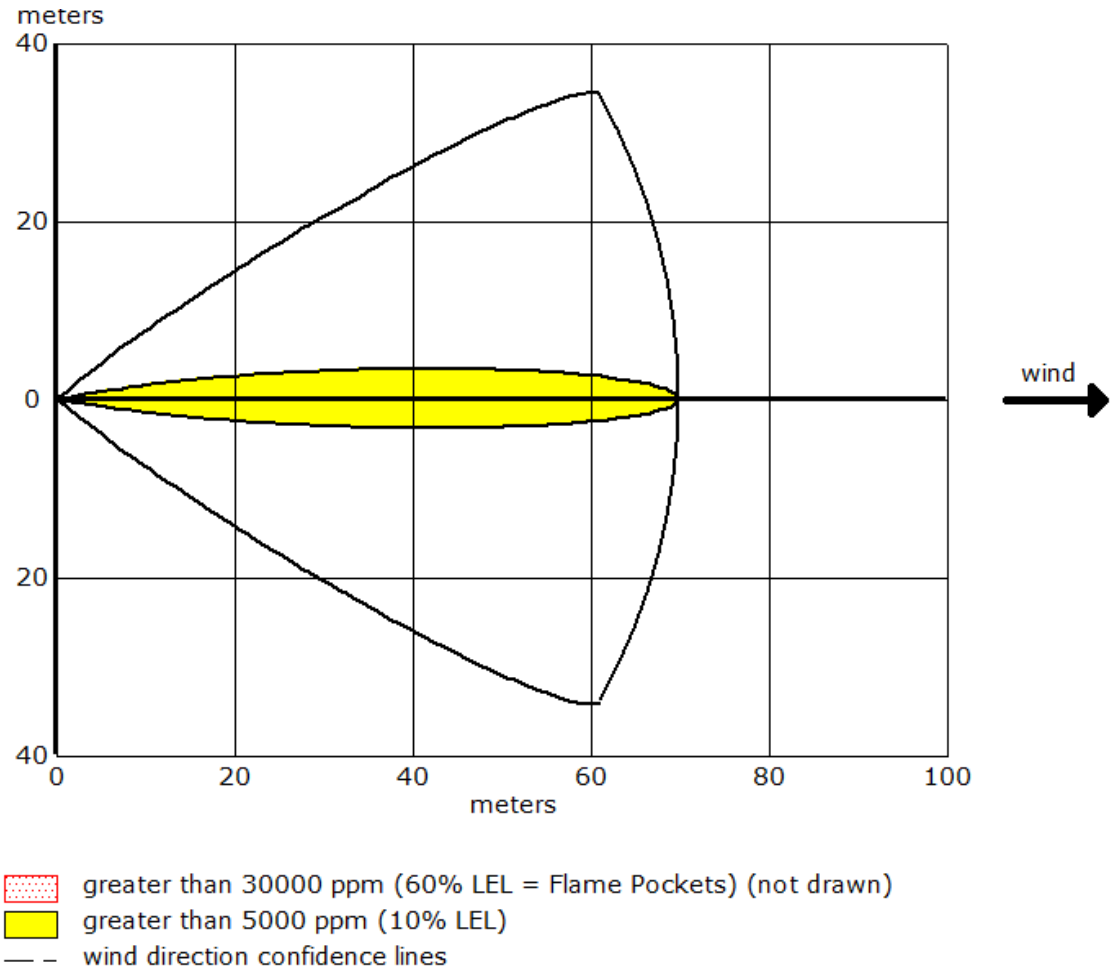

Figure 56 Flash fire threat zone from ALOHA

Figure 56 shows that the yellow threat zone with 10% of methane's lower explosive limit (LEL) reaches up to around 70 m away from the release point. While, the red threat zone with 60% or above of methane's LEL, reaches up to 28 m away from the release point. The yellow threat zone has no actual consequence and is set as default by ALOHA. The red threat zone is the zone where flash fire might occur, and it has to be taken care of while evaluating the risk. The red zone is not plotted by ALOHA due to the effect of near-field patchiness on dispersion reliability for short distances. The same procedure can be done

for various simulations to obtain their associated potential consequences. The approach used using ALOHA is however an incorrect representation of what happens on the surface, since that the major difference is that the flow is spread into a wider area, leading to a smaller velocity of release compared to the used direct point release. ALOHA doesn't have the capability of simulating a case where an area of release is given with a specific mass flux. The ALOHA approach was just shown for the sake of an example, and for actual consequence modeling, software able to model an area of release such as Phast should be used.

10 CONCLUSIONS AND RECOMMENDATIONS

Identifying the risk associated with underground natural gas releases has been of interest to the Qatar industry. Due to the flammability of natural gas, the risks associated with it can be severe and the loss of life and property is evident from previous incidents. The underground gas flow regime is not constant and it depends on the gas flow rate, ranging from diffusion for low flow rates where the soil does not move, to fluidization when the soil starts moving at higher flow rates, eventually to free jet when a crater is formed at even higher flow rates that completely displace the soil. A literature review study has been done to identify all the available integral and empirical models that are used to model each of the flow regimes. There appears to be a lack of a universal model that is able to model all kinds of underground gas flow regimes starting from diffusion all the way to crater formation. In addition, the crater formation models found were all empirical models. Thus. a CFD model was developed with the aim for it to be able to model all the kinds of flow regimes. The model was setup using ANSYS Workbench 18.1 and the steps included, designing the geometry, creating the grid, and finally using ANSYS Fluent to setup the relevant applicable models to underground gas releases. Several geometry dimensions were chosen based on the conditions provided by the Qatari industry.

Various parameters were tested using the model in order to see their effect, and optimize the model's performance. From the configuration, it was noted that the model performs in a more stable manner using velocity as an inlet boundary condition, as opposed to pressure where many simulations diverged. Another finding was the choice of the primary phase, in which it seems that choosing the dominant phase in the inlet boundary condition as the primary phase gives better results. One of the key findings was that the methane cloud did not expand as much vertically as it did horizontally, which was resulted from the sand cloud the formed in the atmosphere, and blocked the gases way vertically. This might result in overlooking risks associated to the possibility of methane igniting near the surface due to the assumption that it is not between its upper and lower flammability limits. However, it is evident from the results that some of the methane near the surface is in the flammability range and the possibility of ignition is present.

The model was validated against experimental data for a diffusion flow regime. The results were compared at different points across the geometry. The data on mirror locations were identical since that the model is symmetrical. There was a difference between the model and the experimental data, especially presented by a lag in the concentration in the experimental data that the model was not able to predict. However, the NMSE values, and having the concentration values in the same order of magnitude with the experimental data, and the model following a similar trend to the experimental data, it was concluded that the model is able to predict the underground gas flow regime and the methane concentration in a reasonable manner. However, due to the large residuals associated with the numerical results, more investigation should be done on this matter.

The information given by the Qatar industry was converted into a gas volumetric flow rate. The data was then compared to the gas flow rate data provided by previous experimental work. It was found out that the Qatar gas flow rate lies closer to crater formation, and is around four orders of magnitude higher than the diffusion cases. Twenty six cases were simulated with different inlet gas velocity, and different soil density, and the flow regime associated with each of them. The data was then plotted in the same plot in order to identify the boundaries of each regime. From the plot (Figure 55), it was clear that the effect of velocity is significant in changing the underground gas flow regime, while changing the soil density didn't seem to affect the flow regime for the investigated simulations.

Finally, one of the simulations was taken as an example to apply consequence analysis. The CFD-Post software was used to obtain the mass flow rate of methane from the simulation, and then the mass flow rate was used as an input into the consequence modeling software ALOHA. The results that were obtained from ALOHA based on the written assumptions were reported, and the threat zone of a flash fire associated with the methane release rate was plotted, showcasing the potential consequences associated with the release. However, using ALOHA is not representative of the real case scenario, and other more advanced software should be used such as Phast.

The following points are recommended as future work for this project:

- Designing an experiment to observe the gas flow through soil. It is suggested to have a small box as a starting stage, filled with soil with known properties, and with a pipeline that passes through the box from the bottom at a known depth. The pipeline would be connected to a methane gas cylinder, and by using a pressure regulator, the methane flow rate can be varied with a known orifice size. Some methane sensors should be planted into the soil to measure the concentration of methane. It is recommended that the box is made from a clear material, such as plastic or glass, in order to observe the gas flow regime during the experiment. The experiment should be done at a safe location taking into considerations the risks associated with methane. Starting with a non-flammable gas for the experiments would be ideal. There might be a potential issue associated with the visual observation of the soil movement depending on the size of the container in the experiment. It is recommended to either perform the experiment using small containers in the beginning and then increasing the size of the container to 1 m^3 for example, and then compare the results between the two experiments and study the scalability of this experiment. The other option is to have motion sensors also installed in the soil to monitor whether the soil is moving or not during the experiment. The available models can then be compared to the obtained experimental data, including the model developed in this project;
- Studying the effect of wind in the atmospheric body on the formed methane and soil cloud, and how it would affect the simulation results. This can be done by choosing one of the sides in the atmospheric body and switching it from an outlet to an inlet, with the air velocity of interest;
- Having a mixed stream instead of pure methane as an inlet to the simulations, and including other possible consequences such as the toxicity associated with hydrogen sulfide, present in natural gas streams;

- Having more simulations with varying soil particle size, including different distributions, and recording the effect of it on the concentrations data and on the flow regime if any;
- Running more simulations with different velocity values and soil density values, to obtain a clearer boundary line between different underground gas flow regimes;
- Comparing the collected integral and empirical models from the literature review with each other, and with the developed model;
- Attempting to run simulations using CFD-DEM approach, starting possibly with a small geometry and a limited number of particles, then scaling the geometry up to real case scenarios and allowing the simulations to run for as long as possible. Then, the results should be compared for both the small geometry and the larger geometry with the Two-Phase model;
- Including bodies that would obstruct the flow, and recorder their effect on the results, since it is more realistic considering soil might contain large rocks that are not easily movable.

REFERENCES

[1] Agency for Natural Resources and Energy, “Energy statistics,” 2017.

[2] K. B. Mishra and K. D. Wehrstedt, “Underground gas pipeline explosion and fire: CFD based assessment of foreseeability,” *J. Nat. Gas Sci. Eng.*, vol. 24, pp. 526–542, 2015.

[3] A. Ranjan, “22 wouldn’t have died in pipeline blast had GAIL installed safety features_ Probe report _ The Indian Express,” *The Indian Express*, 2014. [Online]. Available: http://indianexpress.com/article/india/india-others/22-would-not-have-died-in-pipeline-blast-had-gail-installed-safety-features-as-it-had-promised-probe-report/. [Accessed: 05-Oct-2017].

[4] P. A. Report, “Natural Gas Pipeline Rupture and Fire Near Carlsberg, New Mexico, August 19, 2000,” *Nat. Transp. Saf. Board*, 2003.

[5] M. Parvini and E. Gharagouzlou, “Gas leakage consequence modeling for buried gas pipelines,” *J. Loss Prev. Process Ind.*, vol. 37, pp. 110–118, 2015.

[6] H. Wakoh and T. Hirano, “Diffusion of leaked flammable,” vol. 4, pp. 260–264, 1991.

[7] H. J. Ohstsuga, “No Title,” *Japan Gas Assoc.*, no. 91, p. 32, 1971.

[8] M. Palcoz, J. Kriegler, and E. Farkas, “No Title,” *Energietechnik*, no. 305, p. 32, 1985.

[9] S. J. Farlow, *Partial Differential Equations for Scientists and Engineers*. 1982.

[10] J. Crank, *the Mathematics of Diffusion*. 1975.

[11] Y. Hibi, K. Fujinawa, S. Nishizaki, K. Okamura, and M. Tasaki, “MULTI-COMPONENT MIGRATION IN THE GAS PHASE OF SOIL : COMPARISON BETWEEN RESULTS OF EXPERIMENTS AND SIMULATION BY DUSTY GAS MODEL,” *Japanese Geotech. Soc.*, vol. 49, no. 4, pp. 569–581, 2009.

[12] E. A. Mason, A. P. Malinauskas, and R. B. Evans, “Flow and diffusion of gases in porous media,” *J. Chem. Phys.*, vol. 46, no. 8, pp. 3199–3216, 1967.

[13] B. E. Sleep and J. F. Sykes, “Modeling the transport of volatile organics in variably saturated media,” *Water Resour. Res.*, vol. 25, pp. 81–92, 1989.

[14] B. E. Poling, J. M. Prausnitz, and J. P. O’Connel, *The Properties of Gases and Liquids*, 5th editio. New York: McGraw Hill, 2001.

[15] C. F. Curtiss and J. O. Hirschfelder, “Transport properties of multicomponent gas mixtures,” *J. Chem. Phys.*, vol. 17, no. 6, pp. 550–555, 1949.

[16] S. Hoeg, H. F. Schöler, and J. Warnatz, “Assessment of interfacial mass transfer in water-unsaturated soils during vapor extraction,” *J. Contam. Hydrol.*, vol. 74, no. 1–4, pp. 163–195, 2004.

[17] A. L. Baehr and C. J. Bruell, “Application of the Stefan-Maxwell Equations to determine limitations of Fick’s law when modeling organic vapor transport in sand columns,” *Water Resour. Res.*, vol. 26, no. 6, pp. 1155–1163, 1990.

[18] J. G. Society, “Formulation of a Dusty Gas Model for Multi - Component,” *Soils Found.*, vol. 48, no. 3, pp. 419–432, 2009.

[19] C. Thorstenson and W. Pollock, “Gas Transport in Unsaturated Zones: Multicomponent Systems and the Adequacy of Fick’s Laws,” *Water*, vol. 25, no. 3, pp. 477–507, 1989.

[20] J. Massmann and D. F. Farrier, “Effects of atmospheric pressures on gas-transport in the vadose zone,” *Water Resour. Res.*, vol. 28, no. 3, pp. 777–791, 1992.

[21] R. C. Reid, J. M. Prausnitz, and B. E. Poling, *The Properties of Gases and Liquids*, 4th editio. New York: McGraw-Hill, 1987.

[22] H. Okamoto and Y. Gomi, “Journal of Loss Prevention in the Process Industries Empirical research on diffusion behavior of leaked gas in the ground,” *J. Loss Prev. Process Ind.*, vol. 24, no. 5, pp. 531–540, 2011.

[23] D. E. Wilson, R. E. Montgomery, and M. R. Sheller, “A mathematical model for removing volatile subsurface hydrocarbons by miscible displacement,” *Water. Air. Soil Pollut.*, vol. 33, pp. 231–255, 1987.

[24] H. Okamoto, Y. Gomi, and H. Akagi, “Movement Characteristics of Hydrogen Gas Within the Ground and Its Detection at Ground Surface,” *J. Civ. Eng. Sci.*, vol. 3, no. 1, pp. 49–66, 2014.

[25] Y. Yan, X. Dong, and J. Li, “Experimental study of methane diffusion in soil for an underground gas pipe leak,” *J. Nat. Gas Sci. Eng.*, vol. 27, pp. 82–89, 2015.

[26] D. Kunii and O. Levenspiel, *Fluidization Engineering*, vol. 1, no. c. 1991.

[27] M. O. A. Alsaydalani and C. R. I. Clayton, “Internal Fluidization in Granular Soils,” *J. Geotech. Geoenvironmental Eng.*, vol. 140, no. 3, p. 04013024, 2014.

[28] L. Massimilla and G. Volpicelli, “Flow of fluid-particle suspensions from liquid-fluidized beds,” *Ind. Eng. Chem. Fundam.*, vol. 2, no. 3, pp. 194–199, 1963.

[29] R. K. Niven, “Physical insight into the Ergun and Wen and Yu equations for fluid flow in packed and fluidised beds,” *Chem. Eng. Sci.*, vol. 57, no. 3, pp. 527–534, 2002.

[30] Y. F. Shi, Y. S. Yu, and L. T. Fan, “Incipient Fluidization Condition for a Tapered Fluidized Bed,” *Ind. Eng. Chem. Fundam.*, vol. 23, no. 4, pp. 484–489, 1984.

[31] Y. Peng and L. T. Fan, “Hydrodynamic characteristics of fluidization in liquid-solid tapered beds,” *Chem. Eng. Sci.*, vol. 52, no. 14, pp. 2277–2290, 1997.

[32] S. Ergun, “Fluid flow through packed columns,” *Chemical Engineering Science*, vol. 48, no. 2. pp. 89–94, 1952.

[33] J. E. van Zyl, M. O. A. Alsaydalani, C. R. I. Clayton, T. Bird, and A. Dennis, “Soil fluidisation outside leaks in water distribution pipes – preliminary observations,” *Proc. Inst. Civ. Eng. - Water Manag.*, vol. 166, no. 10, pp. 546–555, 2013.

[34] R. K. Niven and N. Khalili, *In situ fluidisation by a single internal vertical jet*, vol. 36, no. 2. 1998.

[35] W.-C. Yan, *Handbook of Fluidization and Fluid-Particle Systems*. New York, 2003.

[36] C. G. Philippsen, A. C. F. Vilela, and L. D. Zen, "Fluidized bed modeling applied to the analysis of processes: Review and state of the art," *J. Mater. Res. Technol.*, vol. 4, no. 2, pp. 208–216, 2015.

[37] E. P. Silva, M. Nele, P. F. Frutuoso e Melo, and L. Könözsy, "Underground parallel pipelines domino effect: An analysis based on pipeline crater models and historical accidents," *J. Loss Prev. Process Ind.*, vol. 43, pp. 315–331, 2016.

[38] N. D. G. B. N. Leis, S. M. Pimputkar, "Line Rupture and the Spacing of Parallel Lines," p. 41, 2002.

[39] M. R. Acton and N. W. Jackson, "DEVELOPMENT OF GUIDELINES FOR PARALLEL PIPELINES," pp. 1–11, 2010.

[40] H. Versteeg and W. Malalasekra, *An Introduction to Computational Fluid Dynamics: The finite-volume method*. 2007.

[41] L. Zhou, L. Zhang, W. Shi, R. Agarwal, and W. Li, "Transient Computational Fluid Dynamics/Discrete Element Method Simulation of Gas–Solid Flow in a Spouted Bed and Its Validation by High-Speed Imaging Experiment," *J. Energy Resour. Technol.*, vol. 140, no. 1, p. 012206, 2017.

[42] F. Alobaid and B. Epple, "Improvement, validation and application of CFD/DEM model to dense gas-solid flow in a fluidized bed," *Particuology*, vol. 11, no. 5, pp. 514–526, 2013.

[43] A. Bakshi, C. Altantzis, R. B. Bates, and A. F. Ghoniem, "Eulerian-Eulerian simulation of dense solid-gas cylindrical fluidized beds: Impact of wall boundary condition and drag model on fluidization," *Powder Technol.*, vol. 277, pp. 47–62,

2015.

[44] R. B. Bird, W. E. Stewart, and E. N. Lightfoot, *Transport Phenomena*, 2nd ed. John Wiley & Sons, Inc., 2007.

[45] C. D. Argyropoulos and N. C. Markatos, "Recent advances on the numerical modelling of turbulent flows," *Appl. Math. Model.*, vol. 39, no. 2, pp. 693–732, 2015.

[46] B. E. Launder and B. I. Sharma, "Application of the energy-dissipation model of turbulence to the calculation of flow near a spinning disc," *Lett. Heat Mass Transf.*, vol. 1, no. 2, pp. 131–137, 1974.

[47] T.-H. Shih, W. W. Liou, A. Shabbir, Z. Yang, and J. Zhu, "A NEW kt EDDY VISCOSITY MODEL FOR HIGH :REYNOLDS NUMBER TURBULENT FLOWS," *Compurers Fluids*, vol. 24, no. 3, pp. 227–238, 1995.

[48] V. Yakhot, S. A. Orszag, S. Thangam, T. B. Gatski, and C. G. Speziale, "Development of turbulence models for shear flows by a double expansion technique," *Phys. Fluids A*, vol. 4, no. 7, pp. 1510–1520, 1992.

[49] D. Wilcox, *Turbulence Modelling for CFD*, Third. DCW Industries, Inc., 2006.

[50] Y. Wu, D. Liu, J. Ma, and X. Chen, "Effects of gas-solid drag model on Eulerian-Eulerian CFD simulation of coal combustion in a circulating fluidized bed," *Powder Technol.*, vol. 324, pp. 48–61, 2018.

[51] D. Liu, C. Bu, and X. Chen, "Development and test of CFD-DEM model for complex geometry: A coupling algorithm for Fluent and DEM," *Comput. Chem. Eng.*, vol. 58, pp. 260–268, 2013.

[52] "ALOHA Software." [Online]. Available: https://www.epa.gov/cameo/aloha-software. [Accessed: 17-Jul-2018].

[53] D. Gidaspow, R. Bezburuah, and J. Ding, "Hydrodynamics of circulating fluidized beds: Kinetic theory approach," *7th Fluid. Conf.*, pp. 75–82, 1992.

[54] M. Syamlal, W. Rogers, and T. J. O`Brien, “MFIX documentation theory guide,” vol. 1004, no. December, 1993.

[55] J. Lundberg and B. M. Halvorsen, “A review of some exsisting drag models describing the interaction between phases in a bubbling fluidized bed,” *Proc. 49th Scand. Conf. Simul. Model. Oslo Univ. Coll. Oslo, Norw.*, pp. 7–8, 2008.

[56] C. K. K. Lun, S. B. Savage, D. J. Jeffrey, and N. Chepurniy, “Kinetic theories for granular flow: inelastic particle in couette flow and slightly inelastic particle in a general flow field,” *J. Fluid Mech.*, vol. 140, pp. 223–256, 1984.

[57] T. Engineering Toolbox, “Densities of Common Materials.” [Online]. Available: https://www.engineeringtoolbox.com/density-materials-d_1652.html. [Accessed: 25-Jun-2018].

[58] LEAP CFD Team, “Tips & Tricks: Convergence and Mesh Independence Study,” 2012. [Online]. Available: https://www.computationalfluiddynamics.com.au/convergence-and-mesh-independent-study/. [Accessed: 25-Jul-2018].

[59] United States Department of Agriculture, “USDA Textural Soil Classification,” *Soil Mechanics Level I Module 3 - USDA Textural Soil Classification*. pp. 1–53, 1987.

[60] “Lower and Upper Explosive Limits for Flammable Gases and Vapors (LEL / UEL),” p. 22.

[61] “NMSE.” [Online]. Available: https://rem.jrc.ec.europa.eu/RemWeb/atmes2/20b.htm. [Accessed: 01-Jul-2018].

[62] D. A. Crowl and J. F. Louvar, *Chemical Process Safety: Fundamentals with Applications*, Third Edit. Prentice Hall.

APPENDIX

- **Example of journal file code used for a general simulation with constant diameter with methane as primary phase**

/file/read-case /lustre/projects/Case1.cas

/solve/initialize/initialize-flow

/solve/patch phase-2 soil () mp 0.63

/solve/patch phase-3 soil () mp 0.37

/solve/patch phase-3 atmosphere_ () mp 1

/solve/dual-time-iterate 10000 100

/file/write-data Case_1

exit

yes

- **Example of journal file code used for a general simulation with varying diameter with methane as primary phase**

/file/read-case /lustre/projects/Case1.cas

/solve/initialize/initialize-flow

/solve/patch phase-2 soil () bin-0-fraction 0.25

/solve/patch phase-2 soil () bin-1-fraction 0.25

/solve/patch phase-2 soil () bin-2-fraction 0.25

/solve/patch phase-2 soil () bin-3-fraction 0.25

/solve/patch phase-2 soil () mp 0.63

/solve/patch phase-3 soil () mp 0.37

/solve/patch phase-3 atmosphere_ () mp 1

/solve/dual-time-iterate 10000 100

/file/write-data Case_1

exit

yes

- **Example of journal file code used for validation including the species model**

/file/read-case /lustre/projects/Case_exp.cas

/solve/initialize/initialize-flow

/solve/patch phase-2 soil () mp 0.87

/solve/patch phase-2 atmosphere_ () mp 0

/solve/patch phase-1 soil () species-0 0

/solve/patch phase-1 atmosphere_ () species-0 0

/solve/dual-time-iterate 16000 100

/file/write-data Case_exp

exit

yes

- **Example of job file used for the super computer**

#!/bin/bash

#SBATCH -J Case_1

#SBATCH -p l_long

#SBATCH --gres=craynetwork:0

```
#SBATCH --qos ll

#SBATCH --time=24:00:00

#SBATCH -N 1

#SBATCH --ntasks-per-node=24

#SBATCH --output=e_ansys_sim.%j

#SBATCH --error=o_ansys_sim.%j

#SBATCH --hint=nomultithread


## Get job Stats

echo "Starting at "`date`

echo "SLURM_JOBID="$SLURM_JOBID

echo "SLURM_JOB_NODELIST"=$SLURM_JOB_NODELIST

echo "SLURM_NNODES"=$SLURM_NNODES

echo "SLURMTMPDIR="$SLURMTMPDIR

echo "working directory = "$SLURM_SUBMIT_DIR



# Load Ansys Module

module use /lustre/sw/xc40ac/modulefiles

module load ansys/182
```

```
# Load Intel Compiler if needed for simulation

# module swap PrgEnv-cray/5.2.82 PrgEnv-intel



# Start Simulation

echo "Starting Simulation.."


fluent 2ddp -gu -nm -t8 -i j_fluent_v1.jou >f_Case_1.out



echo "Ending at "`date`

echo "Simulation Ended"
```